

INVESTIGATION OF EXTENDED DEFECTS IN CADMIUM ZINC TELLURIDE
CRYSTALS GROWN BY VERTICAL GRADIENT FREEZE (VGF) TECHNIQUE

A THESIS SUBMITTED TO
THE GRADUATE SCHOOL OF NATURAL AND APPLIED SCIENCES
OF
MIDDLE EAST TECHNICAL UNIVERSITY

BY

ÇİĞDEM DOĞRU

IN PARTIAL FULFILLMENT OF THE REQUIREMENTS
FOR
THE DEGREE OF MASTER OF SCIENCE
IN
PHYSICS

JULY 2015

Approval of the Thesis:

**INVESTIGATION OF EXTENDED DEFECTS IN CADMIUM ZINC
TELLURIDE CRYSTALS GROWN BY VERTICAL GRADIENT FREEZE
(VGF) TECHNIQUE**

submitted by **ÇİĞDEM DOĞRU** in partial fulfillment of the requirements for the degree of **Master of Science in Physics Department, Middle East Technical University** by,

Prof. Dr. Gülbin Dural Ünver
Dean, Graduate School of **Natural and Applied Sciences** _____

Prof. Dr. Mehmet Zeyrek
Head of Department, **Physics** _____

Prof. Dr. Raşit Turan
Supervisor, **Physics Dept., METU** _____

Assoc. Prof. Dr. Y. Eren Kalay
Co-Supervisor, **Metallurgical and Materials Eng. Dept., METU** _____

Examining Committee Members:

Prof. Dr. Mehmet Parlak
Physics Dept., METU _____

Prof. Dr. Raşit Turan
Physics Dept., METU _____

Prof. Dr. Bülent Akınoğlu
Physics Dept., METU _____

Assoc. Prof. Dr. H. Emrah Ünalın
Metallurgical and Materials Engineering Dept., METU _____

Assoc. Prof. Dr. Mustafa Kulakcı
Physics Dept., Anadolu University _____

Date: 14.07.2015

I hereby declare that all information in this document has been obtained and presented in accordance with academic rules and ethical conduct. I also declare that, as required by these rules and conduct, I have fully cited and referenced all material and results that are not original to this work.

Name, Lastname: iğdem Doğru

Signature :

ABSTRACT

INVESTIGATION OF EXTENDED DEFECTS IN CADMIUM ZINC TELLURIDE CRYSTALS GROWN BY VERTICAL GRADIENT FREEZE (VGF) TECHNIQUE

Dođru, iđdem

MS, Department of Physics

Supervisor: Prof. Dr. Rařıt Turan

Co-Supervisor: Assoc. Prof. Dr. Y. Eren Kalay

July 2015, 102 Pages

Cadmium Zinc Telluride (CZT) crystal is a promising material due to its high atomic number, room temperature operability and low leakage current. It is used in many important applications such as room temperature gamma ray and X-ray detectors, medical imaging spectrometers. In addition, CdZnTe crystal has been accepted as an excellent substrate for the growth of $\text{Hg}_{1-y}\text{Cd}_y\text{Te}$ epitaxial layer, which is used for the fabrication of advanced infrared focal plane arrays (IR FPA) due to the good lattice match with $\text{Hg}_{1-y}\text{Cd}_y\text{Te}$. However, CZT crystal has a strong tendency to generate defects such as dislocations, inclusions, precipitates, twins and sub-grain boundaries. One of the most successful approaches in identifying the nature and the amount of these defects is based on etching the surface of the crystal. This thesis focuses on different etching studies conducted on $\text{Cd}_{0.96}\text{Zn}_{0.04}\text{Te}$ substrates to reveal the etch-pit formation with the purpose of determining the total defect density throughout the substrate surface. Extensive studies on different etching methods such as Nakagawa, Everson, Inoue and Bagai etchants have been carried to investigate the dislocation

density and thus the CZT crystal quality. Following to each etching process, CZT crystals have been characterized by a series of versatile characterization techniques such as Energy Dispersive X-ray (EDS) Spectroscopy, Scanning Electron Microscopy (SEM) and Transmission Electron Microscopy (TEM). The kinetics of each etchant on different substrate orientation was studied and the etch rates were determined. Etch pit formation and its dependence on surface orientation were identified through extensive experiments.

Keywords: CdZnTe, defects, dislocations, inclusions, etching

ÖZ

DIKEY GRADYAN SOĞUTMA TEKNİĞİYLE BÜYÜTÜLEN KADMIYUM ÇİNKO TELLÜR KRİSTALLERİNDE BÜYÜK BOYUTLU KUSURLARIN ANALİZİ

Doğru, Çiğdem

Yüksek Lisans, Fizik Bölümü

Tez Yöneticisi: Prof. Dr. Raşit Turan

Ortak Tez Yöneticisi: Doç. Dr. Y. Eren Kalay

Temmuz 2015, 102 sayfa

Kadmiyum Çinko Tellür (CZT) kristali oda sıcaklığında çalışabilmesi, yüksek atom numarasına ve düşük kaçak akımına sahip olmasından dolayı gelecek vaat eden önemli bir malzemedir. CZT kristali oda sıcaklığında çalışan gama ışını ve X-ışını algılayıcısı, tıbbi görüntüleme spektrometresi gibi birçok önemli uygulamada kullanılmaktadır. Ayrıca, CdZnTe kristali HgCdTe kristali ile en iyi örgü uyumluluğu özelliğine sahip olmasından dolayı, gelişmiş Kızılötesi Odak Düzlemi Dizinlerinin üretimi için gerekli olan $Hg_{1-y}Cd_yTe$ epitaksiyel katman büyütmesinde taban (alt taş) olarak kabul edilmiştir. Cıva Kadmiyum Tellür (MCT) kızılötesi fotodedektörlerin performansının düşmesindeki en büyük etkenlerden biri kusurlu yapıya sahip CZT tabanlardır. Bundan dolayı, CZT içerisinde bulunan dislokasyonların oluşumunu ve özelliklerini anlamak oldukça önemlidir. CZT kristali dislokasyon, birikimler (inclusions), çökelti (precipitations), ikizler ve alt tanecik sınırları gibi kusurlar oluşturmaya oldukça yatkın bir malzemedir. Bu tez çalışması, $Cd_{0.96}Zn_{0.04}Te$ tabanı üzerine farklı kusur aşındırma işlemleri uygulanarak, taban yüzeyi boyunca oluşan kusurlar incelenip tabanın aşındırma çukur yoğunluğunu (EPD) hesaplamaktır. Nakagawa, Everson, Inoue ve

Bagai gibi aşındırma yöntemleri kullanarak CZT tabanının kristal kalitesi incelenmektedir. Her bir aşındırma sonrası, CZT kristalleri EDS, taramalı elektron mikroskobu (SEM) analizi ve Geçirimli Elektron Mikroskopu (TEM) analizi gibi farklı karakterizasyon teknikleri gerçekleştirilecektir. Her bir aşındırıcının farklı yönelimlere sahip örnekler üzerindeki etkisi ve aşındırma hızı çalışılmıştır. Üçgen çukur oluşumu ve örneğin yönelimine olan bağlantısı çeşitli deneyler ile incelenmiştir. Üçgen çukurların farklı yönelimlerde oluşum şekilleri açığa çıkarılmıştır.

Anahtar kelimeler: CdZnTe, kusurlar, dislokasyonlar, birikimler, aşındırma

To my family

ACKNOWLEDGMENTS

This work is related to the studies on CdZnTe growth and analysis carried out at the Crystal Research Laboratory (CRL) at the premises of GÜNAM facilities.

First of all, I would like to thank my supervisor Prof. Dr. Raşit Turan for providing me the opportunity to be a member of GÜNAM family. I am very grateful to him for his informative discussions and excellent guidance during my study.

I express my gratitude to my co-supervisor Assoc. Prof. Dr. Y. Eren Kalay for his creative ideas and sharing his theoretical and experimental knowledge with me.

Prof. Dr. Mehmet Parlak is appreciated for his encouragement, inspiration and guidance during my study.

I would like to next thank to my 'Crystal Growth Group' and GÜNAM (LAB-118) members. I really appreciate Fırat Es and Ergi Dönerçark for their help during my thesis study. I thank sincerely to Yasin Ergunt for his guidance and experimental knowledge. I express my gratitude for his valuable suggestions about characterization techniques and his encouraging comments throughout my study. I really appreciate Bengisu Yaşar and Mertcan Başkan for their great work in SEM imaging. Their help has improved the prominent part of my thesis study.

Special thanks to Özden Başar Balbaşı for his endless support and infinite kindness.

I would like to thank ASELSAN Inc. for their support and funding in this study.

My dear friends Bahar Akdeniz, Yasemin Külte, Berna Öztürk, Gülüzar Köysüren, Merve Ertuğrul, and Zeynep Gündoğan always gave me a delightful time and kept me motivated. They were always there for me and cheered me up all the time.

Last but not the least I would like to thank my family for their unconditional love, endless support and encouragement during my study.

TABLE OF CONTENTS

ABSTRACT	v
ÖZ.....	vii
ACKNOWLEDGMENTS.....	x
TABLE OF CONTENTS	xi
LIST OF TABLES	xiv
LIST OF FIGURES.....	xv
CHAPTERS	
1. INTRODUCTION.....	1
1.1 Importance of CdZnTe	1
1.2 Growth Techniques and Defects in CdZnTe	2
1.3 Etch Pit Density (EPD).....	3
1.4 Thesis Overview	4
2. THEORY OF DEFECTS & ETCHING.....	7
2.1 Structure of CdZnTe	7
2.2 Crystalline Defects in CdZnTe	9
2.2.1 Dislocations.....	10
2.2.2 Stacking Faults	14
2.2.3 Twins and Twin Boundaries	15
2.2.4 Precipitates and Inclusions.....	17
2.2.5 Grain and Grain Boundaries	19
2.2.6 Cracks.....	20

2.3 Etching of CdZnTe	20
2.3.1 Etch Pit Formation	22
2.3.2 Etchants and their chemical reactions on CZT crystals	24
2.3.2.1 Inoue Etching	26
2.3.2.2 Nakagawa Etching	27
2.3.2.3 Everson Etching	27
2.3.2.4 Saucedo Etching	28
2.3.2.5 Bagai Etching	29
2.3.2.6 Bromine Methanol Etching	29
2.3.2.7 Determination of Crystallographic Polarity	30
3. EXPERIMENTAL PROCEDURES	33
3.1 Sample Information	33
3.2 Surface Process of CdZnTe Crystals	35
3.2.1 Slicing and Mechanical Polishing	35
3.2.2 Chemical Etching for Final Polish	36
3.2.3 Crystallographic Polarity Determination	36
3.3 Process of Chemical Etching	37
3.3.1 Etching	37
3.3.2 Etching Rate Study	41
3.3.3 Oxidation Study	41
3.4 Transmission Electron Microscopy Analysis	42
4. RESULT & DISCUSSION	43
4.1 Mechanical polishing	43

4.2 Bromine Methanol Chemical Etching	45
4.3 Etching Studies	46
4.3.1 Inoue Etching	46
4.3.2 Nakagawa Etching	54
4.3.3 Everson Etching	60
4.3.4 Bagai Etching	63
4.3.5 Saucedo Etching	65
4.3.6 Revealing Te inclusions by Etching Method	70
4.3.7 Etch Rate Analysis	75
4.3.7.1 Inoue EAg2 Etch Rate Analysis	76
4.3.7.2 Nakagawa Etching Rate Analysis	78
4.3.7.3 Everson Etching Rate Analysis	80
4.3.8 Surface Chemistry	81
4.4 Oxidation studies	83
4.5 TEM	86
4.6 EPD Overview	88
5. CONCLUSIONS	91
REFERENCES	95

LIST OF TABLES

TABLES

Table 1 Commonly used dislocation-revealing etchants for family of CdTe	25
Table 2 Sample naming in accordance with origin, orientation and processes.....	34
Table 3 Nakagawa etching of CZT samples with different time intervals.....	38
Table 4 Everson etching of CZT samples with different time intervals	38
Table 5 Bagai etching of CZT samples with different time intervals	39
Table 6 Inoue etching of CZT samples with different time intervals	40
Table 7 Saucedo etching of CZT samples with different time intervals	40
Table 8 Etch rate parameters; different etchants on {111} & {211} planes	41
Table 9 EPD differences and change in the morphology of the pits obtained using different etchants	89

LIST OF FIGURES

FIGURES

Figure 1 Sphalerite structure of CZT crystal.....	8
Figure 2 Polar surfaces in Sphalerite Crystal.....	9
Figure 3 Partial dislocations in Thompson's tetrahedron in FCC crystals.....	12
Figure 4 Types of dislocation found in the Sphalerite structure.	13
Figure 5 Model of Cd and Te related dislocation	14
Figure 6 Stacking sequence of twin boundary of sphalerite lattice.	17
Figure 7 The shape of etch pits on different orientations.....	23
Figure 8 Etch pits on {111}B and {211}B surfaces with two different kinds of dislocations.....	28
Figure 9 Cd and Te terminated surfaces in the sphalerite structure.....	31
Figure 12 FIB technique a) Thinning the sample b) Both side of the sample removed by using Ga ions c) The electron transparent thin membrane was pulled from the bulk specimen using the lift-out technique.	42
Figure 11 AFM images of MT1_S1 sample after mechanical lapping process.....	44
Figure 12 Final polishing procedure of MT1_S1 sample	44
Figure 13 Chemical etching with B-M solution after polishing process of MT1_S1 sample	45
Figure 14 SEM images of 1 min modified EAg-2 etched {110} MT1_R1 sample...	47
Figure 15 XRD pattern and SEM images of 2 min modified EAg-2 etched MT1_S3 sample	48
Figure 16 SEM images of 1 min Modified EAg2 etched {211} Commercial_W10 sample	48
Figure 17 SEM images of 1 min modified EAg2 etched {211} MT_W2 sample	49
Figure 18 SEM images of twin boundary revealed on MT_W2 sample.....	50
Figure 19 SEM images of as-cut {111} MT1_S8 sample.	51

Figure 20 a) Image of central slab of MT4_M1 sample. b) Numbering on the sample gives the location of where EPD and EDS measurements were taken.	52
Figure 21 SEM images of MT4_M1 sample.....	52
Figure 22 Comparison of EDS Analysis and EPD Measurements of MT4_M1 sample with respect to measurement points from bottom to heel of the sample.....	53
Figure 23 SEM images of 1 min Nakagawa etched {111} MT1_S4 sample.....	55
Figure 24 SEM images of 2 min Nakagawa etched {111} MT1_S5 sample.....	56
Figure 25 SEM images of 1 min Nakagawa etched {111} MT1_S3 sample.....	57
Figure 26 SEM images of 2 min Nakagawa etched Commercial_W4 sample	58
Figure 27 SEM images of Nakagawa etched Commercial_W6 sample by varying etching time	59
Figure 28 The average size of the etch pits exposed to varying etching time; length of the etch pits increased with time. (Lines are for visual aid).....	59
Figure 29 SEM images of Commercial_W6 after 30 min Nakagawa etching.	60
Figure 30 SEM images of 1 min Everson etched Commercial_W7 sample	61
Figure 31 SEM images of 2 min Everson etched Commercial_W8 sample.....	62
Figure 32 SEM images of Everson etched MT1_S3 sample.	63
Figure 33 SEM images of 4 min Bagai etched {211} Commercial_W11 sample.....	64
Figure 34 SEM images of 4 min Bagai etched {111} MT1_S3 sample	64
Figure 35 Schematic of formation of etch pits after exposure of etchants.....	65
Figure 36 SEM images of 30 sec. Saucedo etched {111} MT2_S4 sample	66
Figure 37 SEM images of Saucedo etched {111} MT1_S9 sample	67
Figure 38 SEM images of the comparison of Saucedo and Inoue etching	68
Figure 39 SEM images of Saucedo etched multi-grain MT1_M1 sample.....	69
Figure 40 SEM images of 2 min Saucedo etched MT1_M1 sample	70
Figure 41 SEM images of Te inclusions embedded into CZT wafers	71
Figure 42 SEM images of 6 min modified EAg2 etched MT2_S3 sample.....	72
Figure 43 a) SEM image of triangular Te inclusion on MT2_S3 sample	73

Figure 44 a) SEM image of hexagonal Te inclusions with star-shaped Cd residuals on MT2_S3 sample. b) EDS analysis shows the change in atomic concentration of Cd, Zn and Te on the points of the line.....	73
Figure 45 SEM images of 6 min modified EAg2 etched MT1_S2 sample. a) and b) Te inclusions and dislocations observed on a straight line.	74
Figure 46 a) SEM image of hexagonal Te inclusion surrounded with dislocation on {111}B oriented MT1_S2 sample b) EDS analysis shows the change in atomic concentration of Cd, Zn and Te on the points of the line.....	75
Figure 47 Inoue EAg2 etched {211} oriented MT2_W1 sample; a) Weight measurements, b) Thickness measurements.	77
Figure 48 Inoue EAg2 etched {111} oriented MT1_S2 sample; a) Weight measurements, b) Thickness measurements.	78
Figure 49 Nakagawa etched {211} oriented MT2_W2 sample a) Weight measurements, b) Thickness measurements.	79
Figure 50 Nakagawa etching of {111} oriented MT1_S4 sample; a) Weight measurements, b) Thickness measurements.	79
Figure 51 Thickness measurement of Everson etching; a) {111} oriented MT2_S1 Sample. b) {211} oriented MT2_W3 Sample.....	80
Figure 52 XPS depth profiles of CZT crystals.....	82
Figure 53 Angle Resolved XPS analysis of Nakagawa etched CZT samples	84
Figure 54 Angle-Resolved XPS showing the variation of atomic concentration vs sin (theta)	85
Figure 55 TEM image along the <110> zone axis with the corresponding SAED pattern of the CdZnTe crystal, which shows highly ordered arrangement zinc-blende lattice structure.....	86
Figure 56 TEM images of multi-grain MT_M1 sample along <110> zone axis with the corresponding SAED pattern. a) and b) Stacking faults observed in the lattice along <211> direction.....	87

CHAPTER 1

INTRODUCTION

1.1 Importance of CdZnTe

Cadmium Zinc Telluride (CZT) crystal is an important semiconducting material due to its high atomic number, which provides strong absorption and high detection, room temperature operability, excellent optoelectronic properties and low leakage current result from its wide band gap. CZT used in many important applications, such as room temperature gamma ray [1], X-ray detectors [2], medical imaging spectrometers, [3] and infrared windows [4]. In addition, due to its good lattice matching conditions, CdZnTe crystal has been established as a substrate for the growth of $\text{Hg}_{1-y}\text{Cd}_y\text{Te}$ of epitaxial layer that is necessary for the fabrication of advanced infrared focal plane arrays (IR FPA).

Initially, CdTe was used as a substrate for epitaxial growth of HgCdTe infrared detectors [5]. Later, CdTe has been developed as a gamma ray and X-ray detector since the 1960s [6]. However, the lattice of the CdTe mismatches with HgCdTe, which causes a rough surface and high defect density. Lattice constant is important in the growth of epitaxial layers and lattice-matched properties provide defect free growth. Therefore, in mid-80s research for a lattice-matched substrate resulted in the addition of ZnTe into CdTe, which makes the crystal stronger and increases the band gap [7]. In addition, the thermal expansion coefficients of HgCdTe and CdZnTe materials are nearly the same [8].

1.2 Growth Techniques and Defects in CdZnTe

Bulk crystals can be grown by several techniques such as Czochralski [9], Bridgman [10], Travelling Heating Method (THM) [11], and Vertical Gradient Freeze (VGF) [12]. Each of these techniques provides unique advantages for a particular crystal system. It is well established that CdZnTe crystal is best grown by Bridgman-like growth techniques, such as THM and VGF that provide good crystal quality. In spite of all the optimization and the use of good growth conditions, imperfections are commonly observed in the grown bulk crystals. These imperfections include point, line, surface or volume defects resulting from irregular arrangement of the atoms. A wide description of these defect structures is available in almost all solid state physics text books [13].

CdZnTe is a ternary compound, which has a cubic, zincblende structure with atomic number close to that of CdTe. It has low thermal conductivity leading to the formation of dislocation, low stacking fault energy causing twinning structure and low critical resolved shear stress causing a variety of defects in the crystal structure [14].

Owing to all this properties, CZT has a strong tendency to generate defects such as dislocations, inclusions, precipitates, twins and subgrain boundaries. In order to fabricate high performance Mercury Cadmium Telluride based infrared photo-detectors, minimization of the number of defects is crucial. Any defect existing on CdZnTe substrate will be transferred to HgCdTe film grown on it, causing failure of infrared detectors [15]. For this reason, large-area single crystal with lower defect density is needed for these applications. Therefore, it is highly important and desirable to understand the nature and the behavior of dislocations in CZT.

Reducing the dislocation density by improving the growth technology is also another crucial requirement. There are a number of methods to grow CdZnTe single crystals. CdZnTe crystals are commonly grown by high and low pressure Bridgman [16, 17], vertical Bridgman [18], Vertical Gradient Freezing (VGF) [12] and THM methods

[11]. According to Asahi, for growing large diameter crystals, Bridgman [10] and vertical gradient freezing methods [12] are the most conventional growth methods. Although Bridgman technique has been used extensively; it has some disadvantages such that the temperature distribution in furnace is changing due to the movement of the materials in the crucible, which causes large amount of stress during the crystal growth. On the other hand, the vertical gradient freezing (VGF) method has an advantage in which the materials in the crucible is at the fixed position and the temperature of the furnace is lowered gradually during the growth process so temperature distribution can be controlled in advance [12]. eV Products (USA), Redlen Technologies (Canada) and Eurorad (France) are some of the current suppliers for CdZnTe material [19].

In addition, in order to increase the quality of the crystals and decrease the defect density, some research groups try to modify their growth techniques. For example, an Italian group developed a growth technique by modifying vertical Bridgman furnace using boron oxide encapsulation, which reduces the material-crucible interaction and increases the quality of the grown-crystal. They obtained large single crystals with a low dislocation density [20]. Similarly, a French group studied vertical gradient freeze furnace and they obtained single crystal wafers of 80 mm in diameter that are free of defects [21]

1.3 Etch Pit Density (EPD)

Dislocations, twins, stacking faults, cracks, low angle grain boundaries, inclusions, and precipitates are well known extended defects in CdZnTe crystals. These defects can have negative effects on optoelectronic devices and processibility of the crystals [22]. In order to obtain high quality CdZnTe substrates, stoichiometric single crystal substrates with low density of dislocations are necessary [23, 24]. Characterization of these defects is crucial in reaching this goal. For revealing dislocations and other

defects, several etching techniques called etch pit density measurements have been developed. Substrate quality can be revealed using these measurements in combination with the X-Ray data. Etch-pit density measurement is built on estimating the number of pits appeared on the substrate surface after a selective etching process. After etching CdZnTe crystals with an acidic solution, “etch pits are formed at the exit points of dislocations on the surface” [1]. For the defect etching studies, many defect-etching solutions were established by Inoue [25], Nakagawa [26], Bagai [27], Chen [28], Everson [29], Hahnert and Schenk [5].

1.4 Thesis Overview

This thesis focuses on different etching studies conducted on $\text{Cd}_{0.96}\text{Zn}_{0.04}\text{Te}$ substrates to reveal etch pit formation with the purpose of determining the total defect density throughout the substrate surface. The work presented in this thesis is divided into five chapters.

In Chapter 1, the main concepts about CdZnTe material and its application, and the importance of CZT as a substrate material for infrared detectors are introduced.

In Chapter 2, the surface morphology of CZT, the origin of defects existing in CZT, the theory of chemical etching and TEM investigation of defects are presented.

Chapter 3 is composed of wafer processing, chemical etching processes, TEM Analysis of CdZnTe crystals. Different etching methods such as Nakagawa, Everson, Inoue, Bagai and Saucedo etching are employed to investigate CZT crystal quality. Following to each etching process, CZT crystals are to be characterized by a series of versatile characterization techniques such as Energy Dispersive X-Ray Spectroscopy (EDS), Scanning Electron Microscopy (SEM), Atomic Force Microscopy (AFM), Focused Ion Beam (FIB) and Transmission Electron Microscopy (TEM).

Chapter 4 is the results and discussion part, which focus on outcomes of the chemical etching studies. The structural properties of the defects and the effect of chemical etching solutions are presented.

In Chapter 5, a general conclusion of the work done in this thesis is provided, and recommendation for future studies of this work is presented.

CHAPTER 2

THEORY OF DEFECTS & ETCHING

The substrate needs to be uniform and highly crystalline i.e. free of defects. During the epitaxial growth process, defects in CZT will be transferred to the epitaxial layer, such as grains, twins and twin boundaries, dislocations, precipitates and inclusions and degrade the quality of the layer [22]. Additionally, etching and epitaxial growth processes depend on the orientation of the substrate.

2.1 Structure of CdZnTe

CdZnTe is a ternary compound, which has a zinc-blende crystal (Sphalerite, **Figure 1**) structure and it shows different features due to its crystallographic polarity. Sphalerite (Zinc-blende) structure contains two interpenetrating face centred cubic lattice, one of which involves metal atoms while the other one consists of non-metal atoms. Because of its characteristic properties, CdZnTe generate dislocations, twins, stacking faults, cracks, low angle grain boundaries, inclusions and precipitates. CdZnTe crystals have low critical resolved shear stress enabling the formation of dislocations.

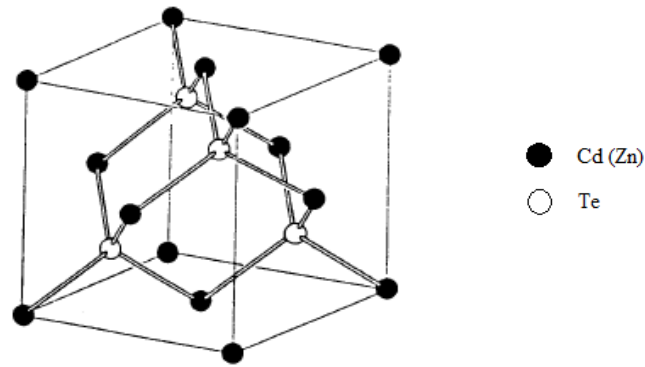


Figure 1 Sphalerite structure of CZT crystal [22].

Due to the lack of symmetry (non-centrosymmetric crystal) in the structure, CZT shows crystallographic polarity i.e. (hkl) and $(\bar{h}\bar{k}\bar{l})$ planes which have different characteristics (**Figure 2**). Lack of symmetry and high density of bonds results in double atomic layers. Each plane of a CZT crystal ended with a single atom (Cd or Te) and Cd (or Te) atom triply bonded with subjacent atoms. If Cd (or Te) added to a Te (or Cd) terminated surface, the bonding will be less stable than tetrahedral bonding. For that reason, each plane of a CZT crystal will always be terminated with a Te or Cd atom. Polar differences in sphalerite-structured crystals are most clearly observed on $\{111\}$ plane. When $\{111\}$ closed packed plane is examined, the plane terminates with a non-metal atom is called $(\bar{1}\bar{1}\bar{1})$ or B face and the plane that terminates with a metal atom is called the (111) or A face. Because of the crystal polarity, many properties differ considerably, such as etch pit geometry, quality of epitaxial growth and geometric variation of defects in the structure. However, the intensities of (hkl) and $(\bar{h}\bar{k}\bar{l})$ planes are identical when measured using X-Ray diffraction [22].

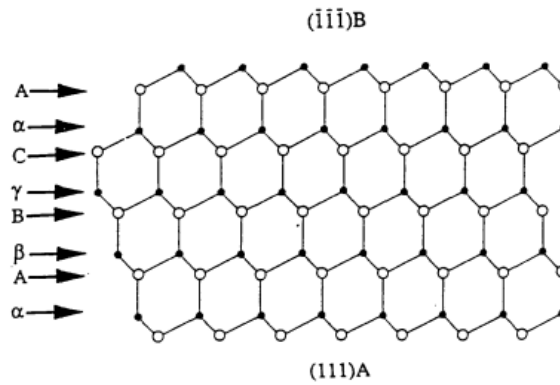


Figure 2 Polar surfaces in Sphalerite Crystal [30].

2.2 Crystalline Defects in CdZnTe

Extended defects are crystal imperfections resulting from the unstable growth conditions. Line, surface, and volume defects are extended defects that differ in the dimensional change of the defect. Dislocations can be given as an example of line defects. Line defects are one-dimensional defects and can be described as the lines, where the crystal pattern is disturbed. Twin boundaries, grain boundaries and stacking faults are surface defects defined as the interfaces between volume defects [13]. Lastly, volume defects are the variation of the lattice pattern in a finite volume. Precipitates and inclusions are considered as volume defects in crystals [31].

CZT has a tendency to generate defects due to its low thermal conductivity, its low critical resolved shear stress for slip and its low stacking fault energy. High dislocation density results from the thermal stresses during the growth processes resulting from low thermal conductivity and low critical resolved shear stress. Since CZT has a low stacking fault energy, twins, twin boundaries and stacking faults are generated in extend [22]. In addition, the retrograde solid solubility of Te causes precipitates and inclusions to incorporate in CZT matrix since the solubility of Te decreases throughout

the cooling process. In the cooling process, instable thermal gradient causes plastic deformation and leads to high dislocation density. Lastly, sphalerite structure of CZT leads to generation and propagation (slip system) of dislocations. The slip planes have the highest density of atoms i.e. most closely spaced. Therefore, the closed packed system in CZT crystal plays an important role in generating dislocation slip and twins [22].

In order to reduce the defect density, melt-solid interface in the growth process must be controlled to be either in convex or flat form. There may be an interaction between the ampoule wall and the crystal, that causes an increase in the mechanical stress and dislocations [32]. The characterization of defects are commonly carried out using an Atomic Force Microscope (AFM), Scanning Electron Microscope (SEM), Energy Dispersive X-ray Spectroscopy (EDX), X-Ray Photoelectron Spectroscopy (XPS) and Transmission Electron Microscope (TEM) to determine surface roughness, surface morphology and chemistry, the elemental composition and microstructural analysis of the surface. In addition, etch pit density (EPD) measurement is often used to identify some type of defects through specific etching procedures as discussed in the introduction.

2.2.1 Dislocations

During cooling and solidification process, dislocations are generated and move because of the thermal stress caused by the high temperature gradient in the CZT crystal growth. In addition, the interaction between ampoule wall and crystals may introduce dislocations in the matrix of the CZT crystal due the stress induced by thermal change during the growth process [32, 33]. Moreover, the plastic deformation in crystals is formed due to the movement of dislocations.

Newly formed (fresh) dislocations and grown-in (old) dislocations can be revealed by etching. Some etchants can reveal only fresh dislocations, while others reveal only old

dislocations. Generally, fresh dislocations are easily revealed due to the strain field of these dislocations [34]. Fresh dislocations can be introduced onto the crystal surface by mechanical contacts such as indenting, scratching, lapping and polishing. The stress field resulting from this mechanical contact causes dislocations to form within the crystal structure.

CdZnTe crystals have 29 different types of dislocations such as shuffle and glide dislocations, α (Cd) and β (Te) dislocations, partial and perfect dislocations, edge, screw and mixed dislocations and misfit dislocations [35]. However, the most encountered dislocation type in zincblende structured single crystals is 60° edge (α and β) dislocations originating at $\{111\} \langle 110 \rangle$ slip systems [33]. Due to the crystallographic polarity of zinc-blende structure of CZT crystals, these two type 60° edge dislocations are produced in the CZT matrix. Moreover, these dislocations are made visible on the surface of the crystals as different etch pit figures by the use of different etchants. α (Cd) and β (Te) dislocations are arranged both in the tangential and tetrahedral deformation zones with $\{111\} \langle 110 \rangle$ orientation.

According to Ball and Stick models of dislocations in sphalerite structure, α and β dislocations can be described as ‘the assignment of the extra half plane of atoms’ [22]. The α (Cd) dislocation has an extra half plane, which terminates at the slip plane forming Cd atoms. β (Te) dislocation has an extra half plane, which terminates in Te atoms.

The most possible Burgers vector for dislocations in FCC structure is $a/2\langle 110 \rangle$, a is the lattice constant due to the shortest vector [36]. This burger vector is perpendicular to the dislocation direction. However, the lowest energy dislocation line has a 60° rotation from $a/2\langle 110 \rangle$ and this dislocation referred as 60° dislocation. 60° dislocation will eventually dissociate into two partial dislocations. One of the most important slip system in CZT is Shockley slip system, which explain the dissociation of the perfect 60° dislocation as follows (**Eqn 1**) [22]:

$$\frac{1}{2} [1\bar{1}0] \rightarrow \frac{1}{6}[1\bar{2}1] + \frac{1}{6}[2\bar{1}\bar{1}] \quad \text{Eqn 1}$$

Dislocations and dissociation of dislocations in FCC crystals can be described by the Thompson's tetrahedron shown in **Figure 3** [20]. The face of the Thompson's tetrahedron is parallel to the four different sets of $\{111\}$ planes and in the direction of (110) slip planes.

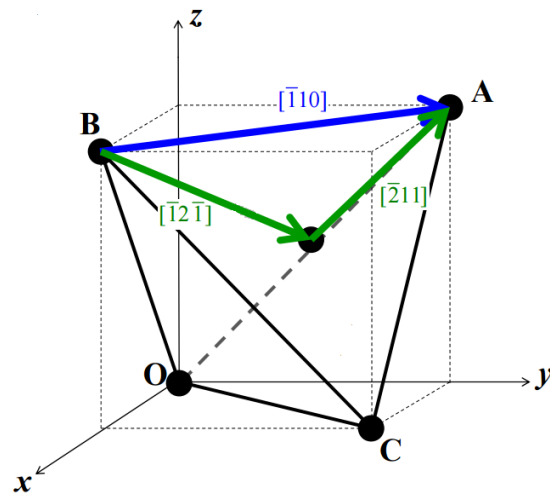


Figure 3 Partial dislocations in Thompson's tetrahedron in FCC crystals.

The region confined by these two partial dislocation causes a stacking fault in the crystal structure. 60° dislocations can be classified as glide and shuffle dislocations. Glide (g) dislocation caused by breaking of bonds between atoms spaced closely while shuffle (s) dislocation formed by breaking of bonds between atoms spaced widely (**Figure 4**) [30].

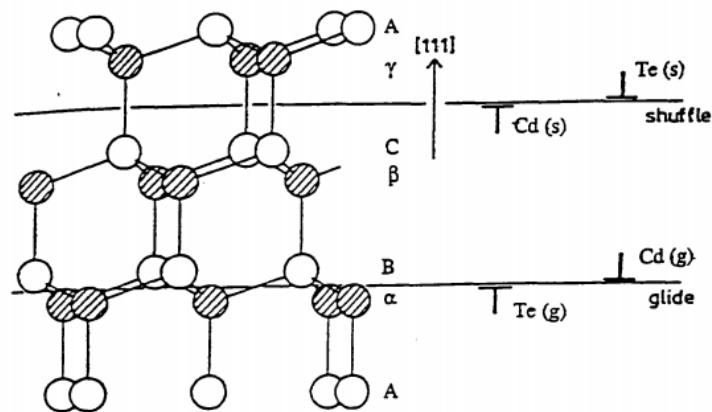


Figure 4 Types of dislocation found in the Sphalerite structure [30].

By indenting $\{111\}$ surface of the crystal, a micro deformation occurs that causes a complicated geometry since several specific $\{111\} \langle 110 \rangle$ slip systems get activated simultaneously. As stress is applied, dislocations tend to form a three dimensional arrangement of $\langle 110 \rangle$ glide prisms [33]. In **Figure 5**, deformation mechanism of dislocations is shown. From this figure, it can be seen that α and β dislocations are expanding into the crystal along the $\langle 110 \rangle$ directions on (111) surface. Slip systems are generated as tangential (burger vectors $\pm \mathbf{b}_1$) and tetrahedral (burgers vectors \mathbf{b}_2 , \mathbf{b}_3) slip processes. The half loop contains 60° and screw dislocations resulting from parallel and tetrahedral glide process on $(111)\text{Te}$ face.

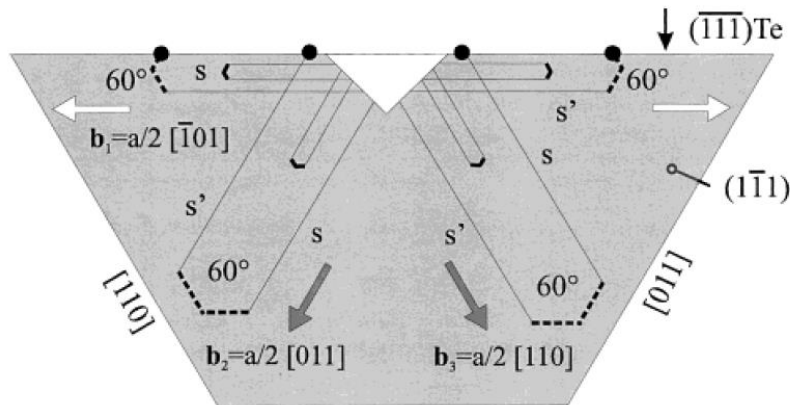


Figure 5 Model of Cd and Te related dislocation [33].

2.2.2 Stacking Faults

Stacking faults are the most observed defects in CZT matrix. Stacking fault can be described as a long-range disturbance in the stacking arrangement of molecules. Stacking fault width can be determined by the differences between inner and outer layer of interruption. Stacking faults cause plastic deformation in the crystals and this deformation can be in the form of dislocation loop or misfit dislocation [37].

Stacking faults in CZT can have two forms that are intrinsic and extrinsic stacking fault. Intrinsic stacking fault is generated when a plane is missing from stacking sequence; while extrinsic stacking fault is generated when there is an extra plane in the stacking sequence. CZT is less stable in sphalerite form, which leads to low stacking fault energy causes formation of large number of twins and stacking disorder in the grown bulk of the crystal [22]. Stacking faults form only in a few atomic spaces so the difference between stacking fault and twins is the change in the size of the stacking sequence.

2.2.3 Twins and Twin Boundaries

Twins are macroscopic defects encountered in CZT and results from crystallographic structure of CZT. CZT has a zinc blende structure with a crystallographic symmetry group of ($F\bar{4}3m$). Formation of twins depends on three energy changes in the crystalline structure: *i.* minimizing crystalline energy, which is related to partial dislocation, *ii.* the interfacial energy related to twin boundary and dislocation core, *iii.* elastic energy associated with slip bands. These three energy changes determine the size, shape and the orientation of the twins [38].

CZT has a highly ionic bonding, which causes some part of the crystal to have hexagonal structure resulting in twins. Cadmium and tellurium bonds have a high ionicity property and results in a low stacking fault energy. Increasing ionicity of the bonds causes a decrease in the formation energy of defects. Therefore, CZT has a tendency to generate twins, dislocations, and stacking faults [39]. Twins are observed most commonly at (111) face of the CZT crystal.

Twins are disorder in stacking sequence of closed packed planes and twin boundary can be described as special interfaces in the crystal structure. Twins and twin boundaries in CZT have low formation energy and low formation volume [40]. Twin boundary, which has the same coordinate as real matrix is different from grain boundary, which has totally different coordinate from the real matrix. Representation of the twin boundary can be shown by the use of stacking order of {111} planes in FCC structure. Stacking sequence can be written as ABCABCABC and if a twin boundary is initiated in this sequence, the order becomes ABCABACBA [41]. As can be seen, the usual stacking sequence is altered by introducing a twin boundary.

Twins and twin boundaries formed from unstable solid-liquid interface and thermal stresses at high temperatures and during cooling. Twins are formed in order to reduce the Gibbs energy of grain boundaries and generated by misorientation of atoms in some part of the disturbed interface caused by supercooling, asymmetrical thermal

distribution and impurities [42]. Grain boundaries and crucible walls are considered to initiate the formation of twins. Dislocations at twin boundaries can be transmitted easily due to their high interfacial energy and weak bonding and these dislocations cause a misfit in the lattice between the two grains [42].

Twins can be classified as stress induced twins and growth twins. Stressed induced twins are formed by the generation and slip of the partial dislocation on $\{111\}$ planes. Stress induced twins are originated from slip of the dislocations and twins are nucleated and propagate in the crystal through the slip mechanism. Stress induced twins are the result of process of partial dislocation nucleation and slip on planes [38]. When a dislocation nucleates and slips, energy changes take place, such as crystalline energy, stacking fault energy and energy of partial dislocations [38]. However, growth twins are formed during the crystal growth as a result of stresses caused by the interaction between crucible and crystal and uncontrolled temperature change in cooling process [32, 38, 43]. By decreasing the interaction between crucible and the crystal, the formation of twins can be decreased in some extent. Instead of using quartz crucible, using carbon-coated quartz [44], graphite [45], or pBN (pyrolytic boron nitride) crucible [46] can decrease the sticking of the crystal to the quartz wall and thus, high quality crystals can be produced. By controlling connection between the melt materials and crucible, one can avoid generation of twins and achieve high quality crystals [19] In addition, a better-controlled cooling profile can decrease the number of twins generated within the crystal [32].

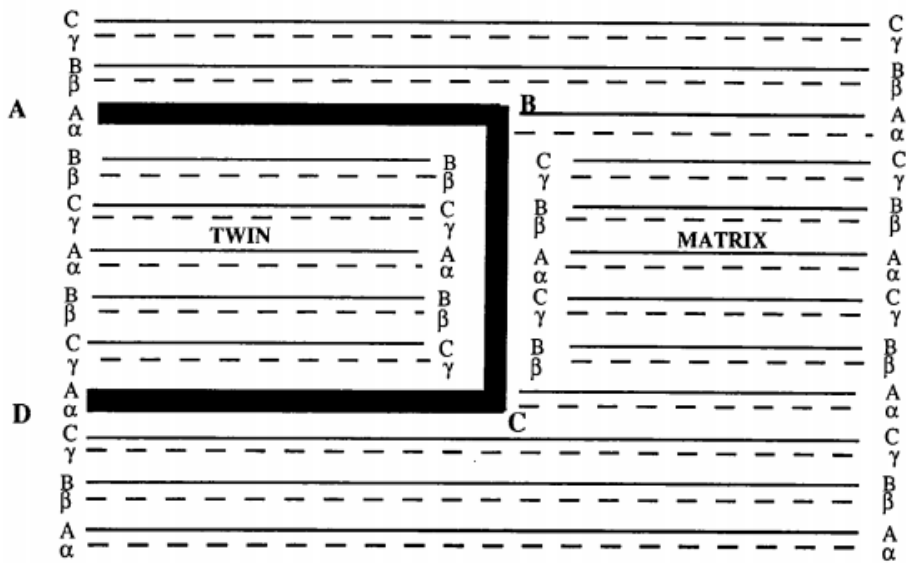


Figure 6 Stacking sequence of twin boundary of sphalerite lattice [30].

First order twin orientation can be found by rotating the matrix by 180° about $\langle 111 \rangle$ axis as shown in **Figure 6**. This matrix operation can be repeated to find higher twins by rotating the first twin about (111) axis. However, first order twin has low formation energy, so it is possible that crystal has a tendency to generate more first order twins in its structure [13].

2.2.4 Precipitates and Inclusions

Te precipitates/inclusion may also generate dislocation in crystal matrix due to the thermodynamics driving force of Te precipitates in the lattice and the difference between thermal expansion of Te inclusion and CZT matrix and by generation of stress in the lattice [22]. Te precipitates and inclusions are important defects that affect the performance of the CZT materials [47]. They negatively affect IR transmission,

worsen the crystal's lattice and give rise to defect density in CZT material [48]. The main differences between inclusions and precipitates are the change in the size and the formation mechanism of these defects. The size of Te precipitates change between 10 and 50 nm measured by TEM [49], while Te inclusions have diameters between 1 and 50 μm [1].

Precipitates generally originate from the segregation of Te atoms, while inclusions originate from the change in the growth interface and get affected by growth rate [47]. Growing bulk CZT crystals from melt causes precipitate incorporation in to the matrix due to the high growth temperature and restriction of phase diagram of the CZT crystal [49]. Unstable cooling process is the main reason for the creation of Te precipitates and they originate from the retrograde solid solubility of the phase diagram of the CZT crystal [50]. Melting point of Te is 450 $^{\circ}\text{C}$ and CZT has a solidification temperature of 1100 $^{\circ}\text{C}$. Due to the temperature differences, the solubility of the Te is retrograded during the cooling process and Te precipitates joined in the CZT matrix [51]. During the cooling process, Te precipitates become denser and result in Cd vacancies and Te interstitials. Te precipitates are also generated due to the native defects and they can be considered as point defects [1].

On the other hand, Te inclusions are formed due to the excess Te in the melt CZT at high temperatures [22]. Although starting material is stoichiometric or Cd rich, Cd will eventually evaporate and result in the formation of Te rich material. Te rich material causes unstable interface during the nucleation due to the thermal solubility of Te [52]. Therefore, Te inclusions are initiated by the instability in the growth interface. Te rich melt droplets are captured before solidification occurs at the growth interface and they can migrate during the cooling process due to the change in the temperature gradient [32, 53]. Unstable growth interface is caused by a change in temperature, mechanical vibration, and supercooling. Due to the temperature variation during the crystal growth, achievement of a stable interface throughout the growth process is very difficult. The growth interface has a convex shape at the beginning of growth, becomes

flat at the middle of the growth and then turns in to a concave shape at the end of the growth, which causes crystals to have imperfections [47]. In addition, unstable growth rate and temperature variation of the furnace can negatively affect the crystal perfection. It is very difficult to control the growth rate, which causes Te inclusions vary in size and distribution throughout the CdZnTe crystal [47]. Three types of inclusions can be found in CZT crystals, which are square, hexagonal and triangular shaped [48, 53, 54]. Triboulet (2010) proposed that Te has a rounded shape when it is small in size; whereas larger Te has facets. Hexagonal shape Te precipitates/inclusions are most commonly encountered and the shape of Te precipitates/inclusions actually depends on the crystallographic projection [22].

Te precipitates and inclusions are observed by chemical etching and then can be analyzed by optical microscope and SEM. According to Wada (1988), Te precipitates density is the same as dislocation density in sample measured using Nakagawa etchant [22]. In addition, Te precipitates and inclusions can be observed by IR transmission microscope and TEM [51]. TEM characterization used to identify nano-scale Te precipitates provides information about the origin of the precipitates. Annealing samples with Cd overpressure can be done to reduce Te precipitates and decrease the size of Te inclusions by migration mechanism [22, 55]. Another method used to reduce Te inclusions and precipitates is based on stirring the melt during the growth process and growth with Cd excess in the starting material so that stoichiometry is conserved [22].

2.2.5 Grain and Grain Boundaries

Grain size range from few micrometers to several millimeters and grain boundary is the interface between grains [22]. Atoms at the grain boundary have more energy than atoms in the grain. For this reason, grain boundaries are chosen as areas for dislocation propagation and they can be etched very easily. Temperature fluctuation of the growth

process and high growth rate cause formation of grain boundaries [32]. Supercooling generates small size grains while slow and controlled cooling produces large grains.

2.2.6 Cracks

According to Triboulet (2010), cracks form due to the thermal or mechanical stress caused by interaction with the ampoule or cooling processes. Crack size is in the range of a few cm in length and 25 μm in width. Cracks initiate near the ampoule wall and propagate to the CZT crystal. Slicing, dicing, lapping and polishing processes may also initiate the formation of cracks formation. Cracks can be removed or at least decreased by appropriate crucible material, suitable thermal profile, stable cooling procedure and convenient surface treatment [32].

2.3 Etching of CdZnTe

Chemical etching is used to reveal dislocations, Te precipitates/inclusions, low-angle boundaries (dislocation walls), twins and twin boundaries in CdZnTe crystals without removing excessive material. The shape of the etch pits and the rate of the etching depends on the orientation of the sample [56]. The densities of these defects are measured directly by counting etch pits, which form at the exit points of dislocations on the surface of CZT [1]. The density of dislocation (EPD) is an important indicator of good quality of CZT crystals. [57]. There are several different etchants used to reveal the defects in CdZnTe crystals; but specifically Nakagawa solution is used as an industrially standards etchant [22, 25, 26, 29, 58]. After etching, defects can be observed by optical microscopy, SEM and infrared microscopy.

Defects are the locations where surface reactions take place under chemical etching processes. Single geometrically regular pit indicates the exit point of one dislocation whereas dislocation walls is the linear association of etch pits present on the surface.

Surface controlled interaction results from different activation energy of defects and local stress fields existing in the CZT crystals. Due to the stresses caused by dislocations, the surface of the crystal would be easily etched by a suitable etchant which removes the surface layer by layer and geometrically regular etch pits are formed on the surface.

It is impossible for a single etchant to reveal all defects types in CZT crystals. Some etchants only reveals one type of defects, while other can reveal different type of defects. Different etchants have different reactions with CZT due to the difference in chemicals and their reactions. Generally, during the etching process, strong acids attack the CZT crystals and form Cd and Te ions in the solution. Te ions react with the solution and the Te ions turn into either gaseous H_2Te that evaporates from the solution or TeO_2 that is insoluble in water. In addition, some of the Te atoms may precipitate and a black layer is observed on the surface [57].

Although the sample surface is flat and smooth after mechanical polishing, the surface may have some imperfections such as impurities, grain and subgrain boundaries and sub-surface damages are introduced to the crystals by mechanical polishing. In addition, lapping and polishing processes scratch the surface of CZT crystals and these processes tend to weaken the bonds in the crystal, which results in a reaction with acidic solutions and might increase the etch pit density. Therefore, chemical polishing gets great attention in order to clean the surface.

Etching process includes two different types, namely polishing and crystallographic etching. Both types include transportation of the reactants, reaction with the surface, and transportation of reaction products from the surface to the solution. Diffusion limited etching is dominant when etch rate is determined by the diffusion of reactants to the surface. Reaction rate limited etching is dominant when the etch rate is determined by the transportation of reaction products. Diffusion limited etching is called polishing since it does not depend on the surface orientation. However, reaction rate limited etching depends on the crystallographic orientation of the surface. Etching

rate is changed throughout the surface i.e. enhanced or reduced etching rate depending on strain fields around dislocations or defect-free fields.

The formation of the etch pits depends on the balance of the rate of oxidation and dissolution. If the rate of one reaction exceeds the other, the shape of the etch pits change. Etchants are sensitive at preferential sites. Therefore, the reaction is faster at these sites due to the higher stress concentration. These sites are the certain points where dissolution begins and proceeds in certain directions. The rate of etching of these sites depends on the oxidation solution. Some etching agents are active and form pits on low energy surfaces (i.e. $\{111\}$) while other agents are active both on high (i.e. $\{100\}$) and low energy surfaces.

2.3.1 Etch Pit Formation

The nature of dislocations and the angle at which dislocations intersect with the surface affect the morphology of the etch pit. If the dislocation is perpendicular to the surface, symmetrical etch pit will form. When a deviation occurs, asymmetry in etch pit formation is observed. In addition, dislocation line cannot disappear in the crystal structure. As a result, etch pits correspond to dislocation reappear after repeated etching and increasing etching time will cause etch pits to widen and deepen. Etch pits at the same site, which correlated with dislocations increase in dimension and depth as the time is increased. All the etch pits at the same surface do not have the same size and depth due to time lag in the formation of these etch pits. Etchants attack the surface, through layer by layer removal, new sites are exposed and form etch pits.

Etch pits revealed in a certain orientations stand for dislocations that form on that orientation in the crystal as shown in **Figure 7**. The change in etch pits' geometry corresponds to dislocations formed along different orientations. The microstructure and etch patterns on habit faces can differ considerably. Firstly, According to Inoue (1962), triangular etch pits on $\{111\}$ surfaces has edges parallel to $\langle 110 \rangle$ directions

and the sides of the etch pits have the same size. Etch pits form at $\{111\}$ B plane (**Figure 7d**) are in the shape of pyramidal or conical triangle, while pits on $\{111\}$ A (**Figure 7d'**) are in flat bottom triangle. Isosceles triangular etch pits form on $\{110\}$ surface (**Figure 7c&c'**) and it corresponds to $\frac{1}{2}$ tetrahedron. In addition, etch pits on $\{211\}$ surface has sides with $(0\bar{1}0)$, $(\bar{1}00)$ and $(\bar{1}\bar{1}\bar{2})$ planes. Lastly, rectangular etch pits revealed on $\{100\}$ surfaces and the sides of the etch pits are parallel to the $\langle 110 \rangle$ directions [25]. Etch pits on $\{100\}$ A and $\{100\}$ B are at right angles to each other (**Figure 7b&b'**).

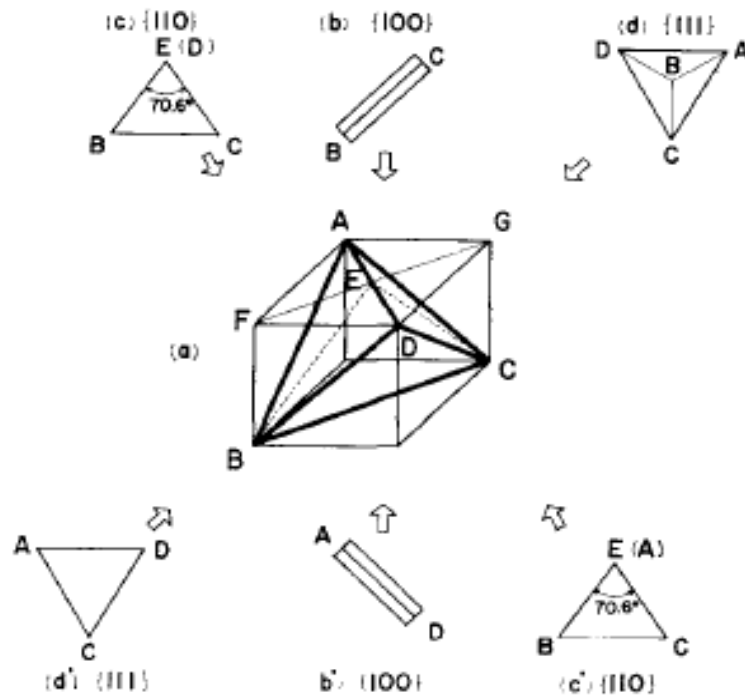


Figure 7 The shape of etch pits on different orientations [25].

However, the geometry of the etch pits may also differ on the same surface of the CZT crystal. According to X.P. Cui [59], by using Everson Etchant, four different etch pits can be detected on {111} face. Namely, triangular pyramidal pits, flat bottom pits, comet shaped pits and irregular triangular pyramidal pits. All pits are in a certain direction which show etch pits are originating from dislocations. In addition, X.P. Cui shows in his study that triangular pyramid etch pits is observed in five different shape. From these studies, we can realize that dislocations in CdZnTe crystal are complex and our knowledge is limited.

2.3.2 Etchants and their chemical reactions on CZT crystals

Etching is a dissolution reaction, which has a mechanism of transport or surface controlled reactions. Chemical etching process involves three steps. The first step is transportation of the reactants to the surface of the crystals. Secondly, the surface reaction takes place by a process of electron transfer i.e. one or more species can be oxidized and others reduced simultaneously. Finally, the products are transported from the surface to the solution [32].

Chemical etching is an important process for removing the amorphous layer near the surface, for cleaning the crystal surface after final polishing, for revealing the polarity of the faces and for finding the density of dislocations to assess crystal quality. In addition, it can be used for oxidizing the surface prior to the electrode deposition on the detectors.

As tabulated in **Table 1** [22], there are many different etchants that were developed by Inoue, Nakagawa, Bagai, Chen, and Everson [5]. A review of these etchants is given below.

Table 1 Commonly used dislocation revealing etchants for family of CdTe [22]

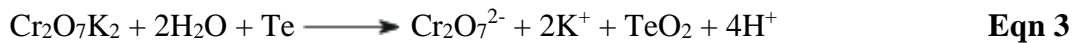
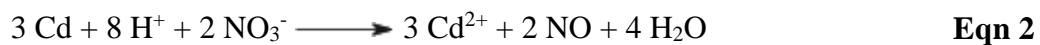
Etchants	Notes on the action of Etchants
<p style="text-align: center;">Inoue, 1962 EAg-1 & EAg-2 Etchants HNO₃ : H₂O : K₂Cr₂O₇ : AgNO₃</p>	<p>Effect both A and B face of the crystal. Crystallographic shaped pits are formed. Irregular shaped pits formed on {111}A face. Polarity determination (crystallographic analysis). Stirring can affect the etching. It is not a reliable dislocation etchant due to unstable etching mechanism.</p>
<p style="text-align: center;">Nakagawa, 1979 H₂O : H₂O₂ : HF (2:2:3)</p>	<p>Commercial etchant Effect {111}A face of the crystal. Rounded pits are observed. Revealing dislocations and assessing EPD.</p>
<p style="text-align: center;">Everson, 1995 HF : HNO₃ : Lactic acid (1:4:25)</p>	<p>Effect {111}B and {211}B face of the crystal. Give similar result with Nakagawa etching. Etch pits formed on B face is related with α and β dislocations.</p>
<p style="text-align: center;">Saucedo, H₂O : HNO₃ : HF : AgNO₃</p>	<p>Reveal dislocations, twin and twin boundaries, grain and grain boundaries.</p>
<p style="text-align: center;">Bagai, 1990 HF : H₂O₂ : H₂O (4:0.5:2)</p>	<p>Affect on {111}B face. Reveal α and β dislocations.</p>

2.3.2.1 Inoue Etching

Inoue proposed three different solutions for the family of CdTe crystal namely E-solution, EAg1 solution and EAg2 solution. E-solution contains nitric acid (HNO₃), DI water (H₂O) and potassium dichromate (K₂Cr₂O₇), which is used for chemical polishing of the surface. Bissoli (2004) reported that the etch duration should be 1 minute. Inoue EAg1 and EAg2 solutions contain nitric acid (HNO₃), DI water (H₂O), potassium dichromate (K₂Cr₂O₇) and silver nitrate (AgNO₃), which is used to reveal density of dislocations and distribution of Cd and Te dislocations.

EAg1 solution which has lower silver concentration reveals etch pits on {111}A, {111}B, {110} and {100} surfaces of CdTe. On the other hand, EAg2 solution with higher silver concentration only reveal etch pits on {111}B surfaces. Inoue's EAg1 solution consists of 20 ml H₂O + 10 ml HNO₃ + 4g K₂Cr₂O₇ + 1.5 mg AgNO₃. Inoue's EAg2 solution contains higher silver concentration and it consists of 20 ml H₂O + 10 ml HNO₃ + 4g K₂Cr₂O₇ + 30 mg AgNO₃. EAg1 and EAg2 etchants are thought to reveal two different types of dislocations namely Cd (α) and Te (β) dislocations respectively. According to Inoue (1962), no precipitates are revealed by these two etchants.

The action of Inoue etchants can be described as follow;



Nitrate ions react with cadmium atoms (**Eqn 2**) while potassium dichromate attacks Te forming TeO₂ (**Eqn 3**). TeO₂ is insoluble in water, while it is soluble in acidic solutions. Finally, silver ions do not only stop the dissolution process; but also, produce etch pits selectively with respect to a change in surface energy of dislocations.

2.3.2.2 Nakagawa Etching

It was reported that Inoue etchants cannot reveal fresh dislocations (see section **2.2.1 Dislocations**) in the crystals under normal conditions. Thus, Nakagawa (1979) found a better solution for revealing fresh dislocations in CdTe and CZT crystals. Nakagawa solution contains DI water, hydrofluoric acid that forms Cd and Te ions and cations, hydrogen peroxide that oxidizes Te atoms. Nakagawa etchant is a commercial solution of revealing dislocations in CZT crystals and EPD obtained from this solution is used as a standard for assessing the density of dislocations. However, Nakagawa etchant has some limitation that it can only reveal dislocations on $\{111\}A$ surface on the crystals. Nakagawa etchant cannot reveal dislocations on Te $\{\bar{1}\bar{1}\bar{1}\}$ and Te $\{\bar{2}\bar{1}\bar{1}\}$ faces used for epitaxial growth.

2.3.2.3 Everson Etching

Nakagawa solution does not reveal dislocations on Te $\{\bar{1}\bar{1}\bar{1}\}$ and Te $\{\bar{2}\bar{1}\bar{1}\}$ faces which are important surfaces for epitaxial growth. For this reason, Everson developed another etchant, which (Everson, 1995) reveals dislocations on $\{111\}B$ and $\{211\}B$ surfaces and it is developed for the production of etch pits on $\{111\}B$ surface. In addition, etching with Everson solution gives the same Etch Pit Density as Nakagawa solution on $\{111\}A$ surface.

Everson solution contains lactic acid, hydrofluoric acid and hydrogen peroxide. Lactic acid is used as a buffering agent, while hydrofluoric acid attacks the crystals and forms Cd and Te ions and cations in the solution. Cd and Zn cations form strong complexes with lactate and dissolve in the solution. Moreover, hydrogen peroxide oxidizes Te ions and consequently TeO_2 would be soluble in the solution and etch pits are formed on the surface of the crystals by preferential attack of Te atoms.

Everson etchant reveal two different triangular pits on {111} and {211} surfaces, which are correlated with α and β dislocations. Nearly all etch pits are flat bottomed and have the same size. According to Everson (1995), α and β dislocations represented by equal angle triangles with opposite polarity on {111}B surface. When {211}B surface is considered, α dislocation turns into an obtuse triangle, while β dislocation grows into acute triangle due to the crystallographic projection that are shown in **Figure 8**. Etch pits with different type of geometry represent different dislocations in the crystal. In addition, when the same crystal is considered, etch pit density on {111}B face has same EPD with respect to {211} face.

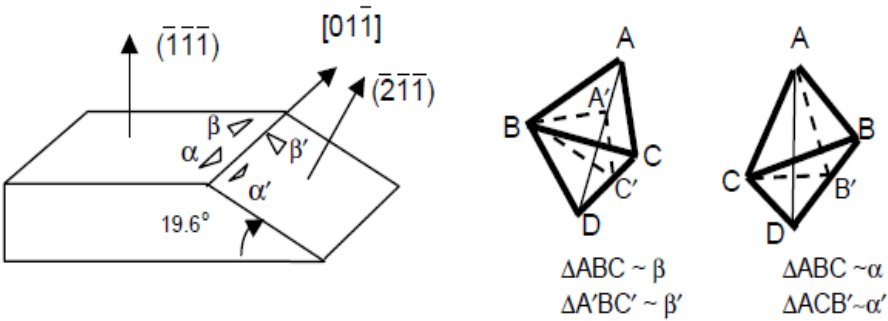


Figure 8 Etch pits on {111}B and {211}B surfaces with two different kinds of dislocations [60].

2.3.2.4 Saucedo Etching

Saucedo Etchant can reveal grains, grain boundaries, twins and micro-twins. In addition, this etchant is supposed to reveal dislocations on the surfaces and the shape of the etch pits show similarities with respect to other specific etchants. Saucedo

etchant consists of H₂O (20 ml) + HNO₃ (15 ml) + HF (5 ml) + AgNO₃ (0.4 g) and the etching time is 2 minutes [61].

2.3.2.5 Bagai Etching

Inoue etchants has some drawbacks to reveal {111}B face and it is assumed that it cannot reveal all the dislocations on this face. Bagai etchant is produced as an alternative solution to reveal {111}B face, which has an importance for epitaxial growth. Bagai solution (HF:H₂O₂:H₂O 4:0.5:2) contains chemicals exactly the same with Nakagawa solution; but, with reduced oxidant concentration. Bagai etchant is supposed to reveal all dislocations on {111}B surface and two etch pits are formed associated to α and β dislocations.

2.3.2.6 Bromine Methanol Etching

Cutting of the substrate from CZT ingots and mechanical polishing induce impurities and subsurface damages to the surface of the substrate, which can be eliminated using chemicals such as bromine (Br) and alcohol including methanol, ethanol or propanol. For cleaning of CZT surface prior to detector fabrication, Bromine Methanol (B-M) chemical etching is used mostly to remove scratches and produce smoother surface. According to Zheng (2012), B-M solution can clean the surface and the surface have the lowest roughness value than using ethanol or propanol [32]. The surface composition depends on the PH of the B-M etchant and on the concentration of Br in solution. The chemical reaction between CdZnTe and B-M etching is described by the equation:



The CdBr_2 compound is soluble in bromine (**Eqn 4**). Thus, Br preferentially reacts with Cd atoms leaving behind a Te rich surface. Moreover, when Te rich surface is exposed to air, TeO_2 and CdO compounds formed during the oxidation process. As a result, the process is achieved in three steps including electron transfer process, oxidation of Te atoms and transfer of CdBr_2 to the solution.

Optimization of chemical etching and control of acidity of etchant and reproducibility of smooth and clean surface is difficult process. Zheng (2012) has tried chemical etching with different concentration of bromine for 2 minutes etching time. 1% B-M etching is not sufficient to remove polishing residues such as alumina or carbon from the surface. As the etchant concentration is increased, polishing residues is decreasing while Te and Cd concentration is increased on the surface. However, increasing the concentration of Br more than 5% in the solution will degrade the surface quality of the substrate.

2.3.2.7 Determination of Crystallographic Polarity

CdTe shows crystallographic polarity due to its sphalerite structure, which has non-centrosymmetric structure. In other words, pairs of opposite crystal planes i.e. $\{hkl\}$ and $\{\bar{h}\bar{k}\bar{l}\}$, show different structure and chemical properties. In sphalerite structure of $\{111\}$ face, each surface ended with Cd or Te single atom which has triple bonds with atoms beneath and these bonding formation will be tetrahedral as shown in **Figure 9**. Addition of a Te (or Cd) atom to the Cd (or Te) terminated surface connected by a single bond will be less stable than that of tetrahedral connection. Consequently, $\{111\}$ stable faces of sphalerite structure have different polarity according to the atoms (Cd or Te) terminated on the surface. If the plane terminates with non-metal atom (Te) called $\{\bar{1}\bar{1}\bar{1}\}$ or B face and the plane terminates with metal atom (Cd) is called the $\{111\}$ or A face. This property is important for epitaxial growth and chemical etching processes.

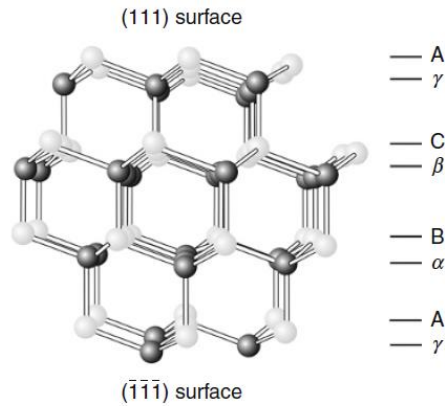


Figure 9 Cd and Te terminated surfaces in the sphalerite structure [22].

The $\{hkl\}$ and $\{\bar{h}\bar{k}\bar{l}\}$ planes give same intensities in the X-Ray diffraction analysis. For this reason, etching method has great importance to determine the polarity of the crystals. Etching process demonstrates distinct differences between polar surfaces. The polarity of the crystals was first studied by Warekois, Lavine, Mariano, and Gatos (1962) using hydrofluoric acid, hydrogen peroxide and DI water (3:2:1). According to their studies, Te terminated or $\{\bar{1}\bar{1}\bar{1}\}$ B face was heavily pitted with respect to Cd terminated or $\{111\}$ A face. Later, Nakagawa, Maeda, and Takeuchiz (1979) used the same chemicals with different concentration and again it was claimed that the pitting is on Te surface, which gives the correct orientation for epitaxial growth. According to Triboulet (2010), epitaxial growth on $\{\bar{h}\bar{k}\bar{l}\}$ Te surface gives better quality while assigning etch pit density should be done on $\{111\}$ Cd surface. Using this argument, epitaxial growth done on the CdTe substrate and orientation was checked. There was a contradiction with the studies done by Fewster, Cole, Willoughby, and Brown (1981). Inconsistency between these results was solved by Fewster and Whiffin (1983) showing that $\{111\}$ Cd surface becomes pitted while the $\{\bar{1}\bar{1}\bar{1}\}$ Te face was polished after etching [62]. Brown (1990) found a better etchant, which can reveal the polarity

of the crystals using hydrofluoric acid, nitric acid and acetic acid (or lactic acid) with a volume ratio of 1:1:1. This etchant gives matt black surface on {111}Cd and bright shiny surface on $\{\bar{1}\bar{1}\bar{1}\}$ Te. Immediate washing of the sample is needed after etching and polarity of the surfaces can be determined by naked eye.

CHAPTER 3

EXPERIMENTAL PROCEDURES

In this chapter, surface processing and etching procedures of CZT crystals are described. The cutting and mechanical polishing process applied in this work discussed in section 3.2.1; while chemical polishing described in section 3.2.2. B-M solution is employed for chemical polishing processes. Determination of crystallographic polarity discussed in section 3.2.3. Etching procedures and characterization techniques discussed in section 3.3. Different etchants are applied on {111}, {110} and {211} faces to reveal dislocations, precipitates, inclusions and twins in the CZT crystals. The formation of etch pits are investigated using different characterization techniques. Defects also investigated using TEM, which are described in section 3.4.

3.1 Sample Information

Samples used in this thesis named in accordance with their origin and orientation. The wafers from China were named as “Commercial” with addition of a letter that shows the orientation of the sample, while wafers produced at METU were named as MT with their orientations. For example MT1_S1 wafer stands for the first slice of the first grown ingot at METU with {111} orientation. **Table 2** shows the names and formulas of the samples with their orientations. Moreover, the processes that the samples were exposed were shown with different characterization analyses.

Table 2 Sample naming in accordance with origin, orientation and processes

#	Name	Formula	Orientation	Process	Analysis
1	Commercial_W1	Cd _{0.96} Zn _{0.04} Te	{211}	Bromine Methanol	XPS
2	Commercial_W2	Cd _{0.96} Zn _{0.04} Te	{211}	E-Reagent	XPS
3	Commercial_W3	Cd _{0.96} Zn _{0.04} Te	{211}	Polished	XPS
4	Commercial_W4	Cd _{0.96} Zn _{0.04} Te	{211}	2 min Nakagawa Etching + air exposure (oxidation)	XPS
5	Commercial_W5	Cd _{0.96} Zn _{0.04} Te	{211}	2 min Nakagawa Etching + Subsequent Analysis	XPS
6	Commercial_W6	Cd _{0.96} Zn _{0.04} Te	{211}	Nakagawa etching + etch pit dimension	SEM
7	Commercial_W7	Cd _{0.96} Zn _{0.04} Te	{211}	1 min Everson Etching	SEM
8	Commercial_W8	Cd _{0.96} Zn _{0.04} Te	{211}	2 min Everson Etching	SEM
9	Commercial_W9	Cd _{0.96} Zn _{0.04} Te	{211}	3 min Everson Etching	SEM
10	Commercial_W10	Cd _{0.96} Zn _{0.04} Te	{211}	1 min Inoue EAg2 etching + Etching rate for 10 min	SEM
11	Commercial_W11	Cd _{0.96} Zn _{0.04} Te	{211}	4 min Bagai Etching	SEM
12	MT_M1	Cd _{0.9} Zn _{0.1} Te	Multi-grain	FIB	TEM
13	MT_W2	Cd _{0.96} Zn _{0.04} Te	{211}	1 min Inoue EAg2 etching	SEM
14	MT1_R1	Cd _{0.96} Zn _{0.04} Te	{220}	Inoue EAg2 Etching	SEM
15	MT1_S1	Cd _{0.96} Zn _{0.04} Te	{111}	Mech. & Chem. Polishing + Inoue EAg2 etching	AFM + SEM
16	MT1_S2	Cd _{0.96} Zn _{0.04} Te	{111}	Inoue EAg1 Etching rate for 6 min	SEM
17	MT1_S3	Cd _{0.96} Zn _{0.04} Te	{111}	2 min Inoue EAg2 etching + Bagai etching + Nakagawa etching + Everson etching	SEM
18	MT1_S4	Cd _{0.96} Zn _{0.04} Te	{111}	1 min Nakagawa etching + etching rate analysis	SEM
19	MT1_S5	Cd _{0.96} Zn _{0.04} Te	{111}	2 min Nakagawa etching	SEM
20	MT1_S8	Cd _{0.96} Zn _{0.04} Te	{111}	1 min Inoue EAg2 etching + as-cut surface	SEM
21	MT1_S9	Cd _{0.96} Zn _{0.04} Te	{111}	2 min Saucedo Etching	SEM
22	MT1_M1	Cd _{0.96} Zn _{0.04} Te	Multi-grain	2 min Saucedo Etching	SEM
23	MT2_S1	Cd _{0.96} Zn _{0.04} Te	{111}	Everson Etching rate for 20 min	SEM
24	MT2_S2	Cd _{0.96} Zn _{0.04} Te	{111}	Nakagawa Etching rate for 15 min	SEM
25	MT2_S3	Cd _{0.96} Zn _{0.04} Te	{111}	Inoue EAg2 Etching rate for 6 min	SEM
26	MT2_S4	Cd _{0.96} Zn _{0.04} Te	{111}	30 sec Saucedo Etching	SEM
27	MT2_W5_1	Cd _{0.96} Zn _{0.04} Te	{211}	1 min Saucedo Etching	SEM
28	MT2_W5_2	Cd _{0.96} Zn _{0.04} Te	{211}	1 min Inoue EAg2 Etching	SEM
29	MT4_M1	Cd _{0.96} Zn _{0.04} Te	Multi-grain	1 min Inoue Etching	SEM

3.2 Surface Process of CdZnTe Crystals

The preparation of crystal surfaces has a great importance in the fabrication of CZT substrate. Mechanical damage and surface contamination or nonstoichiometric surface of the substrate adversely affects the quality of epitaxial layer. Surface processing was done prior to the investigation of defect structure of samples by chemical etching processes and TEM. This section describes the surface processing that includes a series of slicing, lapping, mechanical, and chemical polishing processes. Mechanical polishing procedures and the choice of chemical polishing reagent used were also described.

3.2.1 Slicing and Mechanical Polishing

Crystal ingots were mounted on a goniometer and the largest grains in them were cut out. Parallel cutting of the plane along the twin boundaries was performed and $\{111\}$, $\{211\}$, $\{110\}$ planes were obtained using twin growth direction. Twin boundaries are known to grow in the $\{111\}$ plane direction. As a result, cutting procedures were accomplished using twin boundaries in CZT crystals. The cutting process generates damage and rough surface. Mechanical polishing can reduce the damage resulting from cutting and can be used to obtain flat surfaces. Throughout this work, mechanical polishing was carried out using a polishing and lapping system. All samples were usually polished with first 9 μm alumina powder and then by 3 μm alumina powder in order to remove saw damages and surfaces that is free of scratches were obtained.

Total thickness of each CZT sample was measured using contact thickness measurement gauge after each polishing procedure. After mechanical polishing, samples were investigated with both naked eye and AFM to view surface morphology and obtain roughness values.

3.2.2 Chemical Etching for Final Polish

A chemical polishing agent is different from a chemical etchant in which it dissolves the surface of the wafer in a uniform way without removing material from the points where crystal defects exist. Ideally, chemical polishing solutions have to generate stoichiometric surfaces.

Change in CZT surface composition and surface oxidation after chemical etching were investigated by XPS measurement. For XPS experiments, PHI 5000 VersaProbe Scanning X-Ray Photoelectron Spectrometer (XPS) with an energy resolution of 0,65 eV was used. The system has a spot size diameter of 0.1 mm.

B-M solution is the most used polishing agent, which dissolves CZT samples and form Cadmium Bromine (CdBr_2) salt that is soluble in bromine solution. Commercial_W1 polished with %1 solution of B-M for 10 seconds and immediately rinsed with methanol to investigate whether surface stoichiometry was maintained using XPS analysis.

E-solution consisting of $\text{K}_2\text{Cr}_2\text{O}_7 + \text{HNO}_3 + \text{H}_2\text{O}$ was used as a chemical polishing solution for 10 seconds and rinsed with DI water on Commercial_W2 so that comparison with Bromine methanol solution was investigated. The resultant surface composition was examined by XPS analysis.

3.2.3 Crystallographic Polarity Determination

The etching solutions revealing crystallographic polarity was also investigated. The Brown etchant consisting of HF, HNO_3 , and CH_3COOH or Lactic acid (1:1:1) were used for this purpose. In this case, the surface morphology of CZT crystals i.e. pitting produced on samples, were investigated by naked eye.

Brown solution was used for 20 seconds and immediately rinsed with DI water. Polarity of the samples was determined by naked eye. Cd terminated or A face was heavily pitted and matt black surface is obtained. The surface was covered by a dark film. Bright shiny surface obtained on Te terminated or B face.

3.3 Process of Chemical Etching

Defects in crystals were etched and etch pits are formed where these defects exist. The shape of the etch pits on different orientation of the sample was investigated using various etchants. The Four etching reagents, which have been used in this work were Nakagawa, Everson, Inoue's EAg2 and Bagai solutions. All etching processes were carried at room temperature. Nakagawa, Bagai and Everson solutions were used to reveal defects on {111} and {211} surface of samples while Modified Inoue EAg2 solution were used to reveal {110} surface in addition to {111} and {211} surfaces. Saucedo Etchant was used to reveal twins and twin boundaries, grain and grain boundaries and dislocations in multigrain CZT samples. SEM was used to image these etched samples. The range of the magnification extended from x100 to x50000. Electron Diffraction Spectroscopy (EDS) was performed to measure the change in the stoichiometry of the selected area on the etched surface. Specially, EDS line mapping analysis was performed on the etch pit resulting from chemical reactions.

3.3.1 Etching

Polished {111} and {211} CZT samples were etched using Nakagawa etchant, which consists of HF+H₂O₂+H₂O with a ratio of 3:2:2. Samples then cleaned carefully with alcohol to remove the black layer resulted from Nakagawa etching. In order to investigate whether etching time affects the size of etch pits, CZT sample was etched using Nakagawa etchant with different etching times (**Table 3**).

Table 3 Nakagawa etching of CZT samples with different time intervals

Sample Name	Etching Time	Comments
MT1_S4	1 min	
MT1_S5	2 min	
Commercial_W4	2 min	Air exposure (Oxidation)
Commercial_W5	2 min	Subsequent analysis
Commercial_W6	1, 3,5 & 8 min	Etch pit dimension
MT1_S3	1 min	Comparison of different etchants
MT2_S2	Up to 15 min	Etching rate analysis

Also, polished {111} and {211} samples were exposed to Everson solution, which consists of HF+HNO₃+Lactic acid with a ratio of 1:4:25. Samples was rinsed immediately and dried carefully after exposure of Everson etchant. In addition, three different samples were etched with different time intervals in order to prove that the dimension of the etch pit is increased (**Table 4**).

Table 4 Everson etching of CZT samples with different time intervals

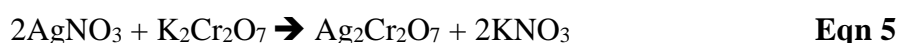
Sample Name	Etching Time	Comments
Commercial_W7	1 min	
Commercial_W8	2 min	
Commercial_W9	3 min	
MT1_S3	2 min	Comparison of different etchants
MT2_S1	Up to 20 min	Etching rate analysis

In addition, Bagai etchant which consists of HF+H₂O₂+H₂O with a volume ratio of 4:0.5:2 was used to analyze the distribution of dislocations in CZT sample. Moreover, the changes in the surface was examined using SEM analysis (**Table 5**).

Table 5 Bagai etching of CZT samples with different time intervals

Sample Name	Etching Time	Comments
Commercial_W11	4 min	
MT1_S3	4 min	Comparison of different etchants

Dislocations on {110}, {111} and {211} surfaces revealed using Inoue etchant and characterized by SEM in order to observe distribution of etch pits on these orientations. Inoue's E-solution consists of 20 ml H₂O + 10 ml HNO₃ + 4g K₂Cr₂O₇. Inoue's EAg2 solution contains 10 ml E-Solution and 10 mg AgNO₃. However, no pitting was observed on the surface of the CZT crystals. So {111}, {211}, and {110} CZT samples were etched with Modified EAg-2 solution, which contains 10 ml E-Solution and 30 mg AgNO₃ (**Table 6**). This etching procedure had higher silver concentration than Inoue EAg2 solution since silver ions are believed to be the main agent revealing dislocations. CZT samples were polished and then etched with modified EAg2 etchant for different time intervals, immediately were rinsed with deionized water and dried carefully.



During the etching procedures, Ag₂Cr₂O₇ precipitates were formed (**Eqn 5**) which are insoluble in water. In order to obtain a uniform etching, the solution was stirred continuously.

Table 6 Inoue etching of CZT samples with different time intervals

Sample Name	Etching Time	Comments
MT1_R1	1 min	Modified Inoue solution
MT1_S1	1 min	
MT1_S3	2 min	Comparison of different etchants
MT_W2	1 min	Observation of twin boundary; modified Inoue solution
MT2_S3	Up to 6 min	Inoue EAg2 etching rate – Te inclusion is observed
MT1_S2	Up to 6 min	Inoue EAg1 etching rate – Te inclusion is observed
MT1_S8	1 min	As cut
Commercial_W10	Up to 10 min	
MT2_W5_2	1 min	
MT4_M1	1 min	EPD analysis

Saucedo Etchant consists of H₂O (20 ml) + HNO₃ (15 ml) + HF (5 ml) + AgNO₃ (0.4 g). Samples were inspected by unaided eye and their surface morphology was investigated by SEM analysis (**Table 7**).

Table 7 Saucedo etching of CZT samples with different time intervals

Sample Name	Etching Time	Comments
MT1_M1	2 min	Observation of twins and twin boundaries
MT2_S4	30 sec	Formation of etch pits
MT2_W5_1	1 min	
MT1_S9	2 min	Geometry analysis of etch pits on twin and host grain

3.3.2 Etching Rate Study

For each combination of the etching parameters, etching rate on (111) & (211) planes was performed by determining the weight of removed CZT layer and measured thickness of the sample by contact thickness measurement gauge (**Table 8**). After etching, the shape and size of the triangular etch pits and the morphology of the pits were observed under optical microscope and SEM.

Table 8 Etch rate parameters; different etchants on {111} & {211} planes

Etchant	Etched plane	Thickness measurement
Inoue EAg2 Nakagawa Everson	{111} {211}	Calculated thickness Measured thickness

3.3.3 Oxidation Study

Change in the CZT surface composition and surface oxidation after Nakagawa etching was studied by XPS measurements. The surface composition of single-crystal CZT samples after exposure to 2 min Nakagawa chemical etching ($\text{HF} + \text{H}_2\text{O}_2 + \text{H}_2\text{O}$ with a ratio of 3:2:2) was employed. During the etching, hydrogen peroxide (H_2O_2) oxidized the surface of CZT samples and produced a thin TeO_2 layer that is soluble in the solution. Commercial_W4 etched and left in air at room temperature for oxidation. Both Commercial_W4 and freshly etched Commercial_W5 samples were examined using XPS measurements. These two samples displayed different surface chemistry. Nakagawa treated CZT samples were found to result in a graded Te-rich surface layer.

3.4 Transmission Electron Microscopy Analysis

TEM was used to characterize the structure of the grown CZT crystals down to the nanoscale with the focus on the origin of the defects. MT_M1 (multi-grain) sample was prepared by Focused Ion Beam (FIB), which allows micro machining to ‘cut out’ a selected area of a CZT bulk material for TEM analysis. FEI Nova 600i Nanolab Focused Ion Beam was used for thinning the sample.

In the FIB technique, Ga ion gun was used for thinning the sample (**Figure 10a&b**). Using the lift-out technique, the electron transparent thin membrane was pulled from the sample, analyzed directly by TEM (**Figure 10c**).

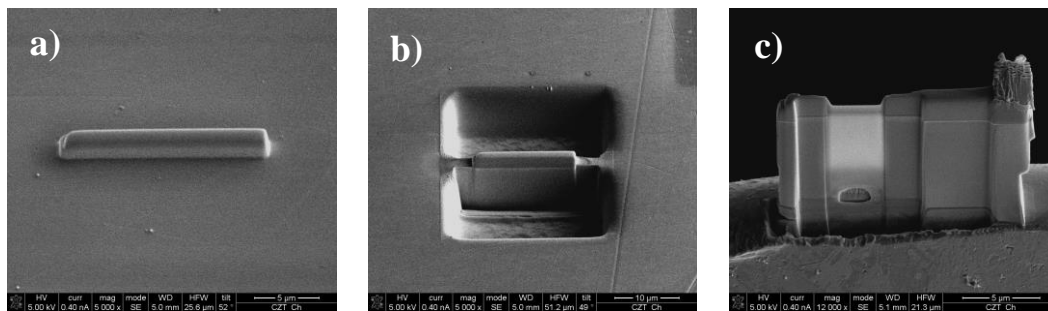


Figure 10 FIB technique **a)** Thinning the sample **b)** Both side of the sample removed by using Ga ions **c)** The electron transparent thin membrane was pulled from the bulk specimen using the lift-out technique.

JEOL JEM-2100F TEM with Field Emission Gun (FEG) was used and electron-transparent region was investigated. High-resolution electron microscope (HREM) is capable of monitoring structures at nanoscale and employed to observe line and point defects. Images of the CdZnTe matrix of selected areas were investigated and traced various defects distributed randomly.

CHAPTER 4

RESULT & DISCUSSION

4.1 Mechanical polishing

Ingots grown in our laboratories and commercial CZT substrates exposed to surface processes including cutting, lapping and polishing. Lapping and polishing processes was applied on CZT samples to obtain smooth and defect-free surfaces. Through successive lapping and polishing processes, surface root-mean-square (rms) roughness values of each process were obtained using AFM measurement. Lapping and polishing processes applied using alumina abrasives of 9, 3 and 0.3 μm in a slurry. Lapping processes were applied in successive steps to obtain a better surface roughness. The surface defects were removed after mechanical lapping and polishing. Since CZT crystal is a soft and brittle material, the alumina abrasive created scratches on the surfaces.

Three different lapping procedures were carried out in order to obtain the best surface roughness result. The surface morphology was investigated in accordance with different polishing procedures. The results were obtained using 9, 3 and 0.3 μm alumina powder shown in **Figure 11(a-c)**. AFM results as shown in **Figure 11a**, the surface of MT1_S1 has many scratches and the Rms roughness of the surface is ~ 300 nm in the sample polished with 9 μm abrasive powder. When 3 μm alumina powder was applied, there was a considerable decrease in the roughness and the surface becomes smoother. The Rms surface roughness obtained from 3 μm alumina lapping was ~ 120 nm as shown in **Figure 11b**. However, the best result was obtained from two-step lapping process; at first, 9 μm alumina powder lapping and then 3 μm alumina powder lapping processes shown in **Figure 11c**. In this case, the Rms surface roughness reduced to ~ 100 nm. Non-uniform areas were observed when the surface

was mechanically lapped. As might be expected, it was observed that the surface roughness decreases as the dimension of the alumina powder decreases.

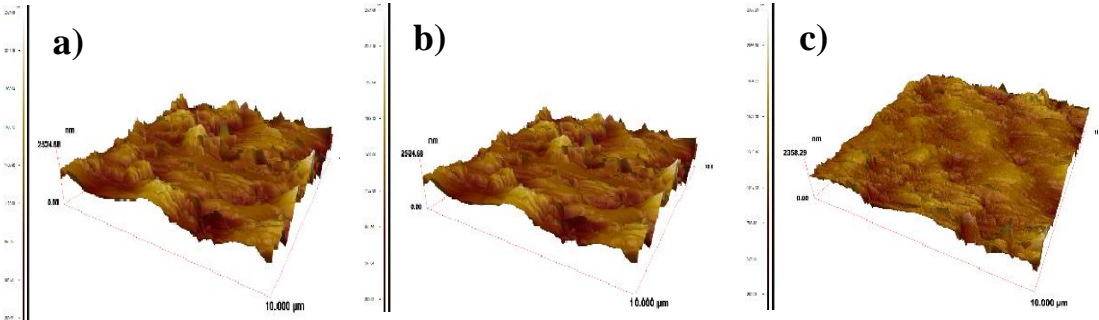


Figure 11 AFM images of MT1_S1 sample after mechanical lapping process. **a)** 9 μm alumina powder lapping, the Rms surface roughness is ~300 nm. **b)** 3 μm alumina powder polishing, the Rms surface roughness is ~120 nm. **c)** 3 μm alumina powder lapping after 9 μm initial lapping, the Rms surface roughness is ~100 nm.

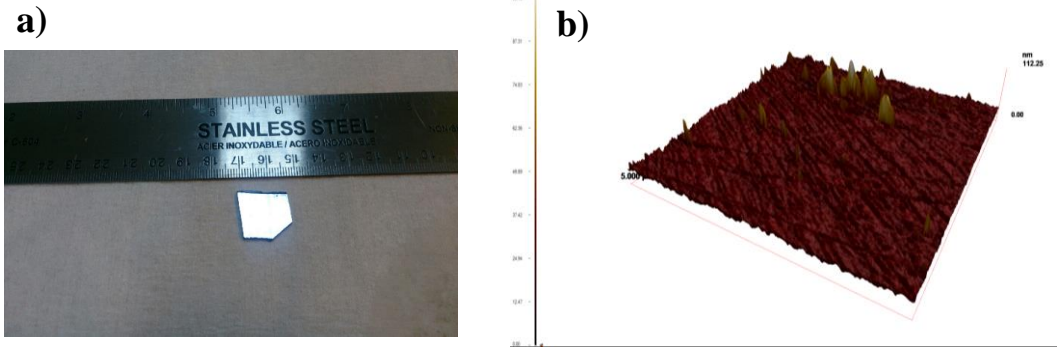


Figure 12 Final polishing procedure of MT1_S1 sample **a)** mirror-like surface of MT1_S1 after lapping and polishing process. **b)** AFM image of polished MT_S1, the Rms surface roughness is ~1.0 to 2.0 nm.

Best result was obtained using MT1_S1 sample with two step lapping processes (3 μm alumina powder lapping after 9 μm alumina powder lapping) and 0.3 μm alumina powder polishing process as can be seen in **Figure 12**. Mirror-like polished surface with an Rms surface roughness of 3 nm surface were achieved with this recipe.

4.2 Bromine Methanol Chemical Etching

After polishing process, samples were chemically etched to the remove damage introduced during cutting, lapping and polishing procedures. It was observed that although B-M etching removed the damaged layer on the surface; whereas, it produced Te rich surface and increased the roughness of the surface. The surface of the MT1_S1 etched with 1 ml Br_2 in 100 ml methanol (MeOH) for about 10 seconds followed by a final MeOH rinse. AFM images in **Figure 13** shows that B-M etching results in a higher surface roughness compared to roughness value obtained after mechanical polishing.

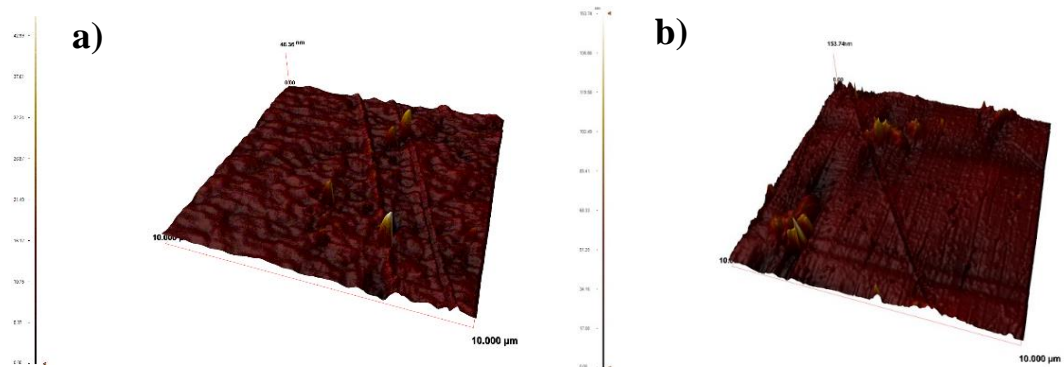


Figure 13 Chemical etching with B-M solution after polishing process of MT1_S1 sample; **a)** 3 μm alumina powder lapping after 9 μm initial lapping; the Rms surface roughness is 1.0 to 2.0 nm. **b)** 10 sec 1% B-M etching; the Rms surface roughness is 3.0 to 6.0 nm.

4.3 Etching Studies

In this part of the thesis, the aim of the etching studies was to reveal etch pits after different etching processes with different orientations. Optimization of the etching process and achievement of the best methodology to understand the defect structures on the CZT crystals that grown in our laboratories and on the commercial CZT samples were investigated.

4.3.1 Inoue Etching

Etch pits on {110} MT1_R1 surface was examined by Modified Inoue EAg2 etchants for 1 minute. Sample then are characterized by SEM in order to observe distribution and density of dislocations. As seen in **Figure 14**, most of the etch pits appeared to be on a straight line, which is believed to be a dislocation line and it is observed throughout the surface. Etch pits on {110} face appeared to be an isosceles triangle (**Figure 14c**). The linear etch pits corresponded to dislocations associated with dislocation lines; while the individual triangular etch pits corresponded to individual dislocations formed in the MT1_R1 sample.

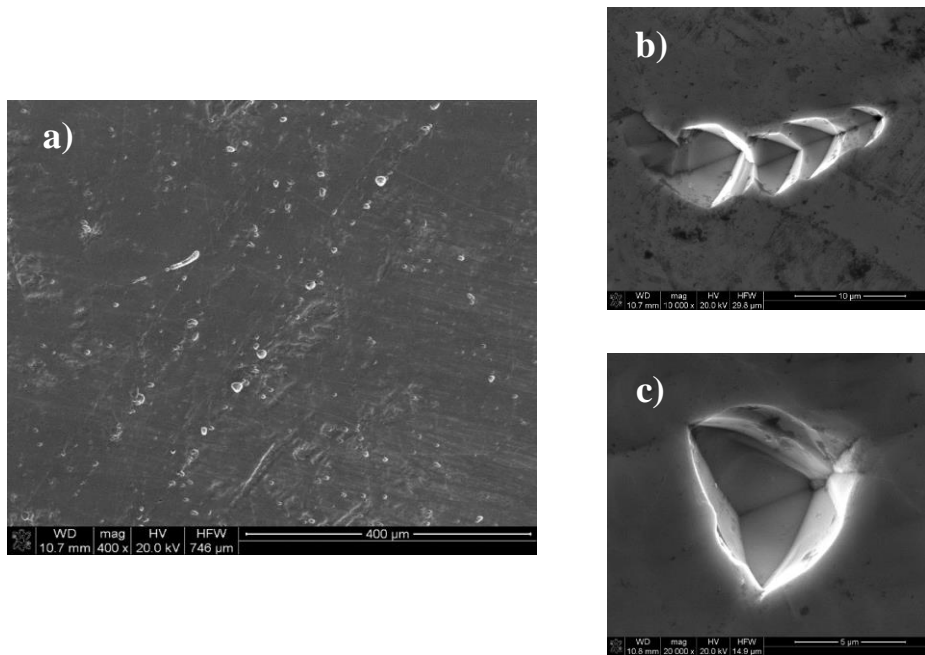


Figure 14 SEM images of 1 min modified EAg-2 etched {110} MT1_R1 sample **a)** Etch pit distribution on a straight line throughout the surface. **b)** Etch pits formed along the dislocation line. **c)** Triangular etch pits

Figure 15a shows the XRD pattern of MT1_S3 sample. The diffraction pattern indicates that MT1_S3 sample has a {111} crystal orientation. Modified EAg2 etchant was applied to the B face of the MT1_S3 sample for 2 minutes and triangular pits appeared to be in pyramidal shape that was formed all over the surface as shown in **Figure 15b**. Etch pit density was calculated to be as $\sim 9.5 \times 10^4 \text{ cm}^{-2}$ on {111}B face. The angle between facet of the triangular etch pit is about 70° which is the inter-planar angle between (111) and $(\bar{1}\bar{1}1)$ planes. Structure of the etch pits formed by chemical etching consist of four {111} planes and the facets are almost in the same size.

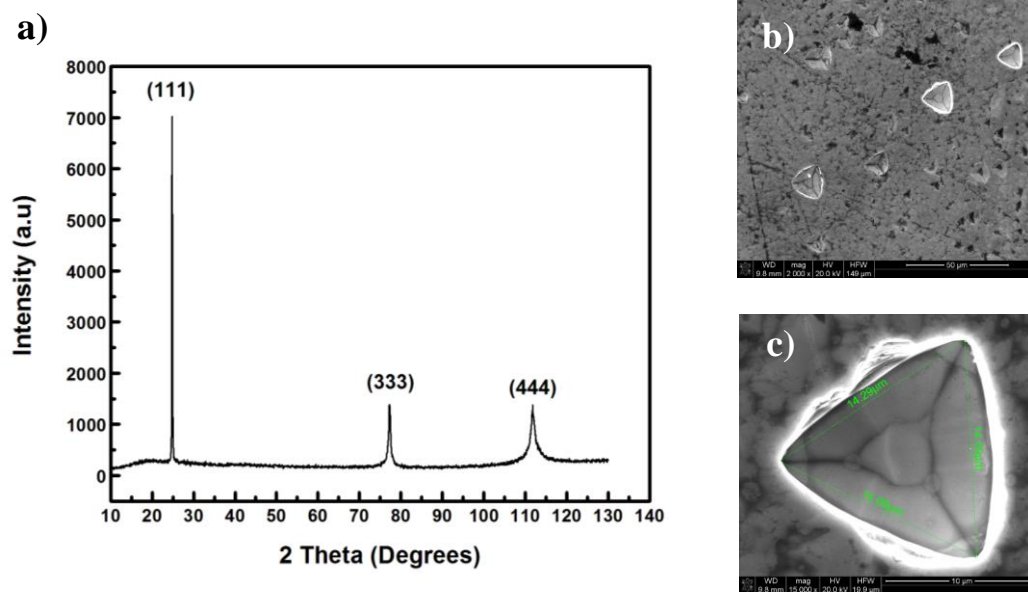


Figure 15 XRD pattern and SEM images of 2 min modified EAg-2 etched MT1_S3 sample. **a)** XRD pattern of MT1_S3 sample. **b)** Etch pits distribution on the surface of {111} MT1_S3 sample. **c)** Equilateral triangular pyramidal etch pit on B face.

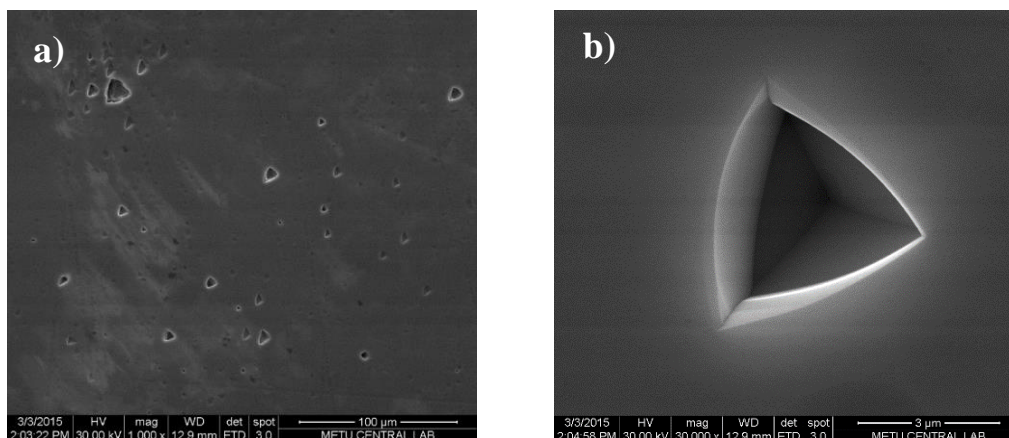


Figure 16 SEM images of 1 min Modified EAg2 etched {211} Commercial_W10 sample. **a)** Etch pits distribution on the B face of the sample. **b)** Triangular pyramidal etch pit with a slight deviation.

Etch pits on B face of {211} Commercial_W10 sample was examined by modified EAg-2 etching for 1 minutes and characterized by SEM in order to observe distribution and density of dislocations shown in **Figure 16**. EPD calculated to be $\sim 7.0 \times 10^4 \text{ cm}^{-2}$. However, the EPD varied throughout the surface of the etched sample.

{211} MT_W2 sample was etched with Modified EAg-2 etchant for 1 min in order to observe grain and grain boundaries, twins and twin boundaries and dislocations. **Figure 17** shows the etch pit distribution and the shape of the pits. **Figure 18** shows that Modified EAg-2 etchant revealed twin boundaries by the change in the polarity of the etch pits across the boundary. The orientations of etch pits in both sides of the boundary had mirror symmetry on some part of the crystal. Triangular etch pits were observed on the surface while the rounded shape of etch pits were seen at the boundary line.

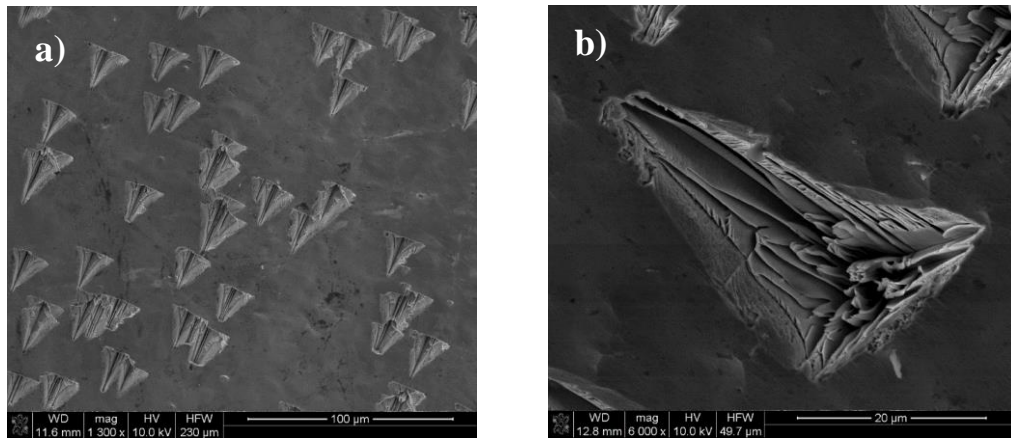


Figure 17 SEM images of 1 min modified EAg2 etched {211} MT_W2 sample. **a)** Distribution of etch pits on the B face of the sample. **b)** Triangular etch pit.

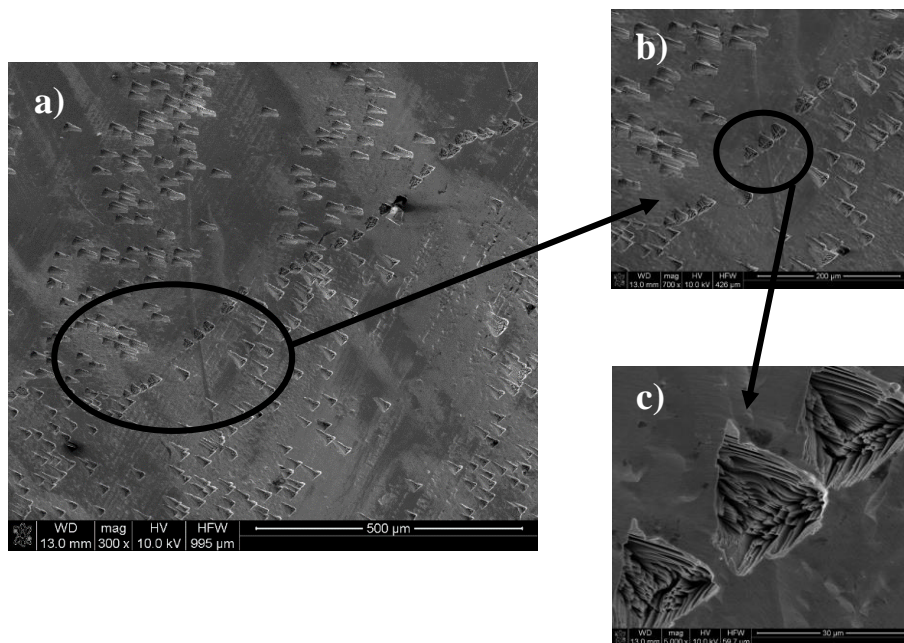


Figure 18 SEM images of twin boundary revealed on MT_W2 sample. **a)** and **b)** The change in the orientation of triangular etch pits on the boundary. **c)** Rounded etch pits at the boundary line.

As-cut $\{111\}$ MT1_S8 sample was etched with 1 min modified EAg2 etchant in order to reveal mechanically induced dislocations on the surface of the sample. No polishing process was applied to this sample. The linear etch pits corresponded to dislocations associated with mechanical stresses while the individual triangular etch pits correspond to the individual dislocation formed in the CZT crystal. **Figure 19** shows the arrangement of etch pits on a straight line due to the low angle grain boundary existing in crystal structure resulting from cutting process.

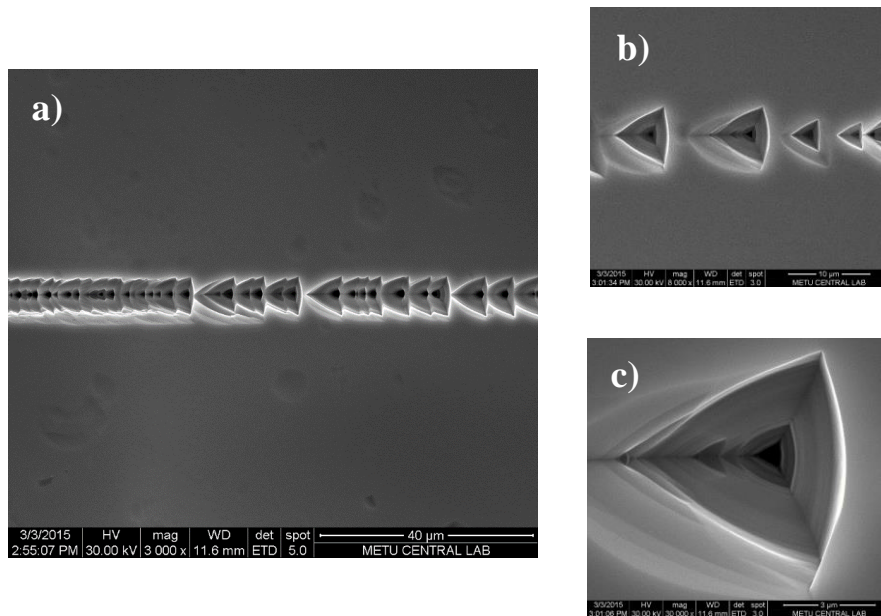


Figure 19 SEM images of 1 min Modified EAg2 etched as-cut $\{111\}$ MT1_S8 sample. **a)** and **b)** Etch pits on a straight line. **c)** Triangular pyramidal etch pit.

Additionally, the change of etch pit density along vertical axis within central slab of MT4_M1 (multi-grain) sample was examined as shown in **Figure 20**. This was done to understand the dependence on the location on EPD measurements along the growth direction of the MT4 ingot. Modified Inoue EAg-2 solution was applied for 1 min and investigated using SEM. EPD measurements were examined by choosing specific areas of central slab of MT4 ingot along a single grain as shown in **Figure 20a&b**. Each image shown in **Figure 21(a-f)** was taken from areas along the vertical axis within central slice of MT4 from the bottom to heel. Etch pit was usually considered as to be related with dislocations.

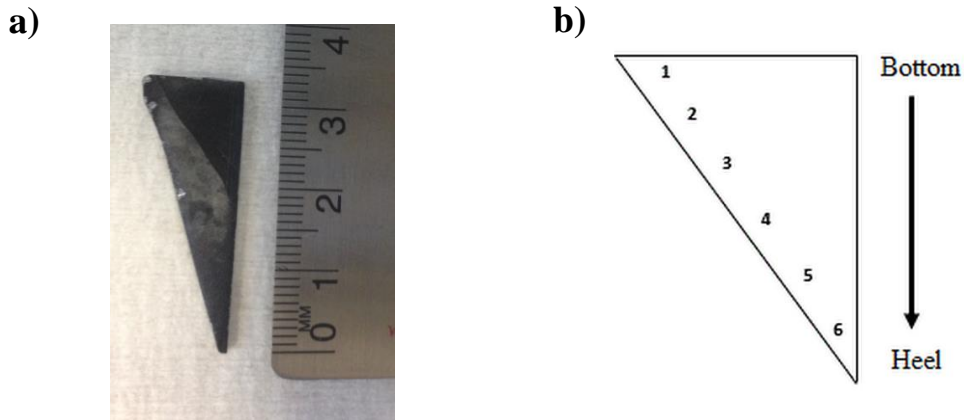


Figure 20 a) Image of central slab of MT4_M1 sample. b) Numbering on the sample gives the location of where EPD and EDS measurements were taken.

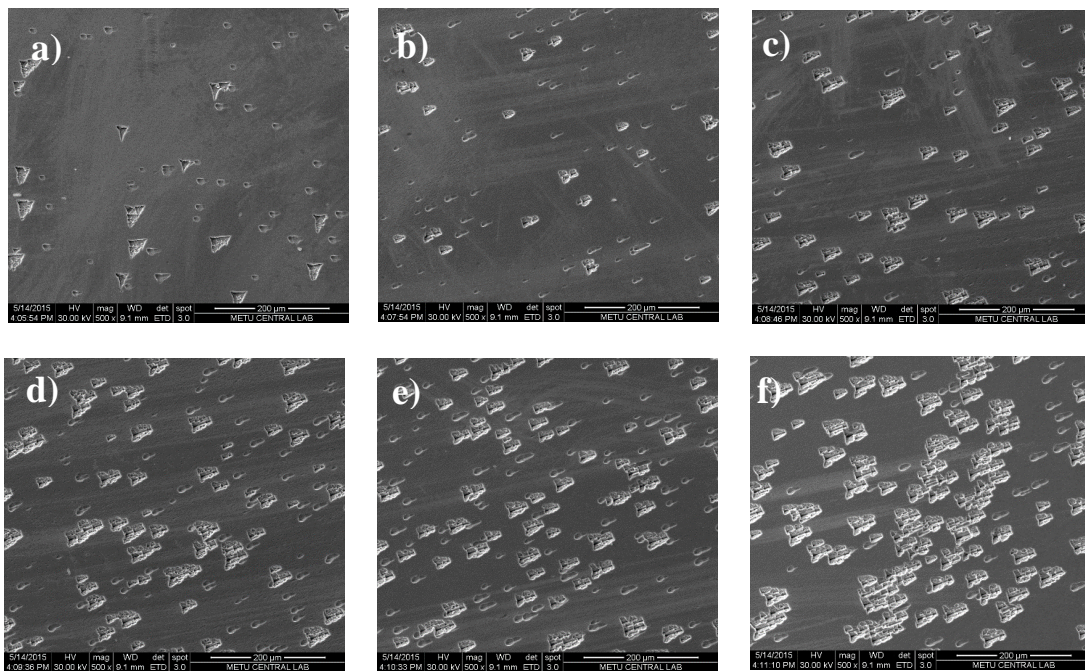


Figure 21 SEM images of MT4_M1 sample. a-f) Etch Pit Density (EPD) varying with locations on a single grain from bottom to heel.

As shown in **Figure 22**, the concentration of etch pits varied significantly from bottom to the heel of the sample. It was found that while the bottom of the ingot had fewer dislocations and lower EPD, the heel had more dislocations and higher EPD. The EPD of the bottom part of the sample was nearly $2 \times 10^4 \text{ cm}^{-2}$, whereas the EPD of the heel part was calculated to be nearly $2 \times 10^5 \text{ cm}^{-2}$.

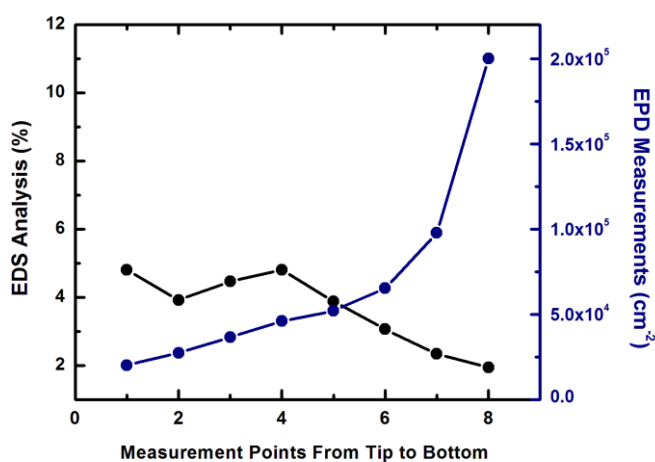


Figure 22 Comparison of EDS Analysis and EPD Measurements of MT4_M1 sample with respect to measurement points from bottom to heel of the sample.

The change in the EPD might be related with the variation of the stoichiometry due to the variation in the Zn concentration throughout the sample during the growth process as shown in the **Figure 22**. When Zn concentration of the slab was considered, sample had higher Zn concentration near the tip and decreasing slowly at the heel because of segregation. However, it is not certain that the segregation of Zn caused varying EPD of the crystal since the heel of the ingot was always Te rich and had non-stoichiometric

structure. Samples could be obtained from the central-tip of the ingot with minimum mechanical damage for lower EPD corresponding to fewer dislocations.

4.3.2 Nakagawa Etching

Nakagawa etchant was applied on polished CZT samples and the results were investigated using the SEM technique. Two {111} grown samples and {211} commercial substrates were etched with Nakagawa etchant for about 1 and 2 minutes.

{111} MT1_S4 sample was etched by Nakagawa etching for 1 min as shown in **Figure 23a**, the EPD was calculated to be roughly $\sim 2.2 \times 10^5 \text{ cm}^{-2}$. Additionally, the surface of the samples etched vigorously. The EPD found using modified Inoue solution was one order lower than that found using Nakagawa solution. Nakagawa etching appeared to affect both Te and Cd terminated surfaces of the sample and the shape of the etch pits changes with polarity. According to literature, Nakagawa solution reveals both α and β dislocations in CZT crystals. The α and β dislocations have equilateral triangular shapes with different polarity and the flat bottom etch pits have the same size [58]. **Figure 23b** shows the arrangement of etch pits in a linear pattern, which was possibly due to the dislocation lines (sub-grain boundaries) existing in crystal structure.

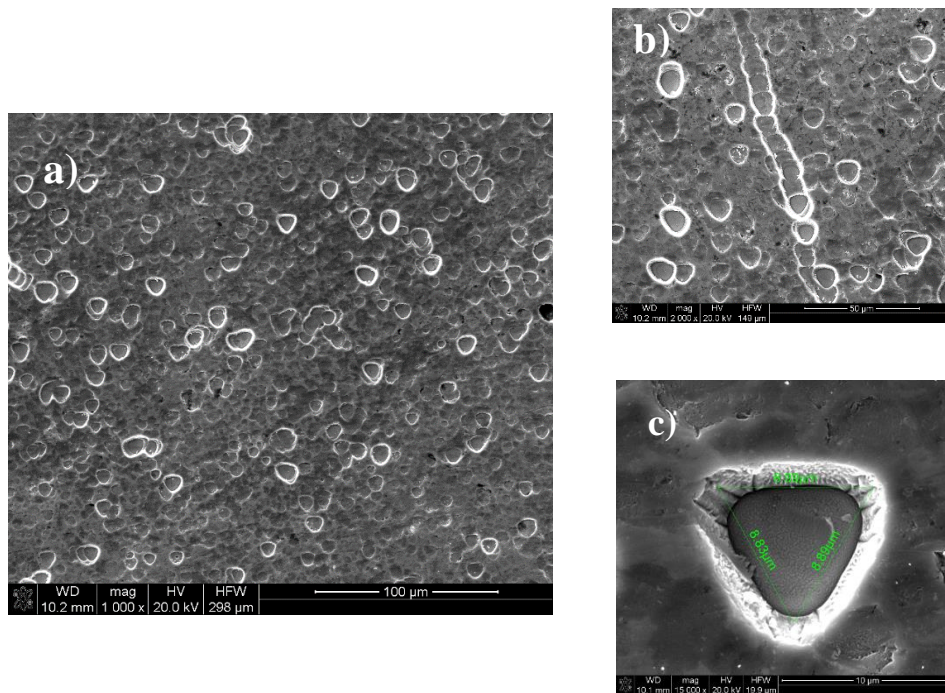


Figure 23 SEM images of 1 min Nakagawa etched {111} MT1_S4 sample **a)** Etch pit distribution on B face of the sample. **b)** Etch pits along dislocation line. **c)** Equilateral triangular flat bottom etch pit.

A face of {111} MT1_S5 sample was also examined after Nakagawa etching for 2 minutes and the EPD was calculated as $\sim 1.8 \times 10^5 \text{ cm}^{-2}$ as seen in **Figure 24**. Therefore, it was observed that the EPD did not change with increasing etching time in this case. Rounded etch pits observed and edge of the pits had the same size as shown in **Figure 24b**. Dislocation lines became visible on the surface after the etching process. Etching for 2 minutes formed etch pits at least twice as big as the etch pits formed by 1 minute etching. **Figure 24c** shows the crack appeared on the surface of the sample after etching process. These cracks might form due to the thermal or mechanical stress and initiated after exposure of surface to the solution.

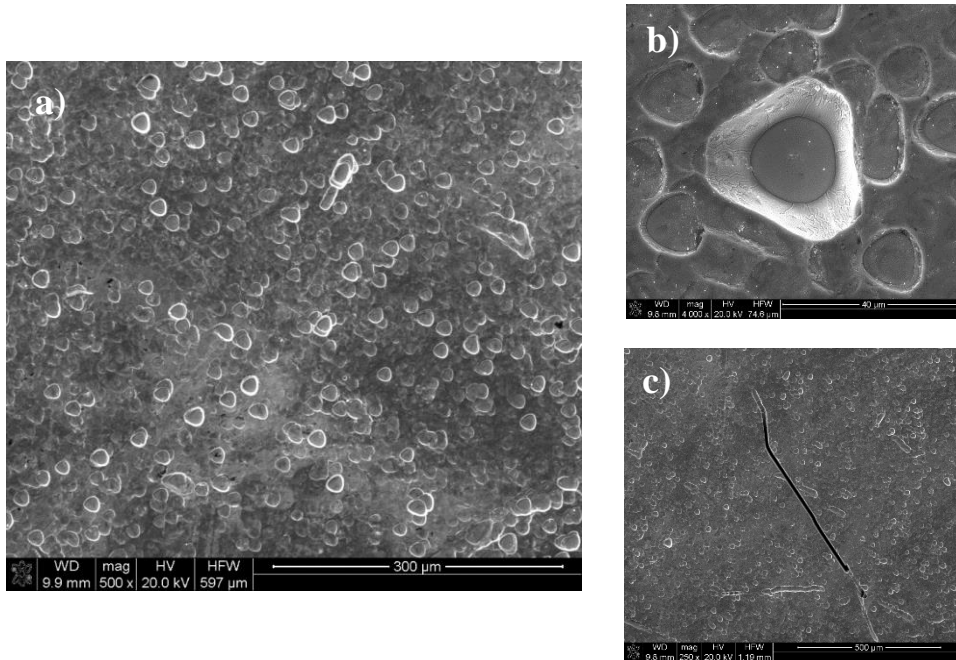


Figure 24 SEM images of 2 min Nakagawa etched {111} MT1_S5 sample **a)** Etch pit distribution on A face of the sample. **b)** Flat bottom rounded etch pits on the A face. **c)** Crack on the surface.

It was observed that the EPD of the {111} MT1_S3 sample was nearly the same on both faces, which was $\sim 2.3 \times 10^5 \text{ cm}^{-2}$. Rounded etch pits formed on A face of the sample while triangular etch pits are observed on B face of the same sample as shown in **Figure 25**.

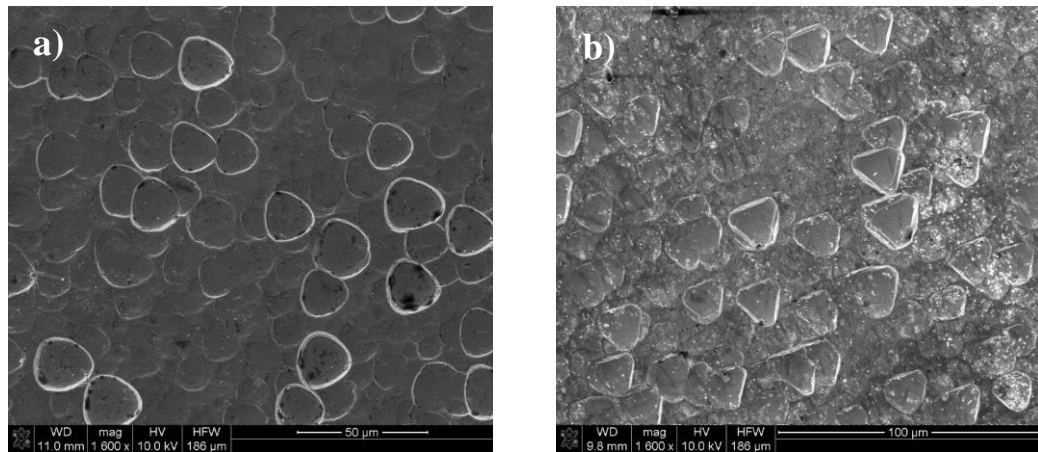


Figure 25 SEM images of 1 min Nakagawa etched {111} MT1_S3 sample: EPD calculated to be same on A&B faces of the sample $\sim 2.3 \times 10^5 \text{ cm}^{-2}$. **a)** The rounded etch pit on the A face. **b)** The triangular etch pits on the B face.

Additionally, {211} Commercial_W4 sample was etched in order to reveal defect structure in different orientations. 2 minutes Nakagawa etching was applied and EPD was found to be approximately $1.2 \times 10^5 \text{ cm}^{-2}$. This result clearly revealed that the CZT samples grown under this study are compatible with the commercial CZT substrates in terms of the crystal quality. Scratches appeared throughout the surface of the etched sample was probably due to the defects formed by mechanical polishing (**Figure 26**). Again, rounded etch pits were observed on A face of Commercial_W4 substrate and etch pits had the same size.

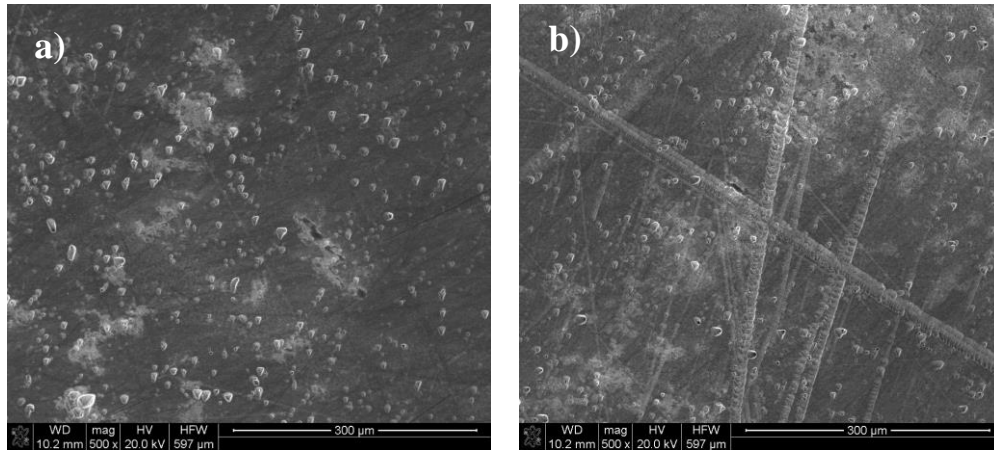


Figure 26 SEM images of 2 min Nakagawa etched {211} Commercial_W4 sample
a) Rounded etch pits on A face of the sample. b) The scratches on the surface.

The size of the etch pits was also investigated as a function of etching time. For this purpose, {211} Commercial_W6 sample was used and various etch conditions were applied. It was observed that extended defects dissolve continuously in the solution and thus the length and depth of the pits had a tendency to increase linearly with time. Etching time selected to be 1, 3, 5 and 8 min in order to reveal the change in the size of the etch pits as shown in **Figure 27**. In **Figure 28** shows the size of the etch pits as a function of etching time. It was found that there was a linear relationship between the size of the etch pits and etching time. The EPD of the sample was not changing with time; but, as the time was increased more than 5 minutes, the etch pits were formed within each other and the determination of the etch pit density became difficult. When an extremely long etching time of 30 min was applied; the surface of the sample was etched rigorously and pits were formed within each other (**Figure 29**).

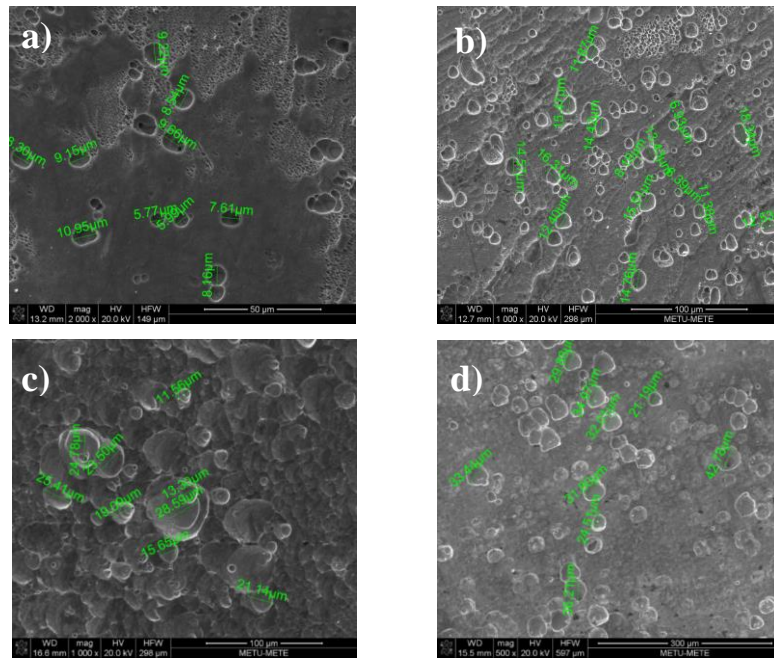


Figure 27 SEM images of Nakagawa etched Commercial_W6 sample by varying etching time. **a)** 1 min etching **b)** 3 min etching **c)** 5 min etching **d)** 8 min etching.

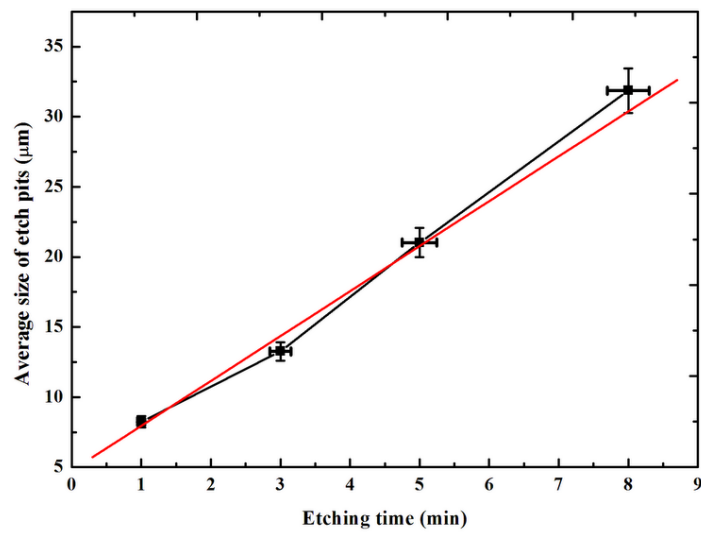


Figure 28 The average size of the etch pits exposed to varying etching time; length of the etch pits increased with time. (Lines are for visual aid)

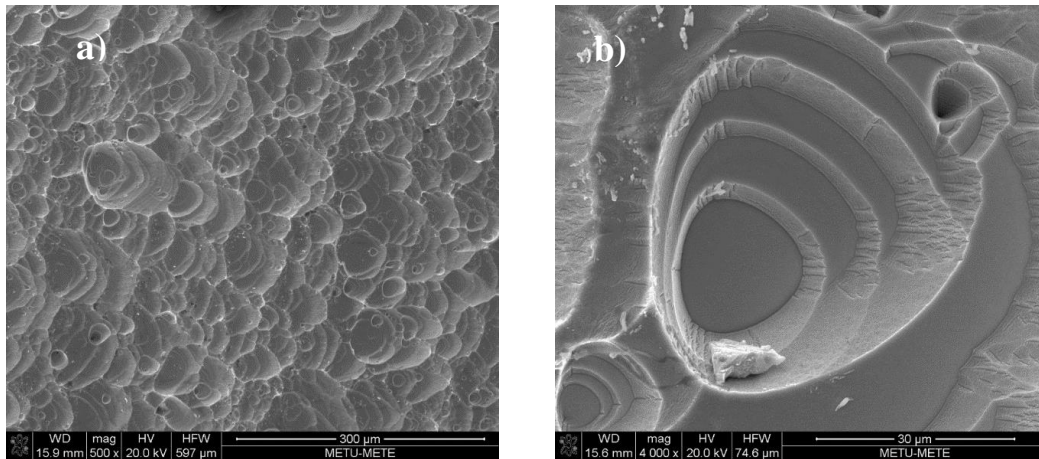


Figure 29 SEM images of Commercial_W6 after 30 min Nakagawa etching. **a)** Surface of the sample etched vigorously. **b)** Etch pits formed within each other.

4.3.3 Everson Etching

In this section, the etch pits formed on $\{211\}$ and $\{111\}$ CZT crystals by Everson etchant were presented. The surface morphologies of 1 min etched Commercial_W7 surface shown in the SEM images grounded in **Figure 30**. Both bar like and triangular etch pits were observed on $\{211\}$ CZT samples. According to Jianrong (2002), Different etch pit structure is a result of different type of dislocations that exist in the crystal structure. Additionally, α dislocation was observed as an obtuse triangle etch pit while β dislocation was observed as an acute triangle etch pit [60]. **Figure 30** shows α and β dislocations with different polarity and the EPD value was $\sim 2.5 \times 10^5 \text{ cm}^{-2}$.

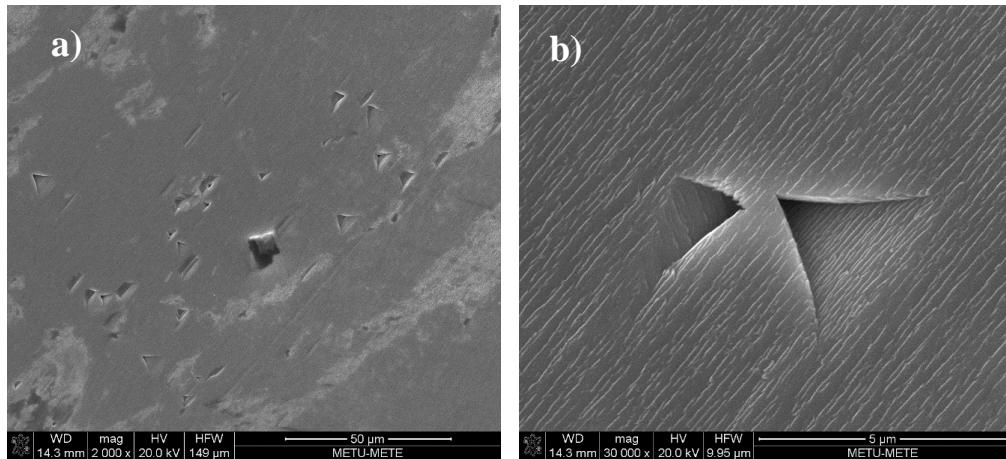


Figure 30 SEM images of 1 min Everson etched {211} Commercial_W7 sample; **a)** Bar-like and triangular etch pits on the B face. **b)** The α and β etch pits.

In addition, 2 minutes Everson etching was applied on {211} Commercial_W8 and the change in the surface morphology studied. **Figure 31a** shows formation of bar like and triangle etch pits. The calculated EPD was about $1,4 \times 10^5 \text{ cm}^{-2}$; but, it was not uniform throughout the surface of the sample. **Figure 31b** shows etch pits formed on a straight line indicating dislocation line or sub-grain boundaries existing in the CZT crystal.

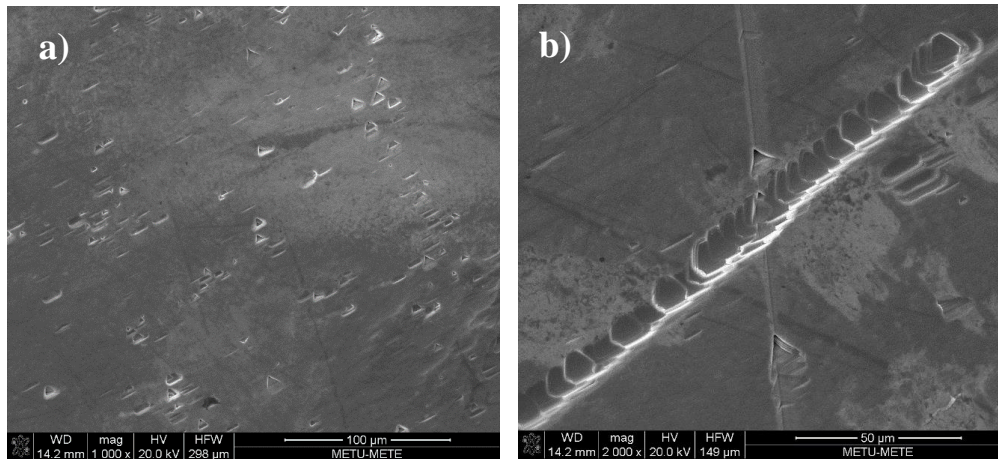


Figure 31 SEM images of 2 min Everson etched {211} Commercial_W8 sample; **a)** Distribution of etch pits on the B face. **b)** Formation of the etch pits on a straight line.

Everson etchant was also applied on {111} MT1_S3 sample in order to find out the behavior of EPD and etch pit formations. After re-polishing the sample, MT1_S3 sample was etched with 2 min Everson etchant. The surface morphology of the sample was investigated in order to observe the distribution of dislocations. The EPD was calculated to be $\sim 1.2 \times 10^7 \text{ cm}^{-2}$. EPD was relatively high since nanoscale pitting was observed and pits are formed within each other as shown in **Figure 32**. Additionally, the surface of the sample was etched vigorously.

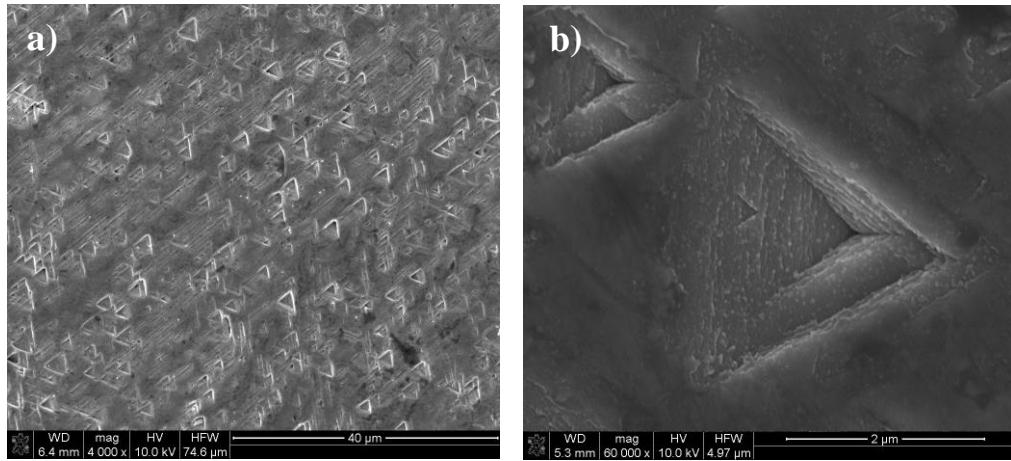


Figure 32 SEM images of Everson etched MT1_S3 sample, EPD: $\sim 1.2 \times 10^7 \text{ cm}^{-2}$; **a)** Distribution of etch pits on the B face. **b)** Triangular etch pit within each other.

4.3.4 Bagai Etching

Bagai uses the same chemicals with Nakagawa solution; but, oxidant concentration is different. In this case, the etching time was 4 minutes. However, different etch pit formations was observed on the surface of $\{211\}$ and $\{111\}$ CZT samples. This solution etched dislocations on the surface by producing flat bottom triangular shape pits on the Commercial_W11 sample (**Figure 33**). Moreover, the EPD was calculated as $\sim 4.3 \times 10^5 \text{ cm}^{-2}$. Bagai etching believed to etch α and β dislocations; but, only one type of etch pits was observed.

Rounded etch pits were observed on the surface of the $\{111\}$ MT1_S3 sample as shown in **Figure 34**. The surface of the sample was aggressively etched and the EPD was around $\sim 1.3 \times 10^6 \text{ cm}^{-2}$.

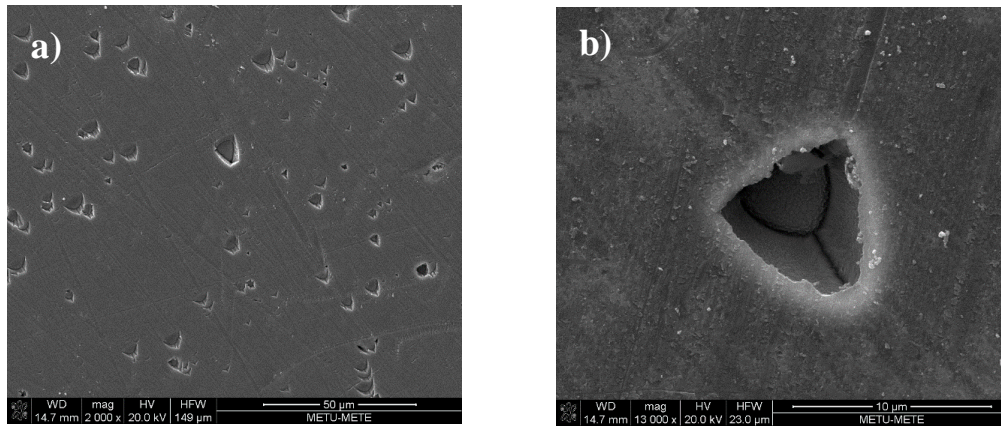


Figure 33 SEM images of 4 min Bagai etched {211} Commercial_W11 sample; EPD $\sim 4.3 \times 10^5 \text{ cm}^{-2}$; **a)** Distribution of etch pits on the surface of the sample. **b)** Triangular etch pit.

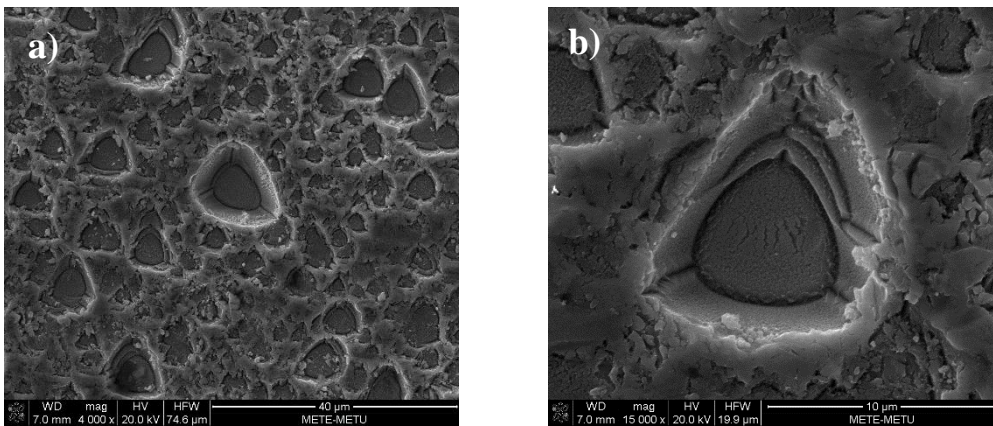


Figure 34 SEM images of 4 min Bagai etched {111} MT1_S3 sample; EPD: $\sim 1.3 \times 10^6 \text{ cm}^{-2}$ **a)** Etch pits distribution on the surface. **b)** Rounded etch pit.

4.3.5 Saucedo Etching

Etching time and reactions affected the morphology of etch pit and the etching rates along different crystal orientation affect the formation of the etch pits on CZT crystals. Firstly, etchant attacks stress field initiated by a dislocation which causes splitting to form etch pits on the surface (**Figure 35a**). Next, those etch pits start broadening due to the change in the etch rate along different orientations (**Figure 35b**). Finally, pits expand into its area so that those pits form in the shape of triangle (**Figure 35c**). Additionally, the size of the etch pits might differ during the etching process since etching continuously reveal new fields and these new stress fields etched by etchants; as a result, a time lag seen in the formation of etch pits.

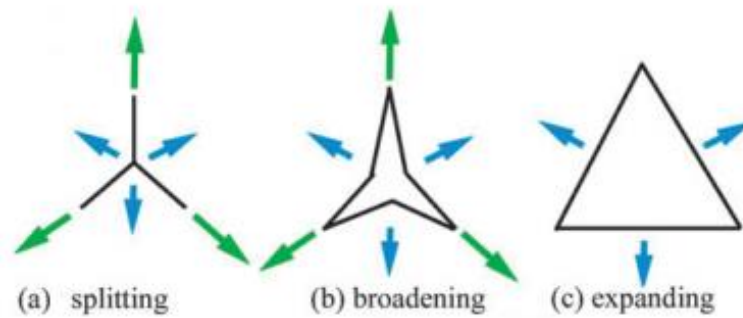


Figure 35 Schematic of formation of etch pits after exposure of etchants [31].

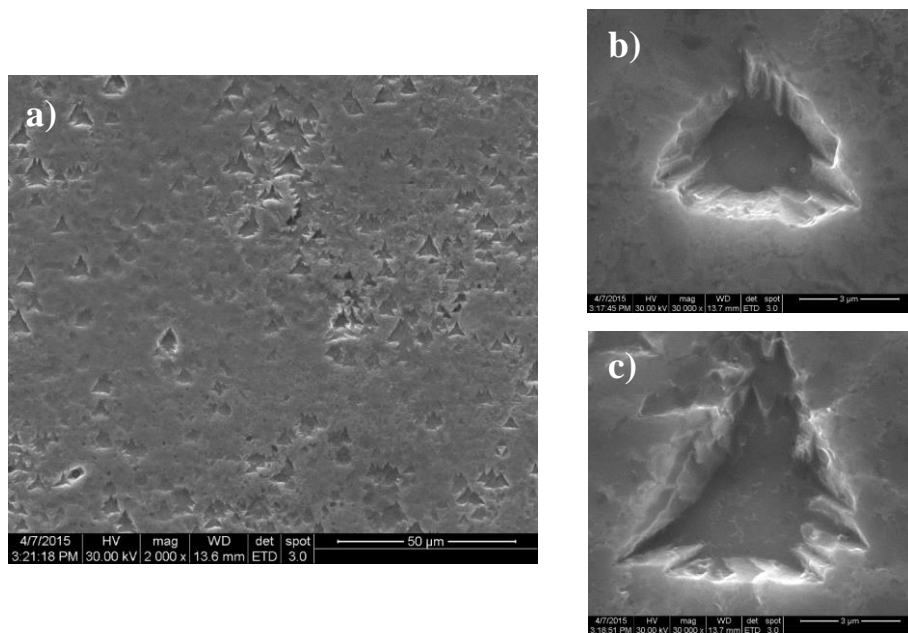


Figure 36 SEM images of 30 sec. Saucedo etched $\{111\}$ MT2_S4 sample; EPD: $9.6 \times 10^5 \text{ cm}^{-2}$ **a)** Etch pits distribution on the surface. **b)** and **c)** Broadening etch pit with different size.

Non-uniform etch pits having different shape and size were observed for 30 sec etched sample. SEM images of Saucedo etching of MT2_S4 sample shown in **Figure 36**. Therefore, etching time was found to be important in the formation of etch pits and it was observed that 30 sec etching is not sufficient for revealing etch pits.

Figure 37 shows SEM images of Saucedo etching of $\{111\}$ B face of host grain with $\{111\}$ A face of twin of MT1_S9 sample and this etching was used to reveal dislocations, twins and twin boundaries. The pits also showed that the twin and matrix are related and have the same shape with different orientations. Flat bottomed triangular etch pits changed their polarity upon crossing the boundary. It was observed that revealed twins showed high crystallographic symmetry with their host matrix and have special orientations. CZT crystal with $\{111\}$ B plane contains a twin whose

polarity is changed by 180° with respect to the host grain. Twin and twin boundaries were clearly seen from the **Figure 37a**. Any pits were observed at the twin boundary where it intersected the surface. EPD values of both host grain ($\sim 3.9 \times 10^4 \text{ cm}^{-2}$) and twin ($\sim 3.02 \times 10^4 \text{ cm}^{-2}$) calculated to be almost the same.

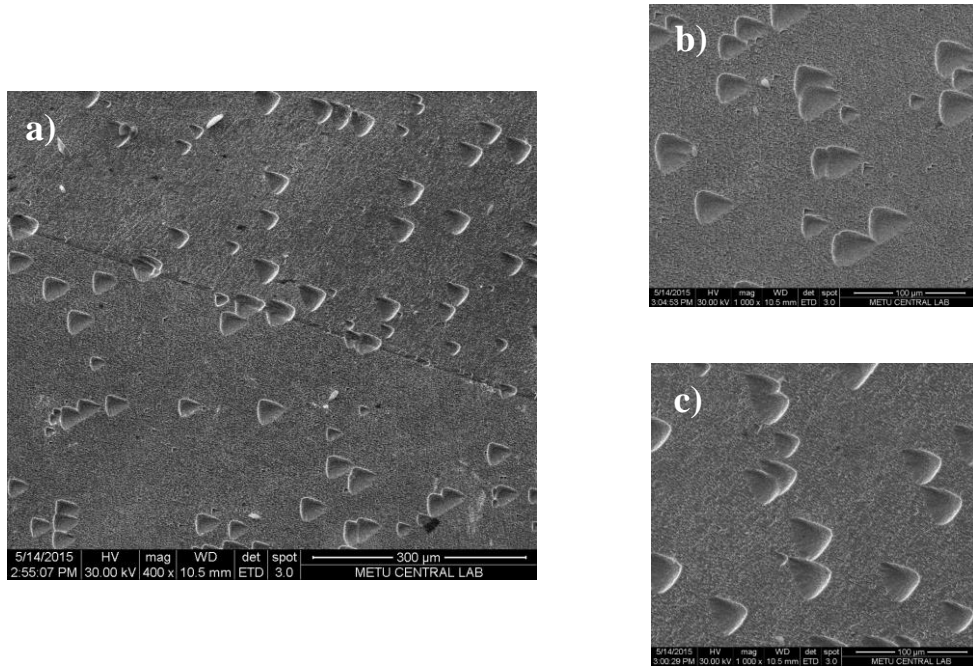


Figure 37 SEM images of Saucedo etched $\{111\}$ MT1_S9 sample; **a)** Twin boundary on the surface of $\{111\}$ B host grain with $\{111\}$ A twin. **b)** Etch pits on the grain with EPD: $3.9 \times 10^4 \text{ cm}^{-2}$ **c)** Etch pit on the twin with EPD: $3.02 \times 10^4 \text{ cm}^{-2}$.

Saucedo etching was investigated on $\{211\}$ MT2_W5_1 sample in order to reveal the shape of the etch pits and to compare EPD results of Inoue and Saucedo etching. On the other hand, Saucedo etching could be used to reveal defects and obtain density of dislocations. **Figure 38** shows SEM images of 1 min Saucedo etched MT2_W5_1 sample, which had an EPD of roughly $1.2 \times 10^5 \text{ cm}^{-2}$. Similarly, $\{211\}$ MT2_W5_2

sample etched by 1 min Inoue etching and EPD obtained to be roughly $4.5 \times 10^5 \text{ cm}^{-2}$. As a result, both EPD obtained from Saucedo and Inoue etchants were nearly the same. Thus, Saucedo etching can be used to calculate EPD of the sample. The shape of the triangular etch pits formed by Saucedo etching were more evident.

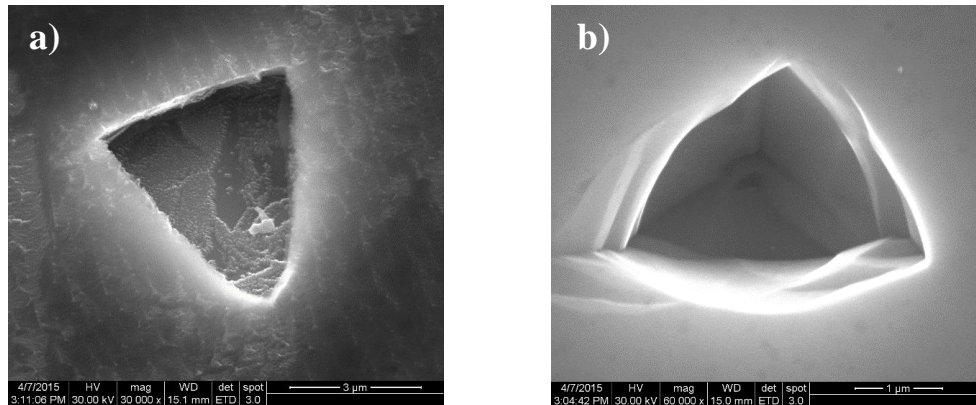


Figure 38 SEM images of the comparison of Saucedo and Inoue etching **a)** 1 min Saucedo etched MT2_W5_1 sample; EPD: $1.2 \times 10^5 \text{ cm}^{-2}$ **b)** 1 min Inoue EAg2 etched MT2_W5_2 sample; EPD: $4.5 \times 10^5 \text{ cm}^{-2}$.

2 min Saucedo etching of multi-grain MT1_M1 sample was applied in order to reveal twins and twin boundaries, grain and grain boundaries and investigate the shape of etch pits on different orientations as shown in **Figure 39**.

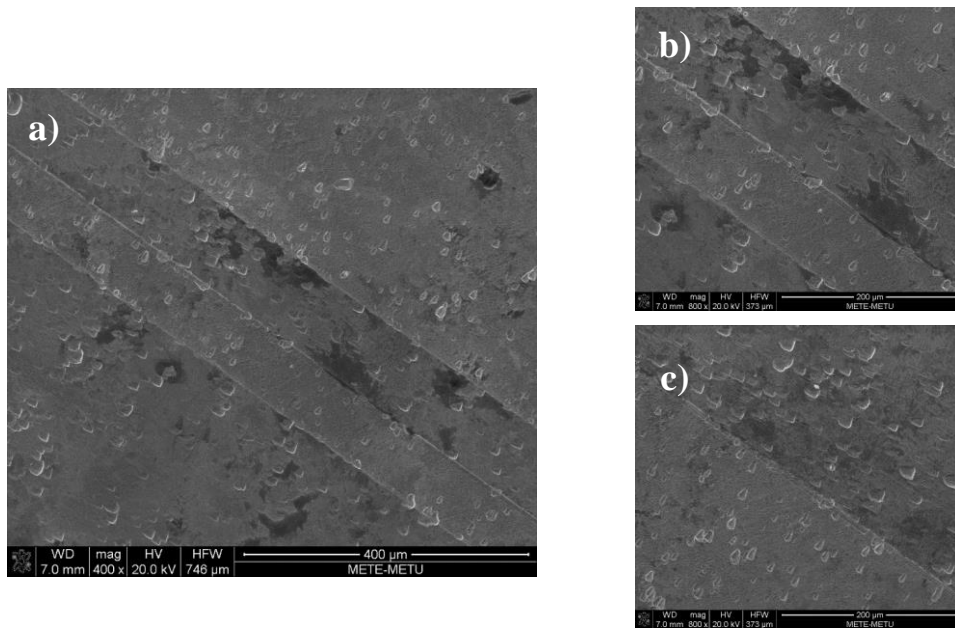


Figure 39 SEM images of 2 min Saucedo etched multi-grain MT1_M1 sample. **a)** Twins, grains and boundaries on the surface. **b)** Matt surface observed on the grain; shiny surface observed on the twin. **c)** Different shape of etch pits on twin and grain.

It was observed that etch pits on different orientations can be different considerably as shown in **Figure 40**. Etch pits on host grain and that on twin had different shape. Boundaries can be seen by the naked eye. The EPD on twin was $\sim 1.4 \times 10^5 \text{ cm}^{-2}$ and that on host grain was $\sim 1.2 \times 10^5 \text{ cm}^{-2}$. They had nearly same dislocation density, while the shape of the etch pits differed.

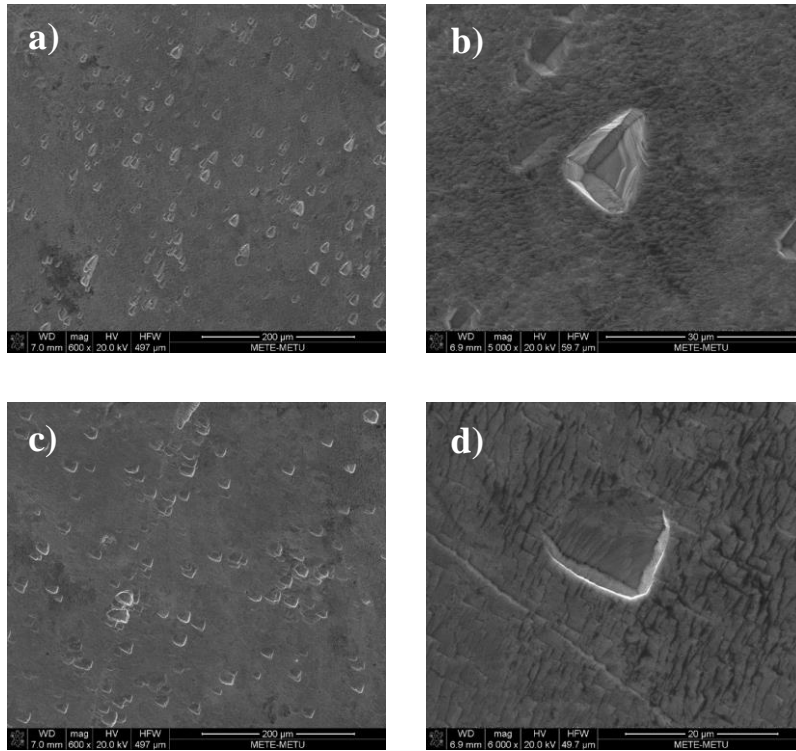


Figure 40 SEM images of 2 min Saucedo etched MT1_M1 sample. **a)** and **b)** Etch pit distribution and shape of the etch pits observed on twin; EPD $\sim 1.4 \times 10^5 \text{ cm}^{-2}$. **c)** and **d)** Etch pit distribution and shape of the etch pits appeared on host grain; EPD $\sim 1.2 \times 10^5 \text{ cm}^{-2}$.

4.3.6 Revealing Te inclusions by Etching Method

Since Inoue EAg2 reagent has a relatively high etching rate, original surface of CZT sample etched layer by layer and Te inclusions were exposed to the surface. After 5 min of etching, the feature of Inoue etchant changed and chemical polishing dominated over the dislocation etching. Since the concentration of silver ions decreased in the solution. Triangular etch pits and polyhedral Te inclusions over $\{111\}$ samples were observed by SEM analysis after a specific etching time.

Additionally, voids and cracks around polyhedral shaped Te inclusions were observed. Te has higher thermal expansion than CdZnTe crystal. During the etching process, stresses cause a distortion in CZT matrix and formation of voids, cracks and dislocations around Te inclusions were formed. Although a Te inclusion was small in dimension, it might cause large deformation field on the surface, leaving dislocations behind.

The morphology of Te inclusions were investigated on two different CZT samples as seen in **Figure 41**.

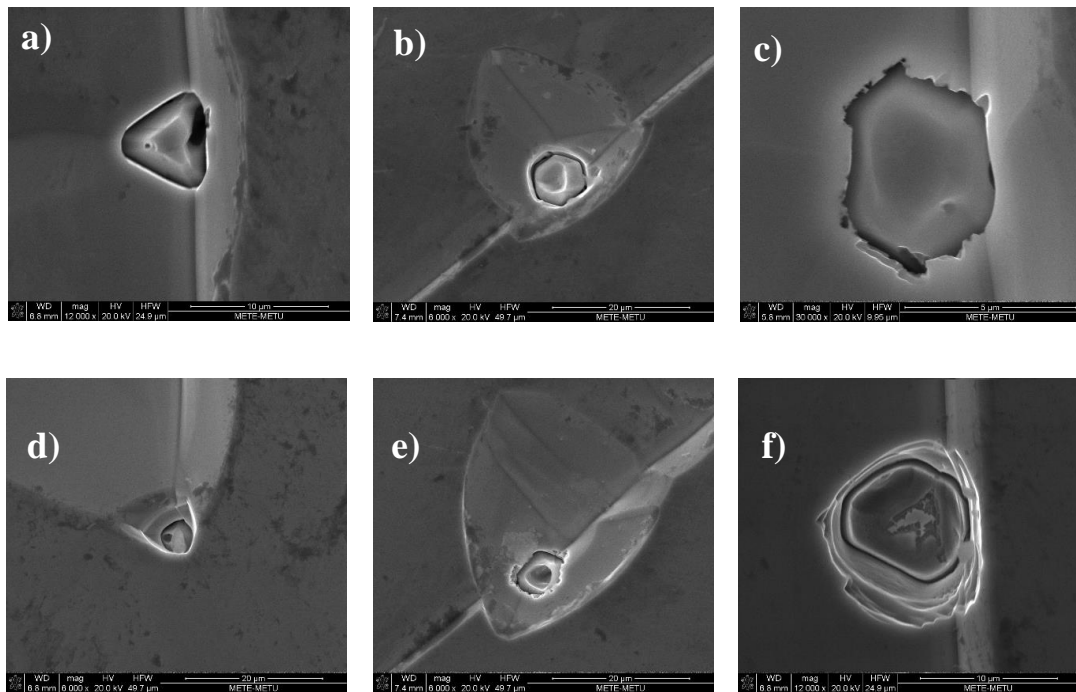


Figure 41 SEM images of Te inclusions embedded into two different CZT wafers. **a-f)** Triangular, hexagonal and polyhedral shaped Te inclusions

Figure 42 shows Te inclusions observed on MT2_S3 sample after 6 min Inoue EAg2 etching. **Figure 43** shows EDS analysis indicating that triangular etching pits were clearly Te inclusions; while, **Figure 44** shows EDS analysis of hexagonal etching pits with star-shaped Cd residuals. These polyhedral etch pits (Te inclusions) observed on a straight line in the {111} CZT crystal surface.

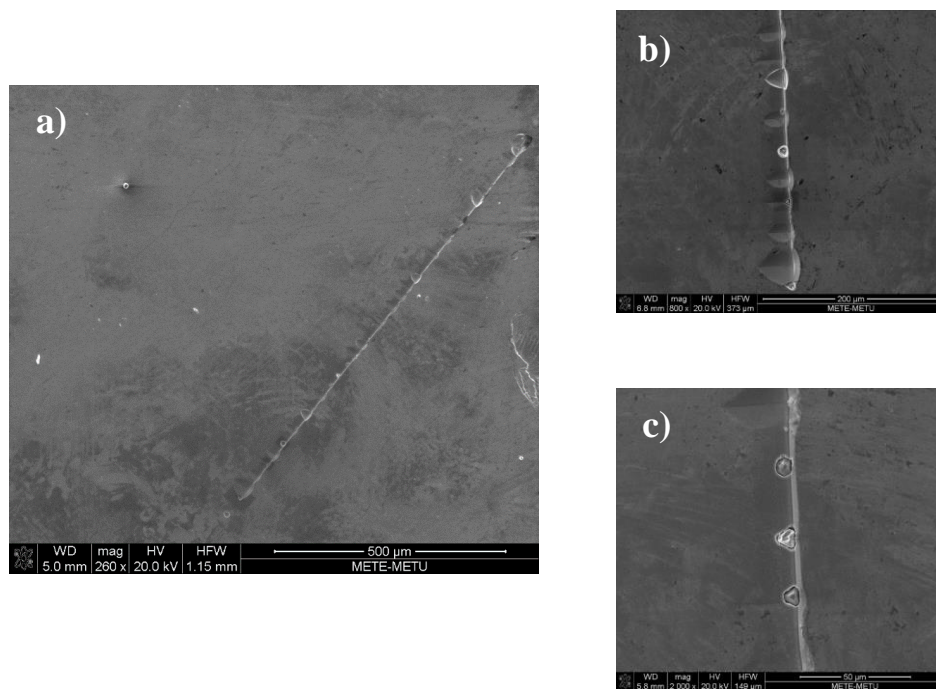


Figure 42 SEM images of 6 min modified EAg2 etched MT2_S3 sample. **a)** The etch pits on a straight line **b)** and **c)** Te inclusions and dislocations on the straight line

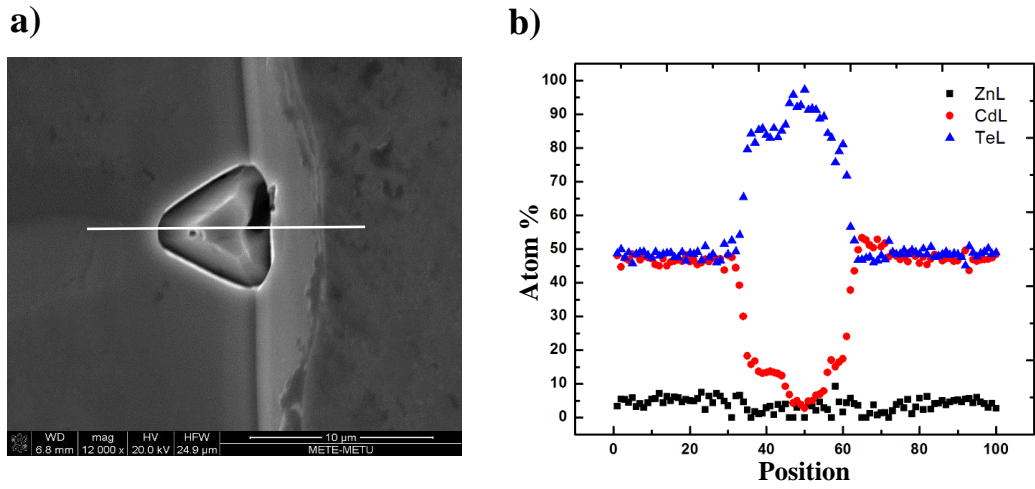


Figure 43 a) SEM image of triangular Te inclusion on MT2_S3 sample. b) EDS analysis shows the change in atomic concentration of Cd, Zn and Te on the points of the line.

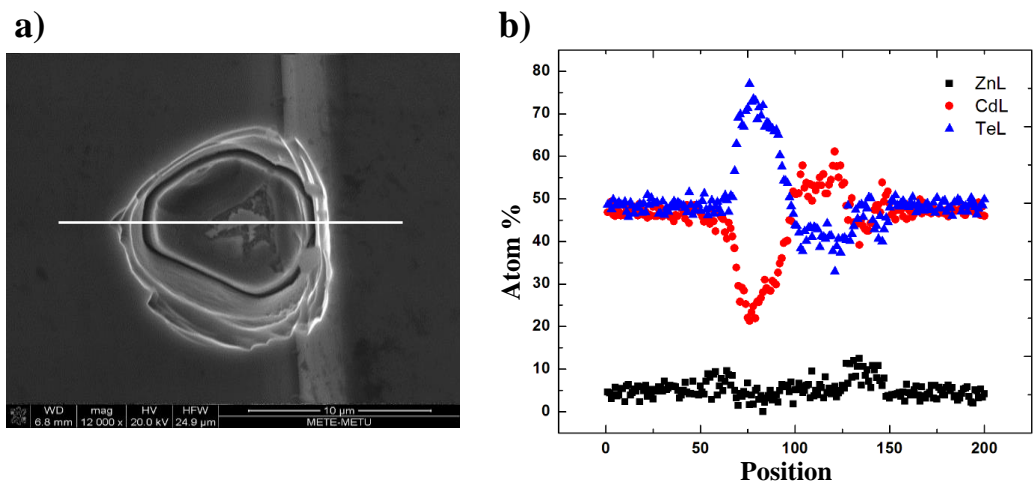


Figure 44 a) SEM image of hexagonal Te inclusions with star-shaped Cd residuals on MT2_S3 sample. b) EDS analysis shows the change in atomic concentration of Cd, Zn and Te on the points of the line.

Similarly, **Figure 45** shows Te inclusions observed on a line on MT1_S2 sample after 6 min Inoue EAg1 etching. **Figure 46** shows EDS analysis of hexagonal Te inclusions embedded into the triangular etch pits. Te inclusions initiated dislocations in the crystal structure resulting in etch pits on the surface of the sample.

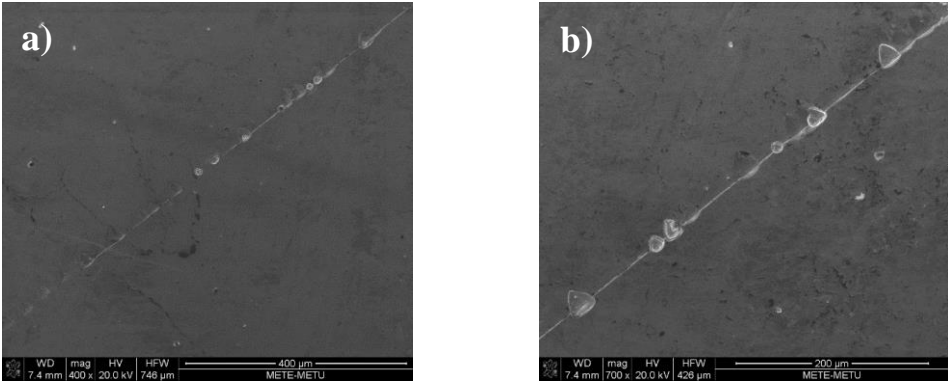


Figure 45 SEM images of 6 min modified EAg2 etched MT1_S2 sample. **a)** and **b)** Te inclusions and dislocations observed on a straight line.

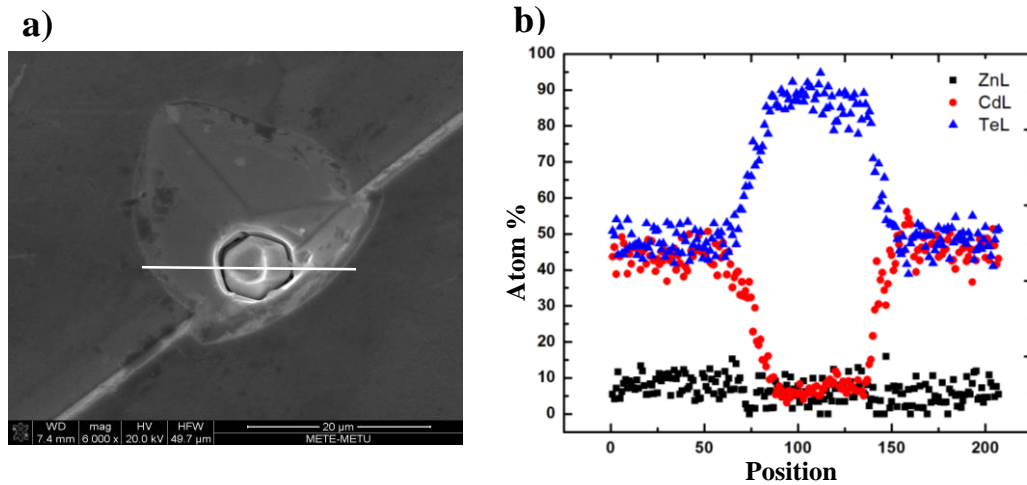


Figure 46 a) SEM image of hexagonal Te inclusion surrounded with dislocation on {111}B oriented MT1_S2 sample b) EDS analysis shows the change in atomic concentration of Cd, Zn and Te on the points of the line.

4.3.7 Etch Rate Analysis

In order to understand the behavior of etchants and their interactions with the CZT crystals, the etching rate of each etchant on two different orientations were investigated. It was observed that etchants have different etching rates on {111} and {211} planes. Etching rate was calculated using two different thickness measurement techniques; namely, calculated and measured as the thickness of the sample. ‘Calculated thickness’ found by calculating the thickness of the sample using mass, density and the area of the sample. On the other hand, ‘measured thickness’ was a direct measurement of the thickness using contact thickness measurement gauge. It was observed that calculated and measured thicknesses differed considerably on the same plane. However, measured thickness seemed to be more reliable than the calculated thickness, since weight measurement was less accurate (0.001 g). It was

observed that the calculated thickness gives higher etching rate than the measured thickness.

Inoue EAg2, Nakagawa and Everson etchants used to reveal the presence of dislocations and they dissolve strained regions of crystalline lattice, which initiated by dislocations and other defects. The stress field around these defects increased the etch rate and produced etch pits on the surface. In addition, the etching rate of planes were affected by etching conditions and their orientation [63].

Dislocation concentration and etching geometry as well as different agents and concentrations affected the etch rate on {111} and {211} orientations. In general, it was observed that {111} oriented samples had slightly higher etching rate. Correspondingly, it was observed that these dislocations in the crystals increased etching rate of {111} planes. Generally, EPD measurements showed that {111} oriented sample had higher dislocation density compare to {211} one. For a better understanding of the etching mechanism, the etch rate analysis should be studied with a great cautious.

4.3.7.1 Inoue EAg2 Etch Rate Analysis

Modified Inoue's EAg2 solution contains 20 ml H₂O + 10 ml HNO₃ + 4g K₂Cr₂O₇ + 30 mg AgNO₃. AgNO₃ is responsible for revealing dislocations; while, potassium dichromate chemically polish the crystal and produces a shiny surface. Additionally, HNO₃ is known as the strong oxidizing agent, which affects the etch rate. **Figure 47** and **Figure 48** show etch rate on MT2_W1 and MT1_S2 samples with calculated and thickness measurements respectively.

Etching rate on {111} plane was higher than that on {211} plane, as a result of higher density of dislocations on {111} plane.

Additionally, it was observed that the characteristic of this etchant was changed and up to 5 min of etching; dislocation etching dominated while for higher etching time chemical polishing dominated the etching procedures and leaving shiny surface behind with few Te inclusions on the surface.

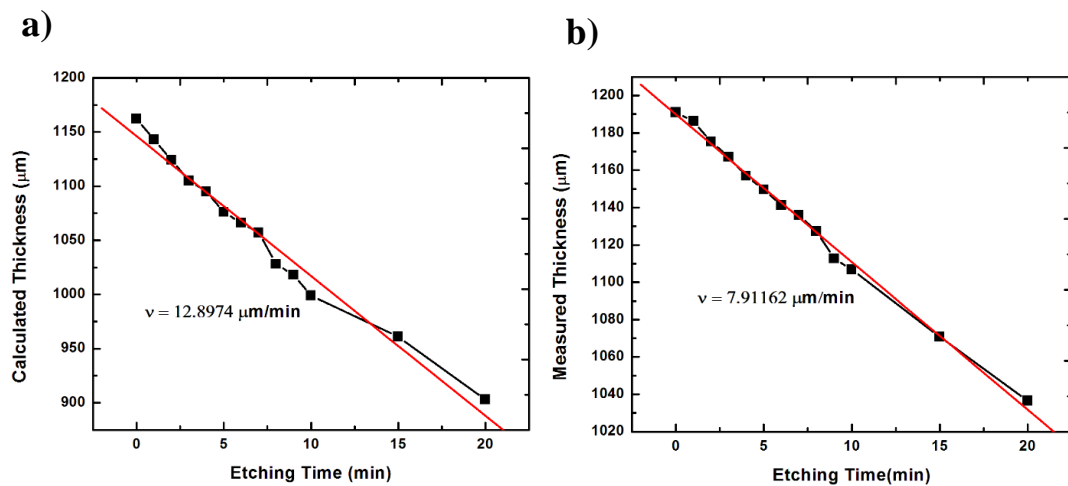


Figure 47 Inoue EAg2 etched {211} oriented MT2_W1 sample; **a)** Weight measurements, **b)** Thickness measurements.

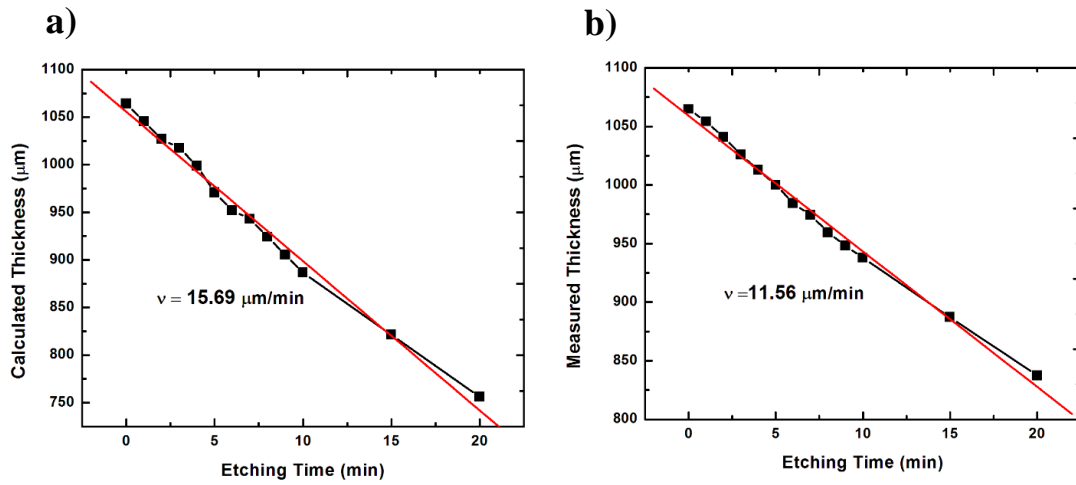


Figure 48 Inoue EAg2 etched {111} oriented MT1_S2 sample; **a)** Weight measurements, **b)** Thickness measurements.

4.3.7.2 Nakagawa Etching Rate Analysis

Nakagawa etchant consists of HF+H₂O₂+H₂O with a ratio of 3:2:2. Since the concentration of HF is higher than H₂O₂ (oxidizing agent), the surface of the sample is etched vigorously. **Figure 49** shows the etching rate of MT2_W1 sample with respect to weight and thickness measurements. Etching rate of MT1_S4 sample shown in **Figure 50**. Etching rate of {111} plane examined to be higher than on {211} plane. Etching rate changed significantly in accordance with the concentration of dislocations.

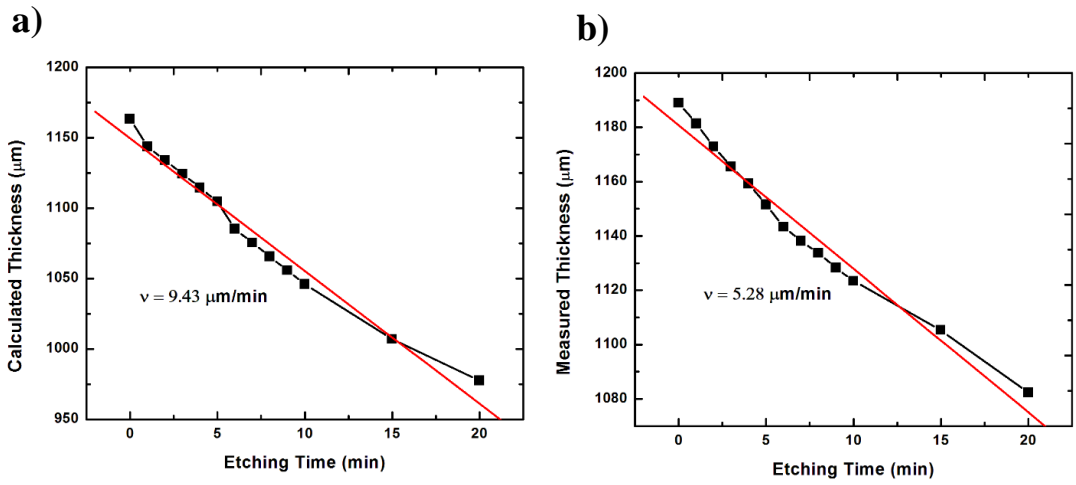


Figure 49 Nakagawa etched {211} oriented MT2_W2 sample **a)** Weight measurements, **b)** Thickness measurements.

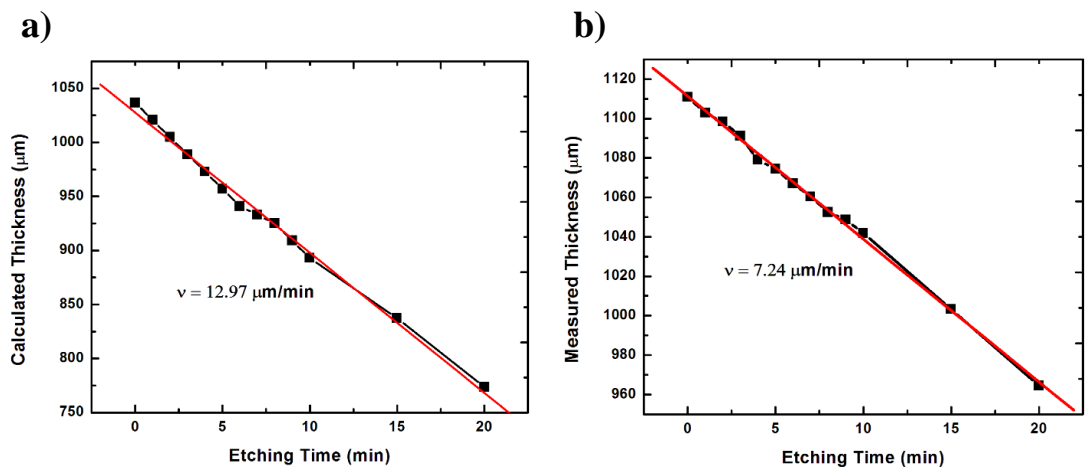


Figure 50 Nakagawa etching of {111} oriented MT1_S4 sample; **a)** Weight measurements, **b)** Thickness measurements.

4.3.7.3 Everson Etching Rate Analysis

Everson solution consists of HF+HNO₃+Lactic acid with a molar ratio of 1:4:25. The concentration of HF is considerably lower than the oxidant agent (HNO₃) and buffering agent (Lactic acid). Accordingly, etch rate measured to be less with respect to other etchants. **Figure 51** shows the etching rate of MT2_S1 and MT2_W3 samples. The etch rate of {111} plane calculated to have a slightly higher value than that for {211} plane.

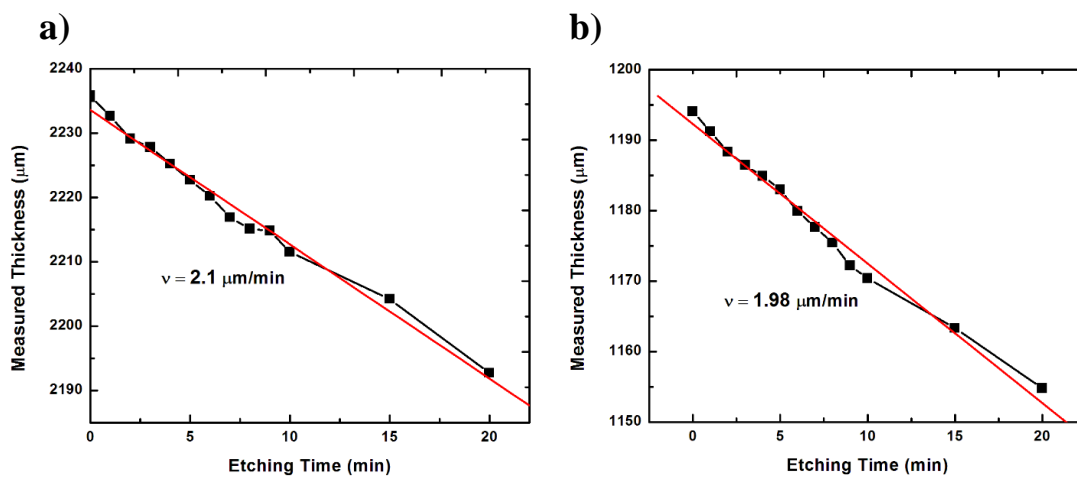


Figure 51 Thickness measurement of Everson etching; **a)** {111} oriented MT2_S1 Sample. **b)** {211} oriented MT2_W3 Sample.

4.3.8 Surface Chemistry

Surface composition of commercial CZT samples after B-M and E-solution etching was investigated. The change in the surface stoichiometry and chemical compositions was studied by XPS measurements including the depth profiling. A mechanically polished sample was used for comparing the effect of different chemical etching processes.

Figure 52 shows the results obtained for the relative atomic percentages for Te 3d₃, Cd 3d₃, Zn 2p₃, O1s and C1s as a function of sputter time. Mechanically polished {211} Commercial_W3 sample had similar surface composition as the B-M etched {211} Commercial_W1 sample. Both surfaces had Te-rich surfaces with graded composition near-surface region. The surface of the samples found to be oxidized and as the surface layers are removed by ion beam sputtering during the XPS measurements, the surface became more stoichiometric. **Figure 52c** shows that E-reagent polished {211} Commercial_W2 sample has a surface with more oxidation and lack of Cd compared to B-M etched Commercial_W1 and polished Commercial_W3 samples. XPS measurement of E-reagent showed that solution preferentially attacks the Cd in the bulk crystal.

Moreover, B-M etching yielded a better surface stoichiometry than E-reagent etching for a less sputter time. With these observations, it was concluded that B-M solution should be preferred in chemical etching after mechanical polishing to obtain better stoichiometric CZT surfaces.

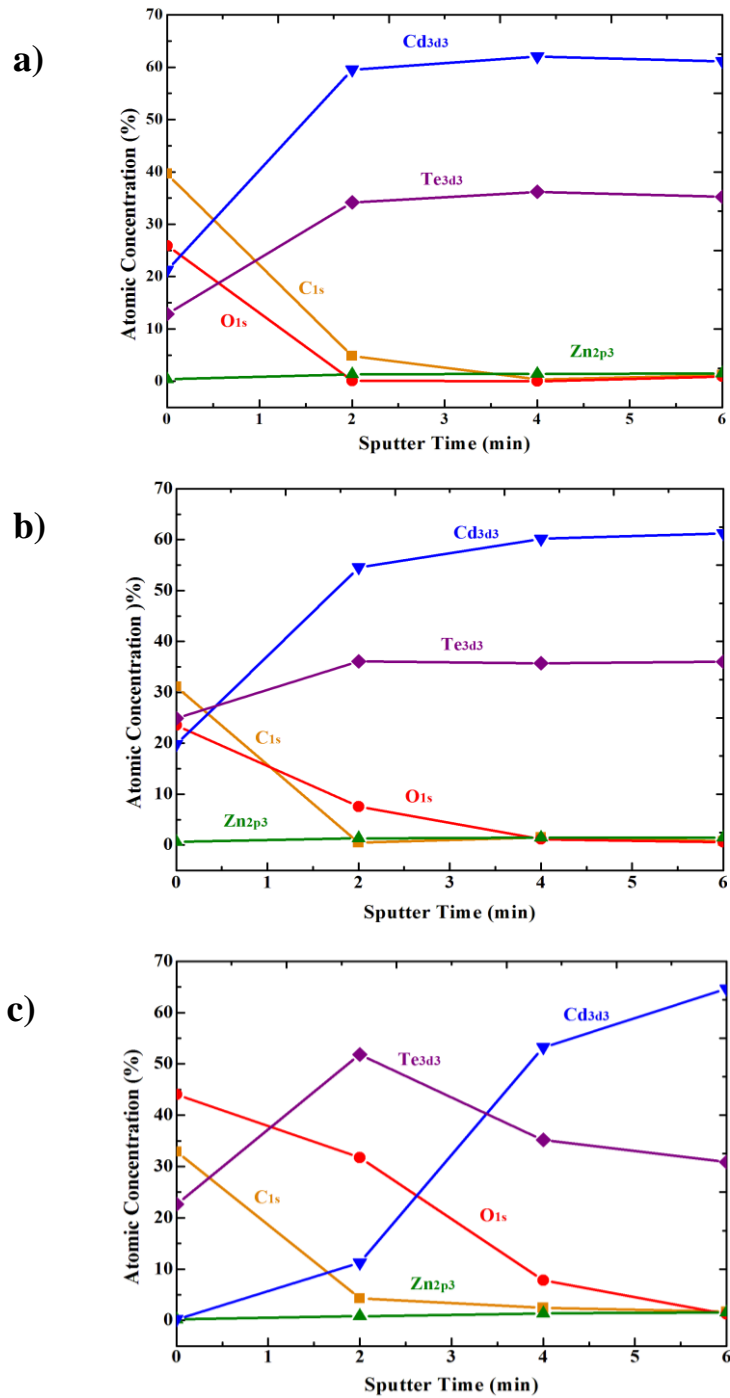


Figure 52 XPS depth profiles of CZT crystals: **a)** Mechanically polished Commercial_W3; **b)** Commercial_W1 etched in 1% B-M for 10 sec; and **c)** Commercial_W2 etched in E-reagent for 10 sec.

4.4 Oxidation studies

The surface chemistry of {211} CZT samples studied by chemical etching and oxidation process. Using XPS measurements, the changes in the surface composition of single-crystal CZT samples were investigated after exposure to Nakagawa etchant.

Figure 53a shows the Te 3d XPS spectrum from a CZT surface freshly etched in Nakagawa solution, and **Figure 53b** shows the surface etched with Nakagawa solution and left in the air at room temperature. Freshly etched surface showed the Te 3d_{5/2} peak at a binding energy of 572.9 eV, attributed to a Te-rich CZT surface. Te oxide peak also observed; but, with a small intensity. When the etched surface exposed to air oxidation, the formation of TeO₂ at 576.6 eV observed. The surface of the CZT sample had a graded Te-rich surface layer after exposure of Nakagawa etchant and the surface oxidized immediately after exposure to air producing a thin TeO₂ layer.

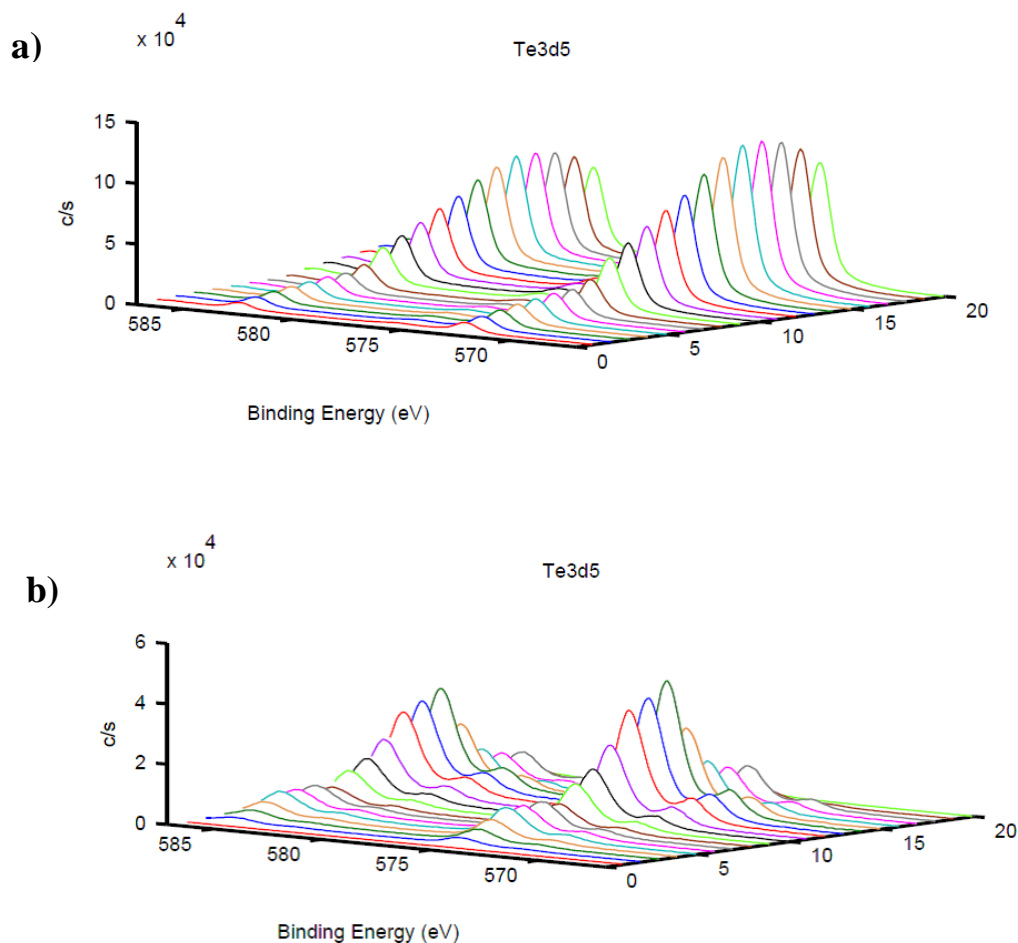


Figure 53 Angle Resolved XPS analysis of Nakagawa etched CZT samples; **a)** Variation of Te3d5 peak energies of freshly Nakagawa etched Commercial_W5 sample. **b)** Nakagawa Etched Commercial_W4 sample and exposed to air

Figure 54 shows the variation of atomic concentration of elements as a function of angle for freshly etched samples and that exposed to the air oxidation. In order to obtain highly sensitive surface analysis, higher analysis angles are needed. **Figure 54a** shows the atomic concentration of freshly etched Commercial_W5 sample and the result gave a Te rich surface. As expected, the oxide concentration was lower than the

Te concentration in the freshly etched sample. **Figure 54b** shows the variation of atomic concentration of elements as a function of angle for oxidation in air after etching. It was observed that sensitivity to surface element increased with decreasing the angle of incidence. It was clear that the sample was exposed to air showed higher oxide concentration on the surface than concentration of Te atom. As a result, when the thickness of the Te-rich graded layer increased, a thicker TeO_2 layer formed when sample exposed to air. The concentration of Te and O decreased with the increasing angle of incidence as the incoming x-ray beam penetrates further into the samples.

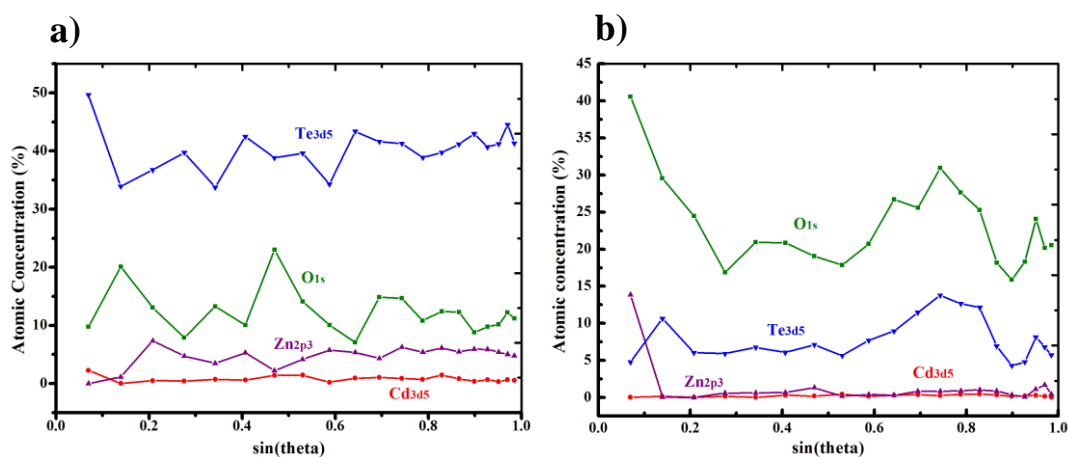


Figure 54 Angle-Resolved XPS showing the variation of atomic concentration vs $\sin(\theta)$. **a)** Atomic concentration of Commercial_W5 (freshly etched) sample **b)** atomic concentration of Commercial_W4 (air oxidation).

4.5 TEM

Defects were observed only by etching methods, which does not give any information about the lattice or atomic structure where defects initiated. Dislocations and Te inclusions were observed using different etchants and etch pits emerging at dislocation points were investigated. On the other hand, defects should be also investigated using TEM technique at atomic level.

CZT lattice arrangement, whose zinc-blende structure clearly seen was investigated using HREM micrograph with $\langle 110 \rangle$ zone axis (see **Figure 55**).

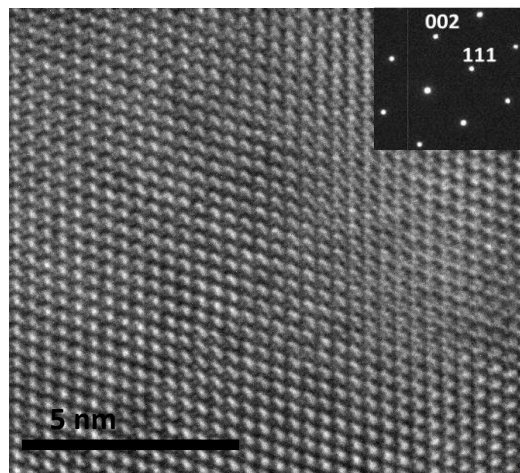


Figure 55 TEM image along the $\langle 110 \rangle$ zone axis with the corresponding SAED pattern of the CdZnTe crystal, which shows highly ordered arrangement zinc-blende lattice structure.

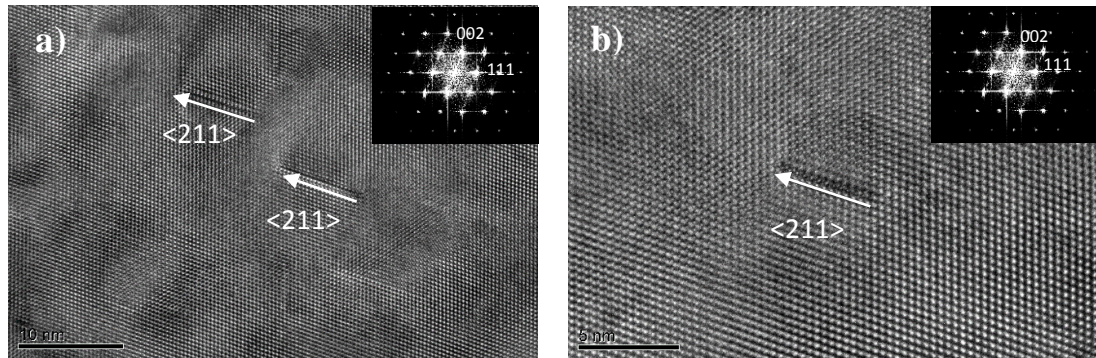


Figure 56 TEM images of multi-grain MT_M1 sample along $\langle 110 \rangle$ zone axis with the corresponding SAED pattern. **a)** and **b)** Stacking faults observed in the lattice along $\langle 211 \rangle$ direction.

Some areas were randomly picked up for HREM observation and defects observed on those regions. Much effort was spent to locate the defects by analyzing the HREM micrographs from the selected areas.

As mentioned in **2.2.1 Dislocations**, the separation of dislocations in Shockley slip system causes a stacking fault in the crystal structure along $\langle 211 \rangle$ direction.

The only observed defect in MT1_M1 crystal was the stacking fault, which is one of the most common defect observed in the CZT matrix. Stacking faults were observed throughout the CZT surface. **Figure 56** shows some mismatch in lattice of the MT_M1, showing a stacking fault in the CZT lattice. Stacking fault is associated with dislocations, where there is an incorrect stacking sequence of crystal planes [64].

4.6 EPD Overview

In this part of the thesis, a short overview on etch pit formation using different etchants was presented. Detailed structural analysis of the etch pits was given in the previous sections. In the EPD experiments, usually the samples were cleaved into pieces and each piece was etched by different etchants.

In addition, for the MT1_S3 sample, different etchants were applied with varying etching time after re-polishing the surface of the same sample for different etching procedures. Each etchant had different effect on MT1_S3 sample so the EPD and the shape of etch pits were changed. **Table 9** summarizes etch pits and EPD values were observed for different etchant solutions. In general, it was observed that Everson and Nakagawa etching yielded nearly the same EPD value. Moreover, the EPD found by using Inoue solution was one order lower than that of EPD found by using Nakagawa solution.

It was observed that the EPDs of the samples did not differ with increasing etching time in the case of Nakagawa and Everson etchants. However, etching with 2 min revealed etch pits at least twice as big as the etch pits formed by 1 min etching in many cases. It was found that extended defects dissolved continuously in the etching solution and thus the length and depth of the pits had a tendency to increase linearly with etching time. Additionally, EPD for $\{111\}$ orientation was found to be slightly higher than that for $\{211\}$ orientation for each etchant.

Table 9 EPD differences and change in the morphology of the pits obtained using different etchants

Nakagawa etching	Proper pitting both on A and B face. A face: rounded etch pits. B face: triangular etch pits. Also hexagonal shape pits are observed (Te inclusions). EPD calculated to be nearly same on both faces of the same sample.	EPD results for some of {111} and {211} samples EPD for MT1_S3 sample; $\sim 2.3 \times 10^5 \text{ cm}^{-2}$ EPD for Commercial_W4 sample; $\sim 1.2 \times 10^5 \text{ cm}^{-2}$
Everson etching	Flat bottomed and bar like etch pits are observed only on B face. No pitting on A face. EPD is relatively high since nanoscale pitting observed and nested structured pits investigated.	EPD for MT1_S3 sample; $\sim 1.2 \times 10^7 \text{ cm}^{-2}$ EPD for Commercial_W8 sample; $\sim 1.4 \times 10^5 \text{ cm}^{-2}$
Inoue EAg-2 etching	Give different result in each case. Stirring can affect etching. Etch pit observed on B face only. Pyramidal shaped etch pits with low concentration is observed. Seems to etch polyhedral shaped Te inclusions. Gives the lowest EPD results.	EPD for MT1_S3 sample; $\sim 9.5 \times 10^4 \text{ cm}^{-2}$ EPD for Commercial_W10; $\sim 7.0 \times 10^4 \text{ cm}^{-2}$
Bagai etching	Min 4 min etching is required. Triangular etch pits are observed. Surface etched vigorously.	EPD for MT1_S3 sample; $\sim 1.3 \times 10^6 \text{ cm}^{-2}$ EPD for Commercial_W11 sample; $\sim 4.3 \times 10^5 \text{ cm}^{-2}$
Saucedo etching	Min 1 min etching is required. Different shaped etch pits are observed on different orientations. Reveals twins and twin boundaries, grains and grain boundaries, and dislocations.	EPD for MT2_S4 sample; $9.6 \times 10^5 \text{ cm}^{-2}$ EPD for MT2_W5_1 sample; $1.2 \times 10^5 \text{ cm}^{-2}$

CHAPTER 5

CONCLUSIONS

The main goal of this thesis was to explore defects in CdZnTe crystals by chemical etching. Deeper fundamental understanding of micro-defects as well as etching mechanism was searched throughout the various chemical-etching studies. Many complementary and advanced diagnostic tools such as EDS, SEM, and AFM were used to reach a better understanding of defects and their formation by a specific etching solution. Moreover, nano-scale defects were studied using TEM analysis.

Prior to etching processes, mechanical polishing with alumina abrasive was applied to all crystals and chemical etching for final polish after mechanical polishing was done in order to produce damage free and stoichiometric surfaces. The flat and defect-free surfaces of the CZT crystals were obtained in order to reveal only as-grown dislocations initiated in the crystals. B-M and E-Reagent were the two solutions in literature used to obtain a shiny surface after mechanical polishing process. The surface chemistry of the samples was examined after applying these solutions and a graded composition near the surface was obtained for both solutions. Specifically, it was observed that chemicals in E-solution (HNO_3) preferentially attack Cd elements.

The main outcome of this thesis was to realize the knowledge and develop the methodology for revealing defects in CZT crystals using different crystallographic etching solutions. In particular, it was observed that the properties of the surface orientation, flatness of the surface, polishing agent, etching duration, chemicals used in etchants, concentration of the chemicals and polarity of the sample had a strong influence on the etching results presented in this work. It was clear that the shape of the etch pits and their growth kinetics depend on the etchant type, crystal orientation, and polarity of the crystal. For example, different etching studies were conducted using MT1_S3 sample to investigate the change in pit formation. Each etchant (EA_g-2,

Nakagawa, Everson, Bagai etchants) revealed dislocations by obtaining different shaped etch pits on MT1_S3 sample. Modified EAg-2 etching produced equilateral pyramidal triangular etch pits on MT1_S3 surface, while, triangular flat-bottomed etch pits were observed using Nakagawa etchants on the same surface after re-polishing. However, orientation of the sample also affected the shape of the etch pits for the same etchant. Modified EAg-2 and Saucedo etchants gave the most significant results for different orientations since these etchants work for all directions. In addition, the polarity of the sample also affected the shape of the etch pits. For example, when Nakagawa etching was applied, rounded etch pits observed on A face of the crystal; while, B face showed triangular etch pits.

Within the scope of studies conducted on Inoue's etchant, it was observed that the amount of AgNO_3 in modified EAg-2 solution should be three times higher than the specified amount for better formation of etch pits. Hence, this etchant can form etch pits on any orientation and reveals fresh and as-grown dislocations, twins and twin boundaries, grain and grain boundaries. However, on A faces of the CZT wafers, patchy results were obtained and etch pits were not observed on the A face of the samples after etching with modified EAg2 etchant. Additionally, formation of etch pits using Modified EAg-2 etchant was affected by stirring of the solution. On the other hand, stirring should be applied during the etching process to maintain the silver ions in the solution since $\text{Ag}_2\text{Cr}_2\text{O}_7$ precipitates can be dissolved by stirring. Following to a specific etching time, the characteristic of this etchant transformed from dislocation etching mechanism to chemical polishing and left shiny surface with a few Te inclusions on the surface.

The dependence of the etch rate on the orientation of CZT crystals was studied. The etch rates were analyzed as a function of the time and two different orientations. For all etchants considered, $\{111\}$ oriented samples had a higher etch rate than that of $\{211\}$ oriented samples. Interestingly, EPD values for all $\{111\}$ oriented samples were

higher than that of {211} oriented samples. Correspondingly, the etch rate was higher for {111} oriented samples.

Formation of the etch-pits was investigated using most of etchants presented in the literature. It was observed that the most feasible defect etchant for CdZnTe crystals is Nakagawa etching due to the repeatability of the formation of pits on both faces of {111} and {211} oriented crystals, which are important surfaces for epitaxial growth. Dislocation densities of A and B face were obtained to be nearly similar. The only disadvantages of Nakagawa etchant was that it resulted in Te rich surface and oxidation occurred immediately due to higher concentration of oxidant agent.

Additionally, the EPD results showed that the CZT samples grown in our lab (METU-Crystal Growth Laboratory) were compatible with commercial CZT substrates with respect to crystal quality. EPD values showed differences for different etchant solutions and Nakagawa etching gives the highest EPD values; while, modified EAg-2 solution gives the lowest.

Finally, stacking faults in CZT crystal was observed using TEM method. Atomic scale structural information about these defects was obtained. Results obtained from TEM analysis gave direct evidence of stacking faults emerged in the lattice of the crystals. The direction of stacking faults might give information about crystallographic etch pit formation and these might be correlated with the directions of pits' side.

As a future work, the aim is to develop deeper understanding of the formation mechanism of defects. Additionally, the effect of post growth annealing on defects can be studied. It is known that an annealing process can reduce the amount of defects and thus improves the crystal quality.

REFERENCES

- [1] A. Bolotnikov, S. Babalola, G. Camarda, Y. Cui, S. Egarievwe, A. Hossain, G. Yang and R. James, "Material Properties Limiting the Performance of CZT Gamma-Ray Detectors," 2009.
- [2] T. Schlesinger, J. Toney, H. Yoon, E. Lee, B. Brunett, L. Franks and R. James, "Cadmium Zinc Telluride and its use as a Nuclear Radiation Detector Material," *Materials Science and Engineering*, vol. 32, pp. 103-189, 2001.
- [3] S. Miyajima, H. Sakuragi and M. Matsumoto, "CdZnTe Detector as an X-Ray Spectrometer," *SPIE*, vol. 4320, pp. 148-155, 2001.
- [4] D. Hobbs and B. MacLeod, "Design, Fabrication, and Measured Performance of Anti-Reflecting Surface Textures in Infrared Transmitting Materials," *SPIE*, 2005.
- [5] P. Capper, *Properties of Narrow Gap Cadmium Based Compounds*, London: INSPEC, 1994.
- [6] W. Akutagawa, K. Zanio and J. Mayer, "CdTe as a Gamma Detector," *Nucl. Instrum. Methods.*, vol. 55, p. 383–385, 1967.
- [7] P. Norton, "HgCdTe Infrared Detectors," *Opto-Electronics Review*, vol. 10, pp. 159-174, 2002.
- [8] M. Kinch, *Fundamentals of Infrared Detector Materials*, Bellingham, Washington: SPIE, 2007.

- [9] H. Hobgood, B. Swanson and R. Thomas, "Czochralski Growth of CdTe and CdMnTe from Liquid Encapsulated Melts," *Journal of Crystal Growth*, vol. 85, no. 3, pp. 510-520, 1987.
- [10] C. Su and S. Lehoczky, "Growth of CdZnTe Crystals by Bridgman Technique with Controlled Overpressures of Cd," in *Fifth International Conference on Solidification and Gravity*, Hungary, 2008.
- [11] K. Mochizuki and K. Masumoto, "Growth of CdTe Single Crystals by THM (Travelling Heater Method) and its Repetition Effect," *Materials Letters*, vol. 4, no. 5-7, pp. 298-300, 1986.
- [12] T. Asahi, O. Oda, Y. Taniguchi and A. Koyama, "Growth and Characterization of 100 mm Diameter CdZnTe Single Crystals by the Vertical Gradient Freezing Method," *Journal of Crystal Growth*, vol. 161, no. 1-4, pp. 20-27, 1996.
- [13] D. Holt and B. Yacobi, *Extended Defects in Semiconductors*, New York: Cambridge, 2007.
- [14] D. Gasperino, "Modeling of Transport Process during Solution, Melt and Colloidal Crystal Growth," 2008.
- [15] A. Rogalski, "HgCdTe Infrared Detector Material: History, Status and Outlook," *Rep. Prog. Phys.*, vol. 68, p. 2267–2336, 2005.
- [16] C. Greaves, B. Brunett, J. VanScyoc, T. Schlesinger and R. James, "Material Uniformity of CdZnTe Grown by Low-Pressure," *Nuclear Instruments and Methods in Physics Research*, vol. 458, pp. 96-103, 2001.
- [17] A. Zappettini, L. Cerati, A. Milani, S. Pietralunga, P. Boffi and M. Martinelli, "High-Pressure Bridgman Grown CdZnTe for Electro-Optic Applications," *Journal of Electronic Materials*, vol. 30, no. 6, pp. 743-747, 2001.

- [18] A. Zappettini, L. Marchini, M. Zha, G. Benassi, N. Zambelli, D. Calestani, L. Zanotti, E. Gombia, R. Mosca, M. Zanichelli, M. Pavesi, N. Auricchio and E. Caroli, "Growth and Characterization of CZT Crystals by the Vertical Bridgman Method for X-Ray Detector Applications," *Transaction on Nuclear Science*, vol. 58, no. 5, pp. 2352-2356, 2011.
- [19] S. Sordo, L. Abbene, E. Caroli, A. Mancini, A. Zappettini and P. Ubertini, "Progress in the Development of CdTe and CdZnTe Semiconductor Radiation Detectors for Astrophysical and Medical Applications," *Sensors*, vol. 9, no. 5, p. 3491–3526, 2009.
- [20] A. Zappettini, M. Zha, M. Pavesi, F. Bissoli and L. Zanotti, "Boron Oxide Encapsulated Vertical Bridgman a Method for Preventing Crystal-Crucible Contact in CdZnTe growth," *IEEE*, pp. 3739-3741, 2006.
- [21] D. Brellier, E. Gout, G. Gaude, D. Pelenc, P. Ballet, T. Míguet and M. Manzato, "Bulk Growth of CdZnTe Quality Improvement and Size Increase," *Journal of Electronic Materials*, vol. 43, pp. 2901-2907, 2014.
- [22] R. Triboulet and P. Siffert, *CdTe and Related Compounds; Physics, Defects, Hetero- and Nano-structures, Crystal Growth, Surfaces and Applications*, Oxford: Elsevier, 2010.
- [23] J. Franc, R. Grill, P. Hlidek, E. Belas, L. Turjanska, P. Höschl, I. Turkevych, A. Toth, P. Moravec and H. Sitter, "The Influence of Growth Conditions on the Quality of CdZnTe Single Crystals," *Semicond. Sci. Technol.*, vol. 16, p. 514–520, 2001.
- [24] A. Hossain, A. Bolotnikov, G. Camarda, Y. Cui, G. Yang, K. Kim, R. Gul, L. Xu and R. James, "Extended Defects in CdZnTe Crystals Effects on Device Performance," *Journal of Crystal Growth*, vol. 312, p. 1795–1799, 2010.

- [25] M. Inoue, I. Teramoto and S. Takayanagi, "Etch Pits and Polarity in CdTe Crystals," *J. Appl. Phys.*, vol. 33, no. 8, pp. 2578-2582, 1962.
- [26] K. Nakagawa, K. Maeda and S. Takeuchi, "Observation of Dislocations in Cadmium Telluride by Cathodoluminescence," *Applied Physics Letters*, vol. 34, no. 9, p. 574, 1979.
- [27] R. Bagai, G. Seth and W. Borle, "Nature of the Crystallographic Defects on the (111) Te Surface of CdTe Delineated by Preferential Etching," *Journal of Crystal Growth*, vol. 91, no. 4, pp. 605-609, 1988.
- [28] J. Chen, "Etchant for Revealing Dislocations in II-VI Compounds". United State of America Patent 4,897,152, 30 Jan 1990.
- [29] W. Everson, C. Ard, J. Sepich, B. Dean and G. Neugebauer, "Etch Pit Characterization of CdTe and CdZnTe Substrates for Use in Mercury Cadmium Telluride," *Journal of Electronic Materials*, vol. 24, no. 5, pp. 505-510, 1995.
- [30] C. Watson, "Structural Defects in CdTe and Related Materials," Durham theses, Durham Univeristy, 1993.
- [31] J. J. Morriss, "Defects in Crystals," 2008. [Online]. Available: <http://www.mse.berkeley.edu/groups/morriss/MSE205/Extras/defects.pdf>. [Accessed 15 04 2015].
- [32] Q. Zheng, "Preparation and Development of CdTe and CdZnTe Detectors for Gamma Ray Radiation Applications," 2012.
- [33] J. Schreiber, L. HoÈring, H. Uniewski, S. Hildebrandt and H. Leipner, "Recognition and Distribution of A(g) and B(g) Dislocations in Indentation Deformation Zones on {111} and {110} Surfaces of CdTe," *phys. Stat. Sol.*, vol. 171, pp. 89-97, 1999.

- [34] G. Voort, *Metallography, Principles and Practice*, New York: ASM International, 1999.
- [35] X. Zhou, D. Ward, B. Wong, F. Doty and J. Zimmerman, "Molecular Dynamics Studies of Dislocations in CdTe Crystals from a New Bond Order Potential," *J. Phys. Chem.*, p. 17563–17571, 2012.
- [36] D. Hull and D. Bacon, *Introduction to Dislocations*, Burlington: Elsevier, 2011.
- [37] A. Hossain, A. Bolotnikov, G. Camarda, R. Gul, K. Kim, K. Kisslinger, G. Yang, L. Zhang and R. James, "Investigation of Structural Defect in CdZnTe Detector-Grade Crystal," *Journal of Electronic Materials*, vol. 41, no. 10, pp. 2908-2911, 2012.
- [38] Y. Shen, J. Henager, H. Chuck and L. Chen, "Simulations of Stress-Induced Twinning and De-Twinning: A Phase Field Model," *Acta Materialia*, p. 6554–6564, 2010.
- [39] H. Scheel and T. Fukuda, *Crystal Growth Technology*, Chichester, England: John Wiley & Sons, 2004.
- [40] A. Kelly and K. Knowles, *Crystallography and Crystal Defects*, United Kingdom: John Wiley & Sons, 2012.
- [41] F. Sansoz, H. Huang and D. Warner, "An Atomistic Perspective on Twinning Phenomena in Nano-Enhanced FCC Metals," *JOM*, pp. 79-84, 2008.
- [42] D. Zeng, W. Jie, T. Wang and H. Zhou, "Transmission Electron Microscopy Observations of Twin Boundaries and Sub-Boundary Networks in Bulk CdZnTe Crystals," *Journal of Crystal Growth*, p. 4414–4417, 2009.

- [43] C. Szeles, S. Cameron, J. Ndap and M. Reed, "Advances in the High-Pressure Crystal Growth Technology of Semi-insulating CdZnTe for Radiation Detector Applications," in *SPIE*, San Diego, 2003.
- [44] L. Casagrande, D. Marzio, M. Lee, D. Larson Jr, M. Dudley and T. Fanning, "Vertical Bridgman Growth and Characterization of Large-diameter Single-Crystal CdTe," *Journal of Crystal Growth*, 1993.
- [45] F. Doty, J. Butler, J. Schetzina and K. Bowers, "Properties of CdZnTe Crystals Grown by a High Pressure Bridgman Method," *J. Vac. Sci. Technol.*, pp. 1418-1422, 1992.
- [46] K. Lay, D. Nichols, S. McDevitt, B. Dean and C. Johnson, "High Quality Single Crystal CdTe Grown by a Modified Horizontal Bridgman Technique," *Journal of Crystal Growth*, 1988.
- [47] Y. Xu, W. Jie, R. Guo, T. Wang and G. Zha, "Size and Distribution of Te Inclusions in Detector-Grade CdZnTe Ingots," *Progress in Natural Science : Materials Internations*, pp. 66-72, 2011.
- [48] J. Min, X. Liang, J. Chen, D. Wang, H. Li and J. Zhang, "Investigation of Te Inclusions in CdZnTe Crystalline Material Using Raman Spectroscopy and IR Techniques," *Vacuum*, pp. 1003-1006, 2012.
- [49] A. Bolotnikov, N. AbdulJabber, S. Babalola, G. Camarda, Y. Cui, A. Hossain, E. Jackson, H. Jackson, J. James, K. Kohman, G. Yang, A. Luryi and R. James, "Effects of Te Inclusions on the Performance of CdZnTe Radiation Detectors," *IEEE*, 2009.
- [50] G. Kulkarni, K. Koteswara Rao, R. Raman, A. Pandey, R. Sharma, A. Garg and M. Srivastava, "Quality Assessment of CdZnTe (%4) Crystals," *IEEE*, 2007.

- [51] T. Wang, W. Jie and Z. Dongmei, "Observation of Nano-Scale Te Precipitates in Cadmium Zinc Telluride with HRTEM," *Materials Science and Engineering*, pp. 227-230, 2008.
- [52] M. Duff, D. Hunter, A. Burger, M. Groza, V. Buliga, J. Bradley, G. Graham, Z. Dai, N. Teslich, D. Black and A. Lanzirotti, "Characterization of Heterogeneities in Detector-Grade CdZnTe Crystals," *J. Mater. Res.*, pp. 1361-1367, 2009.
- [53] Y. Xu, W. Jie, T. Wang, P. Yua, Y. He, L. Fu and P. Sellin, "Morphology Evolution of Micron-Scale Secondary Phases in CdZnTe Crystals Grown by Vertical Bridgman Method," *Journal of Alloys and Compounds*, p. 2338–2342, 2011.
- [54] O. Babalola, A. Bolotnikov, M. Groza, A. Hossain, S. Egarievwe, R. James and A. Burger, "Study of Te Inclusions in CdMnTe Crystals for Nuclear Detector Applications," *Journal of Crystal Growth*, pp. 3702-3707, 2009.
- [55] M. Wada and J. Suzuki, "Characterization of Te Precipitates in CdTe Crystals," *Japanese Journal of Applied Physics*, pp. 972-975, 1988.
- [56] V. Ivanitska, P. Moravec, J. Franc, Z. Tomashik, P. Fochuk, V. Tomashik, L. Shcherbak, K. Mašek and P. Höschl, "Chemical Etching of CdTe in Aqueous Solutions of H₂O₂-HI-Citric Acid," *J. Electron. Mater.*, vol. 36, pp. 1021-1024, 2007.
- [57] L. Teague, M. Duff, J. Cadieux, R. Soundararajan, C. Shick Jr and K. Lynn, "Characterization of Etch Pit Formation via the Everson-Etching Method on CdZnTe Crystal Surfaces from the Bulk to the Nanoscale," *Nuclear Instruments and Methods in Physics Research Section A: Accelerators, Spectrometers, Detectors and Associated Equipment*, vol. 652, no. 1, p. 178–182, 2011.

- [58] P. Capper, *Narrow Gap II-VI Compounds for Optoelectronic and Electromagnetic Applications*, London: Chapman and Hall, 1997.
- [59] X. Cui, W. Fang, S. Sun, C. Zhang, H. Xu and J. Yang, "Characteristics of the Dislocations in CdZnTe Crystals Revealed by Etch Pits," *Journal of Crystal Growth*, vol. 321, pp. 40-44, 2011.
- [60] Y. Jianrong, G. Huiming, C. Xinqiang, F. Weizheng and H. Li, "Dislocation Assessment of CdZnTe by Chemical Etching on Both {111}B and {211}B Faces," *Journal of Crystal Growth*, vol. 234, pp. 337-342, 2002.
- [61] E. Saucedo, P. Rudolph and E. Dieguez, "Modified Bridgman Growth of CdTe Crystals," *Journal of Crystal Growth*, vol. 310, pp. 2067-2071, 2008.
- [62] P. Fewster and P. Whiffin, "Crystallographic Polarity and Etching of Cadmium Telluride," *J. Appl. Phys.*, vol. 54, pp. 4668-4670, 1983.
- [63] A. Nijdam, *Anisotropic Wet-Chemical Etching Of Silicon Pits, Peaks, Principles, Pyramids And Particles*, Enschede, 2001.
- [64] L. Guoqiang, S. ShaoJu, H. Yizhong, W. Tao and J. Wanqi, "Nanostructures of Defects in CdZnTe Single Crystals," *Journal of Crystal Growth*, vol. 311, p. 85–89, 2008.